Since 1955

Strojniški vestnik
Journal of Mechanical Engineering

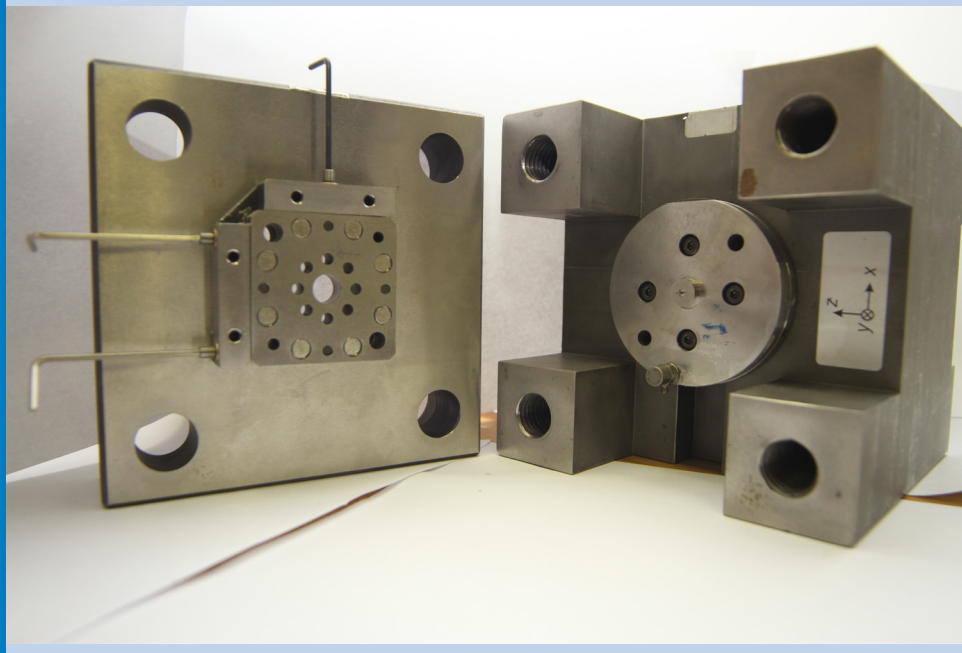

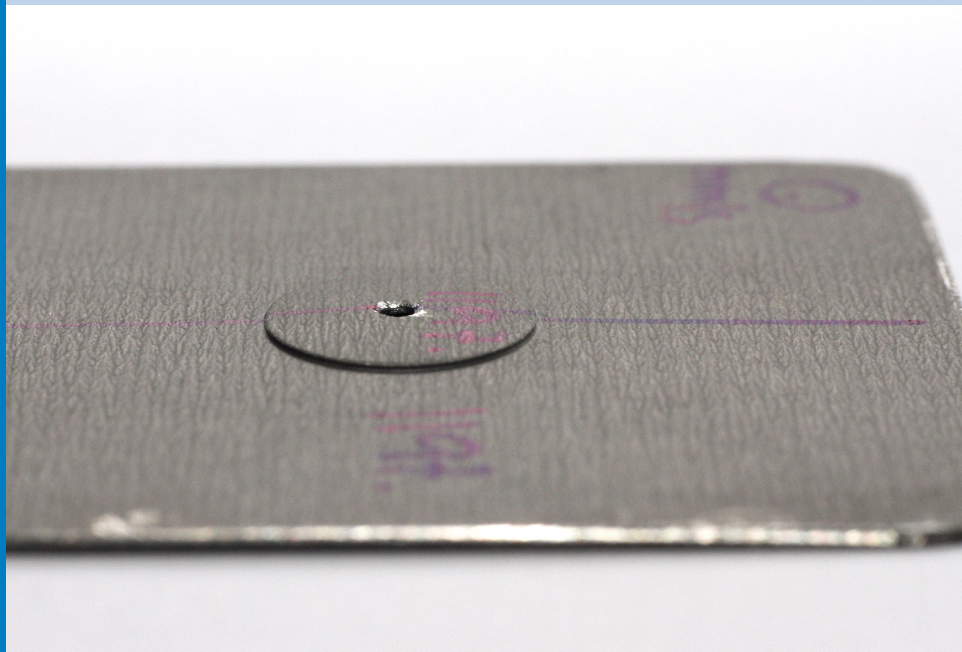

no. 4
year 2015
volume 61

Strojniški vestnik – Journal of Mechanical Engineering (SV-JME)

Aim and Scope

The international journal publishes original and (mini)review articles covering the concepts of materials science, mechanics, kinematics, thermodynamics, energy and environment, mechatronics and robotics, fluid mechanics, tribology, cybernetics, industrial engineering and structural analysis.

The journal follows new trends and progress proven practice in the mechanical engineering and also in the closely related sciences as are electrical, civil and process engineering, medicine, microbiology, ecology, agriculture, transport systems, aviation, and others, thus creating a unique forum for interdisciplinary or multidisciplinary dialogue.

The international conferences selected papers are welcome for publishing as a special issue of SV-JME with invited co-editor(s).

Editorial Office
University of Ljubljana, Faculty of Mechanical Engineering
SV-JME, Aškerčeva 6, SI-1000 Ljubljana, Slovenia
Phone: 386 (0)1 4771 137
Fax: 386 (0)1 2518 567
info@sv-jme.eu, http://www.sv-jme.eu

Print: Grafex, d.o.o., printed in 380 copies

Founders and Publishers
University of Ljubljana, Faculty of Mechanical Engineering, Slovenia
University of Maribor, Faculty of Mechanical Engineering, Slovenia
Association of Mechanical Engineers of Slovenia
Chamber of Commerce and Industry of Slovenia, Metal Processing Industry Association

Cover:
Experimental identification of mechanical characteristics of sheet metal is typically performed in the in-plane direction, demanding special preparation of specimens. An out-of-plane approach through sheet-metal blanking has been proposed. A cutting module (top) is used on a purposely-build laboratory blanking apparatus to determine material characteristics in the out-of-plane direction through analysis of full and partial (bottom) blanking experiments.

Image Courtesy: LADISK, Faculty of Mechanical Engineering, University of Ljubljana

ISSN 0039-2480

General information

Strojniški vestnik – Journal of Mechanical Engineering is published in 11 issues per year (July and August is a double issue).

Institutional prices include print & online access: institutional subscription price and foreign subscription €100,00 (the price of a single issue is €10,00); general public subscription and student subscription €50,00 (the price of a single issue is €5,00). Prices are exclusive of tax. Delivery is included in the price. The recipient is responsible for paying any import duties or taxes. Legal title passes to the customer on dispatch by our distributor.

Single issues from current and recent volumes are available at the current single-issue price. To order the journal, please complete the form on our website. For submissions, subscriptions and all other information please visit: *http://en.sv-jme.eu/.*

You can advertise on the inner and outer side of the back cover of the journal. The authors of the published papers are invited to send photos or pictures with short explanation for cover content.

We would like to thank the reviewers who have taken part in the peer-review process.

The journal is subsidized by Slovenian Research Agency.

Strojniški vestnik - Journal of Mechanical Engineering is available on http://www.sv-jme.eu, where you access also to papers' supplements, such as simulations, etc.

Contents

Strojniški vestnik - Journal of Mechanical Engineering
volume 61, (2015), number 4
Ljubljana, April 2015
ISSN 0039-2480

Published monthly

Papers

Strojniški vestnik - Journal of Mechanical Engineering 61(2015)4, 217-226
DOI:10.5545/sv-jme.2014.2302
Original Scientific Paper
Received for review: 2014-11-12
Received revised form: 2015-02-03
Accepted for publication: 2015-02-03

Identification of Out-of-Plane Material Characteristics through Sheet-Metal Blanking

Špela Bolka[1] – Janko Slavič[2] – Miha Boltežar[2,*]
[1] Hidria Rotomatika, Spodnja Idrija, Slovenia
[2] University of Ljubljana, Faculty of Mechanical Engineering, Slovenia

The mechanical characteristics of sheet metals are typically identified in the in-plane direction, although the sheet-metal forming processes (e.g., blanking, deep-drawing) are normally applied in the out-of-plane direction. As the mechanical characteristics are not necessarily constant, their direct experimental evaluation through the forming process would enable material monitoring and process optimization, and, additionally, material characterization in the out-of-plane direction. Full, partial (to a certain depth) and sequential (consecutive partial steps to full penetration) blanking experiments are performed on a laboratory blanking apparatus to correlate the out-of-plane material characteristics with the in-plane ones. The well-established in-plane approach to damage is introduced for the out-of-plane direction to determine the isotropic Lemaitre damage variable. Furthermore, yield and ultimate shear stresses are determined and correlated to their respective in-plane counterparts, offering a new insight in the sheet-metal blanking process.

Keywords: cutting and forming, constitutive behavior, elastic-plastic material, mechanical testing, ductile damage, out-of-plane experiment

Highlights
- *Experimental out-of-plane sheet-metal material characterization.*
- *Use of in-plane approach for out-of-plane characterization.*
- *Direct material characterization and correlation to in-plane parameters.*
- *Experimental Lemaitre damage characterization in the out-of-plane direction.*
- *Full, partial and sequential blanking experiments on laboratory blanking apparatus.*

0 INTRODUCTION

In sheet-metal forming, for instance blanking, shearing or deep drawing, identification of material mechanical properties (e.g. yield stress, ultimate stress, fracture point or material anisotropy) is crucial for manufacturing of high quality parts. The material parameters are typically determined experimentally, through in-plane tensile or shear tests, which require special preparation of specimens and cannot be applied continuously. As material characteristics may vary, a direct characterization process would enable fast correlation of current material characteristics to those of the standardized in-plane experiments and, thus, opened possibilities for process optimization.

The identification of yield and ultimate stresses in the in-plane direction is well documented and standardized. On the other hand, the evaluation of fracture point in ductile metals can be approached through several mechanisms **[1]** and **[2]**, leading to different experimental evaluation procedures. Among the mechanisms, roughly grouped into micromechanical models (e.g. **[3]** to **[6]**), uncoupled models (e.g. **[1]** and **[2]**) and coupled phenomenological models (e. g. **[1]**, **[7]** and **[8]**), the Lemaitre coupled phenomenological model, following the continuum damage mechanics (CDM) may be considered as most appropriate for direct and continuous material characterization. The model considers material damage through degradation of macroscopic material properties, for instance Young's modulus of elasticity or microhardness **[9]** and **[10]**. Damage is described as gradual material weakening due to initiation, growth and propagation of microscopic cracks and voids, resulting in macroscopic crack **[1]** and **[11]**. The Lemaitre damage model, based on experimental in-plane identification of parameters or on an inverse numerical analysis, has been successfully implemented in both in-plane (e.g. **[7]** and **[12]**) and out-of-plane (e.g. **[13]** and **[14]**) numerical applications. Nevertheless, extensions of the model have been proposed, for example including damage anisotropy (e.g. **[15]** and **[16]**) or Lode angle (e.g. **[1]** and **[17]**) for low stress-triaxiality applications.

Experimental identification of Lemaitre damage variable is typically performed through observation of variation in modulus of elasticity **[11]** and **[12]** or microhardness **[15]** and **[18]** by the uniaxial tensile experiment. The out-of-plane damage value is then estimated through the in-plane measurements **[10]**.

In the out-of-plane direction, several attempts of experimental characterization have been reported by the use of shear-punch testing, mainly as a validation of a numerical analysis. In most researches, yield

*Corr. Author's Address: University of Ljubljana, Faculty of Mechanical Engineering, 6 Aškerčeva cesta, Ljubljana, Slovenia, miha.boltezar@fs.uni-lj.si

and ultimate shear stress are identified and correlated to tensile stresses [19] and [20] and Abendroth and Kuna [21] used the shear punching process for inverse identification of the micromechanics-based GTN damage model parameters. But direct identification of the fracture and damage parameters has not yet been fully concluded [20]. Therefore, sheet-metal blanking would offer similar options to the shear-punch testing, resulting in total separation of the sheet metal, and thus enabling fracture point determination. Furthermore, the identification and optimization of the blanking process, although one of the most frequently used industrial processes for sheet laminations, is mostly focused on the optimization of the tools [22] to [24] or electromagnetic properties of the finished part [25]. Therefore would a direct material characterization procedure enable further understanding and optimization of the process.

In this research, sheet-metal blanking process was used to identify the out-of-plane material characteristics. Full, partial (to a certain depth) and sequential (consecutive partial steps up to full penetration) quasi-static and dynamic blanking experiments were performed in order to obtain the yield and ultimate stress and the material-damage progression directly from an out-of-plane experiment. A novel blanking apparatus (presented in detail in [26]) offers an out-of-plane experimental analysis of the sheet metal. The identified material parameters were compared to the material parameters obtained from classic uniaxial tensile tests.

The article is organized as follows. In Section 1 the theoretical background of the Lemaitre damage model and the small-strain plasticity are presented. Section 2 details the experimental approach. The experimental results are presented and discussed in Section 3. The conclusions are drawn in Section 4.

1 THEORETICAL BACKGROUND

In sheet-metal blanking process, a non-linear material response is accompanied with different phenomena of material degradation. The Lemaitre phenomenological damage model has an advantage of observing the degradation from an averaged, macroscopic point of view, therefore characterization of different damage phenomena is not required.

In this section, the constitutive equations of plasticity and the original formulation of the Lemaitre damage model are briefly summarized. The small-strain rate-independent plasticity with isotropic material hardening and isotropic damage is considered.

The Lemaitre damage model defines the isotropic scalar damage variable D ($0 \le D \le 1$) as the ratio of the damaged area S and the virginal (undamaged) area S_0 at any given plane in the volume of the material [27]:

$$D = 1 - \frac{S}{S_0}. \tag{1}$$

Using the hypothesis of strain equivalence [28], the stress tensor $\boldsymbol{\sigma}$ of the undamaged material is replaced by the effective stress tensor $\tilde{\boldsymbol{\sigma}}$ in the damaged material:

$$\tilde{\boldsymbol{\sigma}} = \frac{\boldsymbol{\sigma}}{1-D}. \tag{2}$$

In the framework of small-strain rate-independent plasticity, the total strain after the yield can be decomposed into the elastic $\boldsymbol{\varepsilon}^{\mathrm{e}}$ and plastic $\boldsymbol{\varepsilon}^{\mathrm{p}}$ (see [29] for details):

$$\boldsymbol{\varepsilon} = \boldsymbol{\varepsilon}^{\mathrm{e}} + \boldsymbol{\varepsilon}^{\mathrm{p}}. \tag{3}$$

The Helmholtz free energy ψ is defined as the free potential, depending on the internal variables, i.e., the elastic strain $\boldsymbol{\varepsilon}^{\mathrm{e}}$, the internal variables associated with isotropic hardening κ and the isotropic damage variable D. The free energy can be decomposed into the elastic-damage ψ^{ed} and the plastic ψ^{p} free energy [28]:

$$\begin{aligned}\psi\left(\boldsymbol{\varepsilon}^{\mathrm{e}}, \kappa, D\right) &= \psi^{\mathrm{ed}}\left(\boldsymbol{\varepsilon}^{e}, D\right) + \psi^{\mathrm{p}} = \\ &= \left[\frac{1}{2}\boldsymbol{\varepsilon}^{\mathrm{e}} : (1-D)\mathbf{D} : \boldsymbol{\varepsilon}^{\mathrm{e}}\right] + \left[\bar{\rho}\psi^{\mathrm{I}}(\kappa)\right],\end{aligned} \tag{4}$$

where $\bar{\rho}$ represents the material density and $\psi^{\mathrm{I}}(\kappa)$ is the free energy associated with isotropic hardening. $\mathbf{D}$ is the standard elasticity tensor. The thermodynamic forces associated with the internal variables (see [29]) are determined as:

$$\boldsymbol{\sigma} = \bar{\rho}\frac{\partial \psi^{\mathrm{ed}}\left(\boldsymbol{\varepsilon}^{\mathrm{e}}, D\right)}{\partial \boldsymbol{\varepsilon}^{\mathrm{e}}} = (1-D)\mathbf{D} : \boldsymbol{\varepsilon}^{\mathrm{e}}, \tag{5a}$$

$$R = \bar{\rho}\frac{\partial \psi^{\mathrm{p}}(\kappa)}{\partial \kappa} = R(\kappa), \tag{5b}$$

$$Y = \bar{\rho}\frac{\partial \psi^{\mathrm{ed}}\left(\boldsymbol{\varepsilon}^{\mathrm{e}}, D\right)}{\partial D} = -\frac{1}{2}\boldsymbol{\varepsilon}^{\mathrm{e}} : \mathbf{D} : \boldsymbol{\varepsilon}^{\mathrm{e}}, \tag{5c}$$

where $\boldsymbol{\sigma}$ is the stress tensor, R is the thermodynamic force associated with isotropic hardening and Y is the thermodynamic force associated with damage.

For the Lemaitre damage model, the thermodynamic damage force, or the energy density release rate, is determined as [26]:

$$-Y=\frac{\sigma_{\mathrm{eq}}^{2}}{2E\left(1-D\right)^{2}}\cdot\left[\frac{2}{3}\left(1+\nu\right)+3\left(1-2\nu\right)\left(\frac{p}{\sigma_{\mathrm{eq}}}\right)^{2}\right], \quad (6)$$

where:

$$\sigma_{\mathrm{eq}}=\sqrt{\frac{3}{2}}\left\|\mathbf{s}\right\|, \quad (7)$$

is the von Mises equivalent stress with **s** as the stress deviator tensor. $p=\frac{1}{3}\mathrm{tr}\left(\boldsymbol{\sigma}\right)$ represents the hydrostatic stress, E is the Young's modulus of elasticity and ν is the Poisson's ratio.

The evolution of the internal variables is derived by assuming the existence of a scalar potential of the dissipation Ψ that can be decomposed into the plastic Ψ^{p} and damage Ψ^{d} components (see [10] for details):

$$\Psi=\Psi^{\mathrm{p}}+\Psi^{\mathrm{d}}=\Phi+\frac{r}{\left(1-D\right)\left(s+1\right)}\left(\frac{-Y}{r}\right)^{s+1}, \quad (8)$$

where Φ is the yield function and r and s are the material parameters of the damage model. For the von Mises yielding, the yield function is given as:

$$\Phi\left(\boldsymbol{\sigma},\varepsilon_{\mathrm{eq}}^{\mathrm{p}},D\right)=\frac{\sigma_{\mathrm{eq}}}{1-D}-\sigma_{\mathrm{y}}, \quad (9)$$

where σ_{y} represents the current yield stress:

$$\sigma_{\mathrm{y}}=\sigma_{\mathrm{y0}}+R\left(\kappa\right), \quad (10)$$

with σ_{y0} as the initial yield stress and $R(\kappa)$ is the isotropic hardening function, with the hardening variable κ equal to the accumulated plastic strain $\bar{\varepsilon}^{\mathrm{p}}$ (see [27] for details):

$$\bar{\varepsilon}^{\mathrm{p}}=\sqrt{\frac{2}{3}\left\|\boldsymbol{\varepsilon}^{\mathrm{p}}\right\|}. \quad (11)$$

The evolution of the internal variables is determined by:

$$\dot{\boldsymbol{\varepsilon}}^{\mathrm{p}}=\dot{\gamma}\frac{\partial\Psi}{\partial\boldsymbol{\sigma}}=\dot{\gamma}\mathbf{N}, \quad (12a)$$

$$\dot{\kappa}=-\dot{\gamma}\frac{\partial\Psi}{\partial R}=\dot{\gamma}=\dot{\varepsilon}^{\mathrm{p}}, \quad (12b)$$

$$\dot{D}=\dot{\gamma}\frac{\partial\Psi}{\partial Y}=\dot{\gamma}\frac{1}{1-D}\left(\frac{-Y}{r}\right)^{s}, \quad (12c)$$

where $\dot{\gamma}$ represents the plastic multiplier and **N** is the plastic flow vector. Assuming an associative plastic flow it follows:

$$\mathbf{N}=\sqrt{\frac{3}{2}}\frac{\mathbf{s}}{\left\|\mathbf{s}\right\|}. \quad (13)$$

The evolution of the internal variables is subjected to the Kuhn-Tucker loading/unloading conditions:

$$\dot{\gamma}\geq 0,\quad \Phi\leq 0,\quad \dot{\gamma}\cdot\Phi=0. \quad (14)$$

2 EXPERIMENTAL PROCEDURE

Two sets of experiments were performed - the classic uniaxial tensile experiments and the blanking experiments.

2.1 Material

A low-alloyed steel sheet metal M400-50A HP of nominal thickness 0.5 mm was used for all the experiments in this investigation. All the specimens were obtained from the same part of the sheet-metal roll. The mechanical characteristics will be presented later on, as obtained from uniaxial tensile experiments. The uniaxial tensile test were performed in the steel-sheet rolling direction.

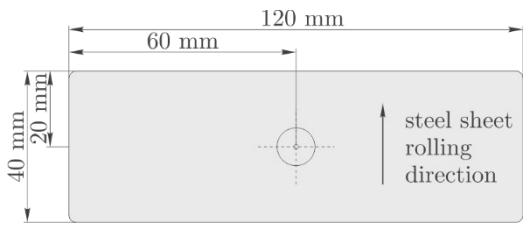

Fig. 1. *Specimen used for blanking experiments with the indicated circular blanking shape*

Standard specimens (ISO 6892-1) for the tensile testing were obtained by blanking. The edges of the samples were additionally smoothed to reduce the edge effects in the tensile tests. For the blanking experiments, specimens, an example is shown in Fig. 1, were obtained by water-jet cutting. The central hole with a diameter of 1.2 mm, used for the punch-displacement measurement (explained later), was obtained by drilling.

2.2 In-Plane Experimental Setup (Tensile Experiments)

Full and stepwise uniaxial tensile experiments were performed using an Instron universal hydraulic machine. Full tensile tests were performed according to the ISO 6892-1 standard. Stepwise uniaxial tensile tests were based on the same standardized procedure. For every 2 % of deformation the sample was unloaded and loaded again up to full rupture.

Strain, elongation, force and stress were measured at the hydraulic head with the built-in sensors.

2.3 Out-of-Plane Experimental Setup (Blanking Experiments)

Blanking experiments were performed using the custom-built laboratory blanking apparatus [24]. The apparatus enables quasi-static (blanking speeds of about 0.1 mm/s) and dynamic blanking experiments (blanking speeds depending on the thickness of the sheet metal and the circumference of the cutting tools; typically about 200 mm/s or more).

The quasi-static blanking is performed by turning a fine-threaded screw in the fixation block (Fig. 2) that propels the piston and the punch forward in the cutting module, shown in Fig 4. For dynamic blanking, the blanking apparatus is elevated at one end for an angle α (Fig. 3) and the impactor is released from rest from an arbitrary position on the slope. Typically, the blanking apparatus is raised for about 5°. The initial potential energy of the impactor is transformed to the initial kinetic energy of the piston and the punch at the base of the slope. The position of the impactor on the slope can be determined up to 1 mm accurately, resulting in ±5 mm/s control of the blanking speed.

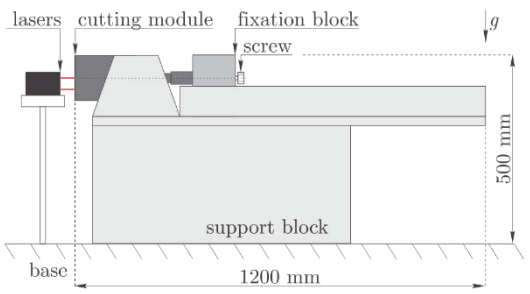

Fig. 2. *Custom blanking apparatus in configuration for quasi-static experiments; g represents acceleration due to gravity*

The blanking is performed in the cutting module (Figs. 4 and 5). The sheet metal is held in place by 8 strong magnets that are inserted into the die. The punch displacement is measured on the punch tip, a 1-mm-diameter extension from the tip, using a Keyence LG-82 displacement laser. The punch force is measured by a Kistler 9061A ring-type force transducer, mounted behind the punch. The punch acceleration is measured using a Brül&Kjær, type 8309 accelerometer.

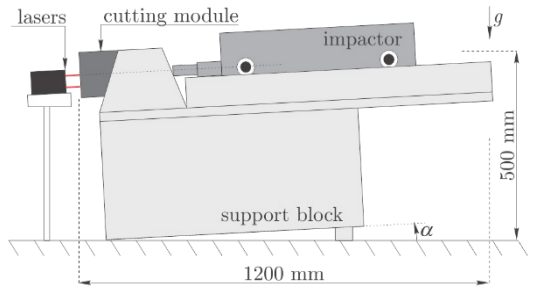

Fig. 3. *Custom blanking apparatus: configuration for dynamic experiments; g represents acceleration due to gravity*

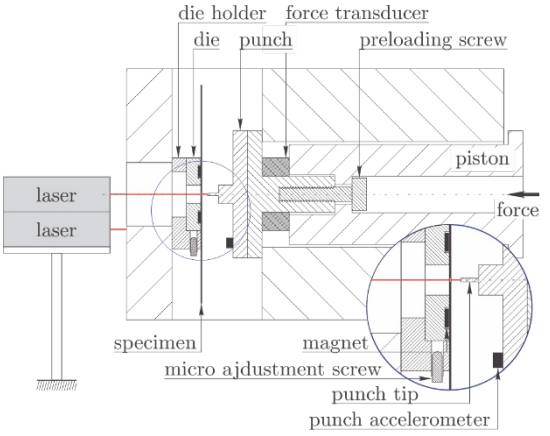

Fig. 4. *The cutting module*

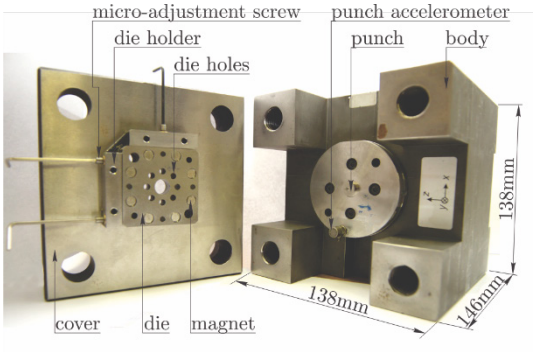

Fig. 5. *The cutting module in an opened position*

For this research, a centric circular punch-die set with a nominal diameter of 10 mm and a clearance of 25 µm per radius was used. The set was not lubricated and all the experiments were performed at room temperature (about 23 °C). The full experiments were

performed quasi-statically with a blanking speed of about 0.1 mm/s and dynamically with blanking speeds of approximately (200, 250, 300, 350) mm/s. The partial and sequential quasi-static experiments were performed with a blanking speed of about 0.1 mm/s, whereas the dynamic blanking experiments were performed with a blanking speed just high enough for the punch to reach the designated depth.

The partial experiments were performed up to depths of (100, 200, 300, 350) µm and the sequential experiments were performed in steps of 50 µm. The repeatability of the laboratory blanking apparatus is above 95 % and is discussed in detail in [24].

In all the out-of-plane experiments, at least five trials (to obtain minimal statistical requirements) were performed and averaged. Data was smoothed using a Hann window over 11 measurement points.

3 RESULTS

3.1 In-Plane Experimental Results

3.1.1 Yield Stress and Material Hardening Law

The material hardening data was obtained from standard uniaxial tensile tests (results shown in Fig. 5). As the material exhibits a Lüder plateau, a combined isotropic hardening material model was defined. After the initial yield stress σ_{y0} the material exhibits a linear hardening behavior with a hardening coefficient K:

$$\sigma_y = \sigma_{y0} + K\bar{\varepsilon}^p, \tag{15}$$

where $\bar{\varepsilon}^p$ is the accumulated plastic strain. After the limit accumulated plastic strain $\bar{\varepsilon}^{p0}$ is reached, the material exhibits an exponential Voce/saturation-type hardening law [28]:

$$\sigma_y = \sigma_{y1} + \left(\sigma_\infty - \sigma_{y1}\right)\left(1 - e^{-\bar{\varepsilon}^p m}\right), \tag{16}$$

where $\sigma_{y1} = \sigma_{y0} + K\bar{\varepsilon}^{p0}$, σ_∞ is the saturation stress. The parameters of the combined material model for the rolling direction of steel are given in Table 1. The fitting of the combined model to the experimental data is shown in Fig. 5.

3.1.2 Damage Parameters

As shown in [12], it follows from Eqs. (1), (2) and (5a):

$$D = 1 - \frac{E}{E_0}, \tag{17}$$

where E and E_0 are the current and initial Young's modulus of elasticity.

Under the assumption of $s = 1$, the damage parameter r was obtained from the sequential tensile tests [12]. For the uniaxial tensile test, Eq. (6) is simplified to:

$$-Y = \frac{\sigma^2}{2E\left(1-D\right)^2}. \tag{18}$$

Using Eq. (18) in Eq. (12c), damage propagation in relation to the accumulated plastic deformation can be written as:

$$\frac{\mathrm{d}D}{\mathrm{d}\bar{\varepsilon}^p} = \frac{\sigma^2}{2Er\left(1-D\right)^2}. \tag{19}$$

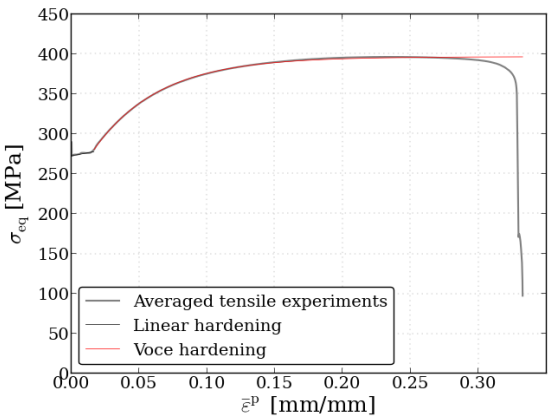

Fig. 6. *Averaged full uniaxial tensile experiments with modelled hardening curves*

It follows that the damage parameter r is equal to:

$$r = \frac{\sigma^2}{2E\left(1-D\right)^2}\frac{\mathrm{d}D}{\mathrm{d}\bar{\varepsilon}^p}. \tag{20}$$

For statistical reasons as mentioned above, five sequential tests were performed, as shown in Fig. 6. As recommended by [10], the elastic modulus was determined on the unloading part of each step. Fig. 7 shows the degradation of the elastic modulus and the accumulation of damage in relation to the accumulated plastic strain. For each unloading point the minimum and maximum values of the parameters are shown by the error bar. Using Eq. (20), it follows $r = 0.953$ MPa.

3.2 Out-of-Plane Experimental Results

Full, partial and sequential experiments were performed quasi-statically and dynamically. The

mechanics of the blanking experiments is different to the mechanics of the in-plane experiments. In contrast to the clamped specimen in the tensile test, in the blanking experiment the cutting tools and the specimen initially come into contact and the cutting tools affect the material's response in the initial elastic zone. Therefore, the resulting blanking force vs. punch penetration ($P-d$) diagrams do not show all the distinct characteristics of the total stress vs. total strain diagrams resulting from the tensile experiment. The elastic response of the material was therefore identified during the unloading phase when the cutting tools are retracting from the material.

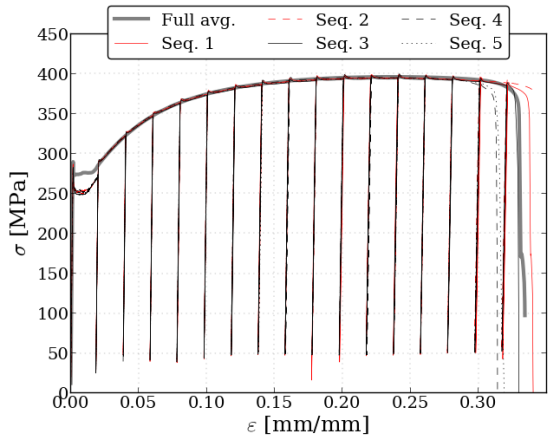

Fig. 7. *Sequential uniaxial tensile experiments, compared to averaged full uniaxial tensile experiment*

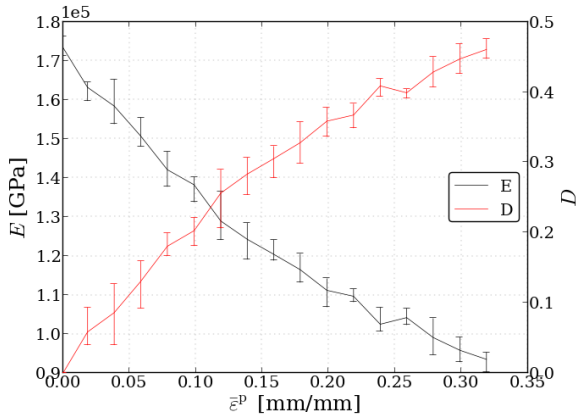

Fig. 8. *Identification of damage for uniaxial tensile experiments*

Although the inertial forces are accounted for (see [24] for details), complete elimination is not possible at higher blanking speeds, as the dynamics of the process becomes more pronounced (Fig. 8). However, during the unloading part, a similar slope of the P–d diagram is expected.

3.2.1 *Yield and Ultimate Stress*

The shear stress can be estimated as (see [19]):

$$\tau = \frac{P}{2\pi r_{\text{avg}} t}, \tag{21}$$

where $r_{\text{avg}} = (r_{\text{die}} + r_{\text{punch}})/2$ is the average radius of the cutting tools and t is the thickness of the specimen. The correlation between the ultimate and the yield stress in the tensile and shear directions can be obtained from the $P-d$ diagram for the full blanking experiments. Averaged diagrams (at least five measurements for each measurement type) for different blanking speeds are shown in Fig. 8 and the effect of the blanking speed on the shear ultimate τ_u and the yield τ_y stress during blanking in comparison to the tensile ultimate σ_u and yield σ_y stress is shown in Fig. 9. Yielding was determined by the use of partial blanking experiments (discussed later) and a linear approximation. It was determined from partial blanking experiments that the plastic deformation of the specimens occurred at an approximate punch penetration of 30 μm. A linear approximation was used on the $P-d$ data to acquire the blanking force at the yield.

The quasi-static ultimate shear stress is lower than the ultimate tensile stress (ratio about 1.06), whereas the dynamic ultimate shear stress is slightly higher than the ultimate tensile stress (ratio of approximately 0.99). In contrast, the yield shear stress is lower than the tensile yield stress (1.45), but it increases with the blanking speed (from about 1.30 at a blanking speed of 200 mm/s, and to 1.15 at a blanking speed of 350 mm/s).

Increase in process speed may lead to thermal softening of the material due to the heat generated inside the sheet-metal. The temperature increase during blanking was discussed in the literature from experimental and numerical point of view (see [24]), but for the material, presented in this study, no significant effects of generated heat were observed at different blanking speeds. Therefore the thermal effects will be disregarded in this study.

Table 1. *Material hardening parameters in the rolling direction, obtained from tensile tests*

Parameter	E_{rolling} [GPa]	σ_{y0} [MPa]	ε^{p0} [mm/mm]	K [MPa]	σ_∞ [MPa]	m
Value	175.6	273	0.0168	321.698	396.623	20.704

3.2.2 Damage Identification

For damage identification, partial (Fig. 10) and sequential (Fig. 11) quasi-static and dynamic blanking experiments were performed. As can be seen from Fig. 10, the partial dynamic experiments conform well with the full dynamic experiments. By lowering the initial kinetic energy of the punch for the stepwise experiments, the stepwise steps show a more quasi-static-like curve, but still follow closely the full experiments (Fig. 11).

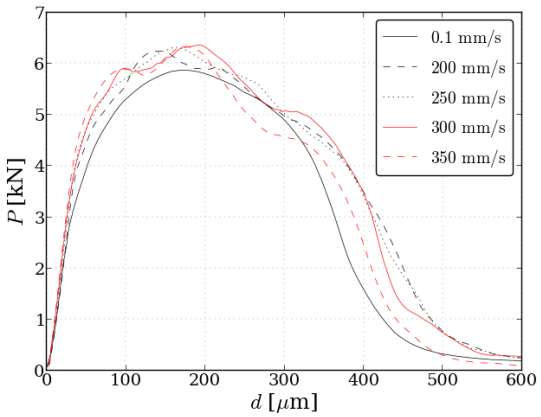

Fig. 9. *Averaged blanking diagrams at different blanking speeds*

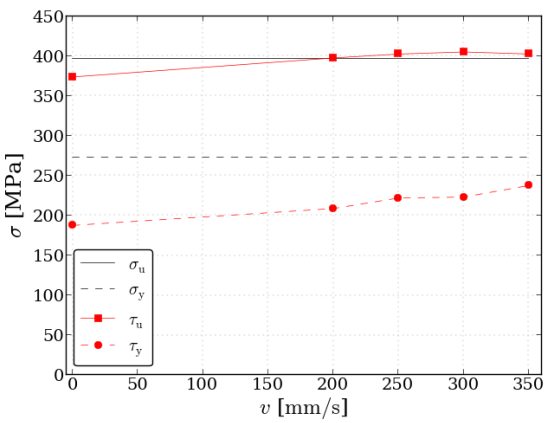

Fig. 10. *Correlation of uniaxial tensile and blanking yield and ultimate stresses*

The material degradation was determined, similar to the uniaxial tensile tests, by observing the gradient $G = \mathrm{d}P/\mathrm{d}d$ during the unloading phase of the blanking for the sequential steps (Fig. 12). In contrast to the tensile experiments, where the unloading slope of the curve is approximately linear, the blanking partial and sequential unloading curves exhibit non-linearities that are attributed to the contact conditions between the cutting tools and the specimen. Fig. 13 shows the identified unloading gradients for partial and sequential experiments at different punch penetration depths. The gradients for the unloading data increase approximately to the maximum blanking force and then start to decrease rapidly.

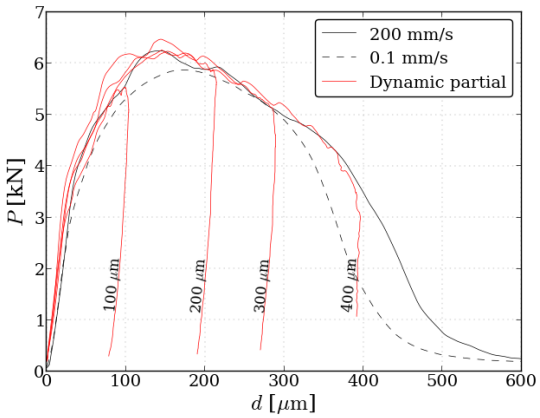

Fig. 11. *Averaged partial experiments*

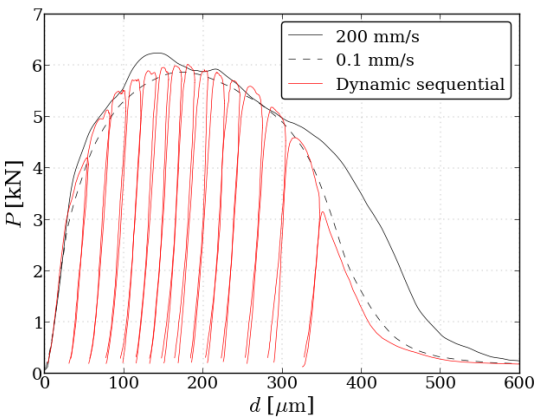

Fig. 12. *Averaged sequential dynamic blanking experiments*

For an approximately equal punch-penetration depth, similar gradient values are obtained from the quasi-static and the dynamic partial and sequential experiments. Only the small, 50 μm steps reveal the peak gradient at the maximum force depth. The P–d diagram up to the maximum force is usually assumed to show the hardening of the sheet-metal, followed by damage initiation and shearing after the force peak [29]. The shearing zone ends with an abrupt fracture of the sheet metal. By investigating metallographic samples, the fracture point was determined to be at approximately 350 μm. This can also be seen from the sequential experiments - even for sequential steps with a nominal depth of 50 μm, the final fracture occurred at a depth of approximately 350 μm.

A comparison of the damage accumulation during the uniaxial tensile experiment and of the damage-like

variable during the blanking experiment is shown in Fig 14.

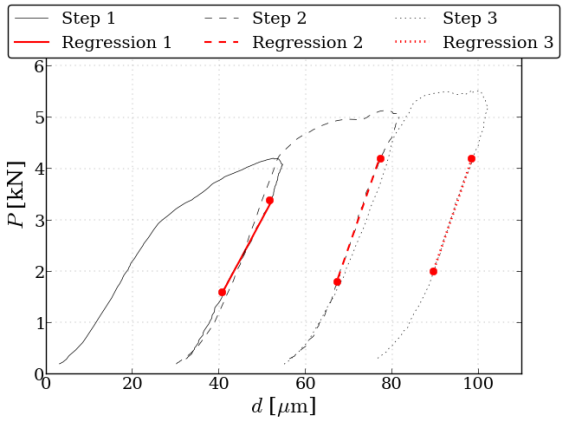

Fig. 13. *Identification of damage from sequential blanking experiments*

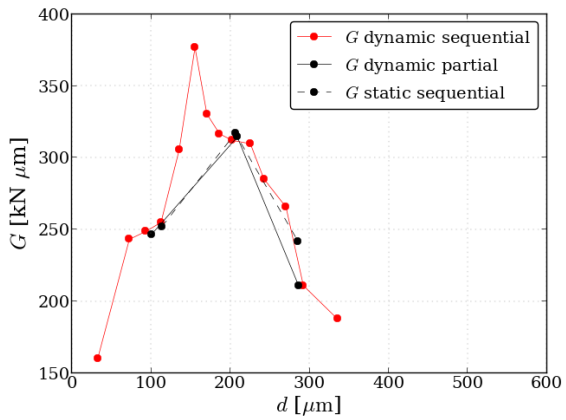

Fig. 14. *Damage at different punch penetrations for sequential and partial experiments*

As the strains during the blanking cannot be directly characterized, neither as pure tensile nor as pure shear strains [19] and [29], relative plastic displacement is used to compare the values of the damage variable during tensile and blanking experiments instead of the accumulated plastic strain.

The relative plastic displacement for the tensile experiment $d_{\mathrm{rel,t}}$ is determined as:

$$d_{\mathrm{rel,t}} = \frac{d_{\mathrm{y,t}}}{d_{\mathrm{f,t}}}, \tag{22}$$

where $d_{\mathrm{y,t}}$ is the displacement after the material yield and $d_{\mathrm{f,t}}$ is the displacement at fracture for the tensile experiment. The relative plastic displacement for the blanking experiment is determined as:

$$d_{\mathrm{rel,b}} = \frac{d_{\mathrm{p,b}}}{t}, \tag{23}$$

where $d_{\mathrm{p,b}}$ is the displacement after the peak force and t is the sheet-metal thickness. The damage coming from the blanking is characterized as:

$$D_{\mathrm{b}} = 1 - \frac{G}{G_0}, \tag{24}$$

G_0 represents the unloading gradient at the highest peak. A further analysis was performed, the same as with the data from the tensile experiments.

In the tensile experiments the Young's modulus was reduced from an initial 177 MPa to a final 94 MPa, or, about 46 %. Similarly, in the blanking experiments the gradient was reduced from the steepest 376 kN/mm to 160 kN/mm, which is about 57 %. This is consistent with the results obtained by [17].

However, the observation of the relative plastic displacement shows that, while during the uniaxial tensile experiment, damage accumulation starts almost immediately with the plastification, the accumulation of damage in the out-of-plane direction starts after the maximum force is reached, resulting in a smaller relative plastic displacement at fracture.

4 CONCLUSIONS

In this research, an experimental procedure to directly identify material parameters in the out-of-plane direction is proposed. The in-plane procedures from uniaxial tensile testing are implemented in the out-of-plane blanking experiments to determine shear yield and ultimate stresses and material damage accumulation up to fracture point. The out-of-plane values are compared to the values obtained from the uniaxial tensile experiment. Full, partial and sequential blanking experiments at various blanking speeds were performed to obtain the ultimate and the yield stress and the damage accumulation in relation to the punch depth in the out-of-plane direction. The damage was identified from the blanking force vs. punch penetration unloading gradient of the partial and sequential steps.

The damage initiation in the out-of-plane direction can only be observed with sufficiently small sequential steps, as can be seen from the results above. Furthermore, out-of-plane damage dependency on the step size and/or process speed needs to be assessed for the tested material using partial and sequential experiments with different step sizes.

Similarly, the yield and ultimate shear stresses should be tested at different process speeds in order to perform full correlation with the in-plane data. Furthermore, as the yield stress evaluation in the

out-of-plane direction is influenced by the material-punch contact conditions, additional care should be taken in order to ensure equal contact conditions (e.g. lubrication, tool wear, etc.), otherwise the parameter might monitor the variation of the contact conditions instead.

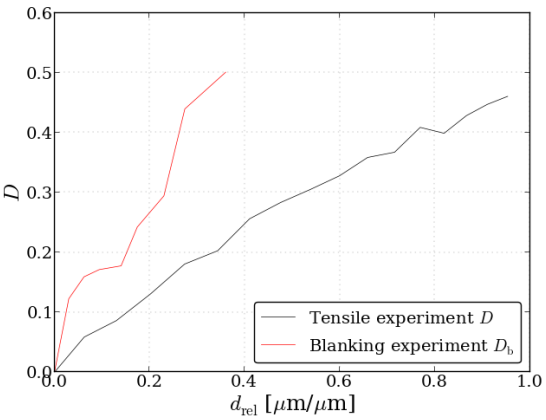

Fig. 15. *Correlation of tensile and blanking damage propagation up to fracture*

With the integration of the proposed procedure into an industrial blanking press, an on-line monitoring of the material quality could be obtained from which process monitoring and optimization could be achieved, for example by correlating the blanking speed to the material fracture point. Furthermore, with appropriate extensions to the Lemaitre damage model formulation, damage parameters for a fully anisotropic Lemaitre damage model could be determined.

5 ACKNOWLEDGEMENTS

This operation was partially financed by the European Union, European Social Fund (Grant nr. MR-10/103).

6 REFERENCES

[1] Cao, T.-S., Gachet, J.-M., Montmitonnet, P., Bouchard, P.-O. (2014). A Lode-dependent enhanced Lemaitre model for ductile fracture prediction at low stress triaxiality. *Engineering Fracture Mechanics*, vols. 124-125, p. 80-96, **DOI:10.1016/j.engfracmech.2014.03.021**.

[2] Li, H., Fu, M., Lu, J., Yang, H. (2011). Ductile fracture: Experiments and computations. *International Journal of Plasticity*, vol. 27, no. 2, p. 147-180, **DOI:10.1016/j.ijplas.2010.04.001**.

[3] Gurson, A.L. (1977). Continuum theory of ductile rupture by void nucleation and growth. Part I: yield criteria and flow rules for porous ductile media. *Journal of Engineering Materials and Technology*, vol. 99, no. 1, p. 2-15, **DOI:10.1115/1.3443401**.

[4] Tvergaard, V., Needleman, A. (1984). Analysis of the cup-cone fracture in a round tensile bar. *Acta Metallurgica*, vol. 32, no. 1, p. 157-169, **DOI:10.1016/0001-6160(84)90213-X**.

[5] Nahshon, K., Hutchinson, J. (2008). Modification of the Gurson model for shear failure. *European Journal of Mechanics - A/Solids*, vol. 27, no. 1, p. 1-17, **DOI:10.1016/j.euromechsol.2007.08.002**.

[6] Starman, B., Vrh, M., Halilovič, M., Štok, B. (2014). Advanced modelling of sheet metal forming considering anisotropy and Young's modulus evolution. *Strojniški vestnik - Journal of Mechanical Engineering*, vol. 60, no. 2, p. 84-92, **DOI:10.5545/sv-jme.2013.1349**.

[7] Saanouni, K. (2008). On numerical prediction of ductile fracture in metal forming. *Engineering Fracture Mechanics*, vol. 75, no. 11, p. 3545-3559, **DOI:10.1016/j.engfracmech.2007.02.023**.

[8] Lemaitre, J. (1985). A continuous damage mechanics model for ductile fracture. *Journal of Engineering Materials and Technology*, vol. 107, p. 83-89, **DOI:10.1115/1.3225775**.

[9] Ghozzi, Y., Labergere, C., Saanouni, K. Parrico, A. (2014). Modelling and numerical simulation of thick sheet double slitting process using continuum damage mechanics. *International Journal of Damage Mechanics*, vol. 23, no. 8, pp. 1150-1167, **DOI:10.1177/1056789514520799**.

[10] Lemaitre, J., and Desmorat, R. (2005). *Engineering Damage Mechanics*, Springer, Berlin, Heidelberg.

[11] Celentano, D.J., Chaboche, J.L. (2007). Experimental and numerical characterization of damage evolution in steels. *International Journal of Plasticity*, vol. 23, no. 10-11, p. 1739-1762, **DOI:10.1016/j.ijplas.2007.03.008**.

[12] Mashayekhi, M., Ziad-Rad, S., Parvizian, J., Niklewicz, J., Hadavinia, H. (2007). Ductile crack growth based on damage criterion: Experimental and numerical studies. *Mechanics of Materials*, vol. 39, no. 7, p. 623-636, **DOI:10.1016/j.mechmat.2006.10.004**.

[13] Hambli, R. (2001). Comparison between Lemaitre and Gurson damage models in crack growth simulation during blanking process. *International Journal of Mechanical Sciences*, vol. 43, no. 12, p. 2769-2790, **DOI:10.1016/S0020-7403(01)00070-4**.

[14] Teixeira, P., Santos, A.D., Pires, F.A., de Sa, J.M.A.C. (2006). Finite element prediction of ductile fracture in sheet metal forming processes. *Journal of Materials Processing Technology*, vol. 177, no. 1-3, p. 278-281, **DOI:10.1016/j.jmatprotec.2006.04.059**.

[15] Ganjiani, M. (2013). Identification of damage parameters and plastic properties of an anisotropic damage model by microhardness measurement. *International Journal of Damage Mechanics*, vol. 22, no. 8, p. 1089-1108, **DOI:10.1177/1056789513482598**.

[16] Desmorat, R., Otin, S. (2008). Cross-identification isotropic/anisotropic damage and application to anisothermal structural failure. *Engineering Fracture Mechanics*, vol. 75, no. 11, p. 3446-3463, **DOI:10.1016/j.engfracmech.2007.05.011**.

[17] Malcher, L., Mamiya, E. (2014). An improved damage evolution law based on continuum damage mechanics and its dependence on both stress triaxiality and the third invariant. *International Journal of Plasticity*, vol. 56, p. 232-261, **DOI:10.1016/j.ijplas.2014.01.002**.

[18] Mkaddem, A., Gassara, F., Hambli, R. (2006). A new procedure using the microhardness technique for sheet metal damage characterization. *Journal of Materials Processing Technology*, vol. 178, no. 1-3, p. 111-118, **DOI:10.1016/j.jmatprotec.2006.02.018**.

[19] Guduru, R.K., Darling, K.A., Kishore, R., Scattergood, R.O., Koch, C.C., Murty, K.L. (2005). Evaluation of mechanical properties using shear-punch testing. *Materials Science and Engineering: A*, vol. 395, no. 1-2, p. 307-314, **DOI:10.1016/j.msea.2004.12.048**.

[20] Sellamuthu, P., Collins, P.K., Hodgson, P.D., Stanford, N. (2013). Correlation of tensile test properties with those predicted by the shear punch test. *Materials & Design*, vol. 47, p. 258-266, **DOI:10.1016/j.matdes.2012.11.057**.

[21] Abendroth, M., Kuna, M. (2006). Identification of ductile damage and fracture parameters from the small punch test using neural networks. *Engineering Fracture Mechanics*, vol. 73, no. 6, p. 710-725, **DOI:10.1016/j.engfracmech.2005.10.007**.

[22] Mole, N., Cafuta, G., Štok, B. (2013). A method for optimal blank shape determination in sheet metal forming based on numerical simulations. *Strojniški vestnik - Journal of Mechanical Engineering*, vol. 59, no. 4, p. 237-250, **DOI:10.5545/sv-jme.2012.989**.

[23] Vrh, M., Halilovič, M., Štok, B. (2008). Impact of Young's modulus degradation on springback calculation in steel sheet drawing. *Strojniški vestnik - Journal of Mechanical Engineering*, vol. 54, no. 4, p. 288-296.

[24] Gantar, G., Sterzing, A. (2008). Robust design of forming processes, *Strojniški vestnik - Journal of Mechanical Engineering*, vol. 54, no. 4, p. 249-257.

[25] Vegelj, D., Zajec, B., Gregorčič, P., Možina, J. (2014). Adaptive pulsed-laser welding of electrical laminations. *Strojniški vestnik - Journal of Mechanical Engineering*, vol. 60, no. 2, p. 106-114, **DOI:10.5545/sv-jme.2013.1407**.

[26] Slavič, J., Bolka, Š., Bratuš, V., Boltežar, M. (2014). A novel laboratory blanking apparatus for the experimental identification of blanking parameters. *Journal of Materials Processing Technology*, vol. 214, no. 2, p. 507-513, **DOI:10.1016/j.jmatprotec.2013.10.006**.

[27] Kachanov, L. (1958). On creep rupture time. *Proc Acad Sci USSR Dlv Engn Sci*, p. 26-31,

[28] Lemaitre, J. (1992). *A Course on Damage Mechanics*. Springer, Berlin, Heidelberg, **DOI:10.1007/978-3-662-02761-5**.

[29] de Souza Neto, E.A., Perić, D., Owen, D.R.J. (2001). *Computational Methods for Plasticity: Theory and Applications*. John Wiley & Sons, Chichester, **DOI:10.1002/9780470694626**.

[30] Voce, E. (1948). A Practical Strain-Hardening Function. *Acta Metallurgia*, vol. 51, p. 219-226.

[31] Klingenberg, W., Singh, U.P. (2005). Comparison of two analytical models of blanking and proposal of a new model. *International Journal of Machine Tools and Manufacture*, vol. 45, no. 4-5, p. 519-527, **DOI:10.1016/j.ijmachtools.2004.09.002**.

Strojniški vestnik - Journal of Mechanical Engineering 61(2015)4, 227-236
DOI:10.5545/sv-jme.2014.2248
Original Scientific Paper
Received for review: 2014-10-18
Received revised form: 2015-01-23
Accepted for publication: 2015-02-09

Mechanical Characteristics of Two Environmentally Friendly Resins Reinforced with Flax Fibers

Dario Croccolo* – Massimiliano De Agostinis – Stefano Fini – Alfredo Liverani – Nicolò Marinelli – Eugenio Nisini – Giorgio Olmi
University of Bologna, Department of Industrial Engineering, Italy

In this paper, a comparison between the mechanical characteristics of two different natural fiber composites has been carried out. The two composites were made using two different environmentally friendly resins, but with the same flax fiber reinforcement. Thirty-two specimens were tested for tension, bending and shear. The results obtained in the tensile and bending tests are acceptable according to the Standards, whereas those of the shear tests were discarded, since the samples exhibited unacceptable failure modes. In light of the results obtained, both in terms of strength and stiffness, the isophthalic resin (181EN2X) outperformed the vinyl ester resin (VEef220ST). In the case of the isophthalic resin, microscopic observations showed a good adhesion between the matrix and the fiber, with a small amount of air inclusions. The present study demonstrates that the mechanical characteristics of flax reinforced and environmentally friendly resins are similar to those achievable with the same fibers using conventional resins.
Keywords: natural fibre composites, mechanical properties, flax, environmentally friendly resin

Highlights
- *Two different natural fiber composites have been compared.*
- *The two resins have wide applications in the marine industry.*
- *The two composites have been obtained with two different environmentally friendly resins.*
- *The mechanical properties of the manufactured composites have been determined.*
- *The mechanical properties of the Resin 181EN2X are significantly improved by the presence of the fiber reinforcement.*

0 INTRODUCTION

Over the past twenty years, polymer matrix composites reinforced with vegetable fibers have attracted great interest [1] and [2]. The increasing attention on these materials arises from both the excellent mechanical properties of vegetable fibers, such as high tensile strength for low density, low environmental impact, renewability, recyclability and low cost. Despite the good qualities of some types of vegetable fibers, such as flax, hemp and jute, vegetable fiber reinforced plastics are still mainly used for non-structural applications only. This is due to the low strength properties that can be achieved for the composite, despite its generally good impact resistance and low density. The mechanical response of a composite is strictly related to its structure [3] to [7]. The relatively poor mechanical properties of the vegetal fiber reinforced composites are usually due to the following: i) damage to the plant fibers during the extraction process, ii) variability of fiber characteristics depending on the source. Other drawbacks are the difficulty in finding fabrics specially made for composites, resulting in non-optimal orientation and volume fractioning of the fibers that can be obtained, and a poor affinity between the fiber and the matrix. Moreover, due to the short length of technical plant fibers, the reinforcement needs to be in the form of staple fiber yarns, which have a twisted structure. Although twisting facilitates yarn processing, it has several detrimental effects on the composites produced [8]. Natural fibers also have limited thermal stability and harsh environments may seriously affect their mechanical properties. There is, finally, a major drawback related to the application of natural fibers for the reinforcement of polymeric matrices: natural fibers exhibit high moisture absorption [9] due to the presence of hydroxyl and other polar groups in their constituents. In the present study, the mechanical characteristics of composites obtained using environmentally friendly polymer matrices, reinforced with flax fibers derived from the textile industry, were evaluated. The aim of the research is to assess the potential of low cost vegetable fiber reinforced plastics. An set of experiments was carried out in order to show whether the combination of flax fiber reinforcement and environmentally friendly resins could lead to high-performance materials, with comparable structural properties to other composites made using natural fibers and non-environmentally friendly polymer matrices.

*Corr. Author's Address: University of Bologna, Department of Industrial Engineering, Viale del Risorgimento 2, 40136 Bologna, Italy, dario.croccolo@unibo.it

1 STATE OF THE ART: VEGETABLE FIBERS AND RESINS

1.1 Vegetable Fibers

There are six basic types of natural fibers. They are classified as follows: bast fibers (jute, flax, hemp, ramie and kenaf), leaf fibers (abaca, sisal and pineapple), seed fibers (coir, cotton and kapok), core fibers (kenaf, hemp and jute), grass and reed fibers (wheat, corn and rice) and all other types (wood and roots) [10]. The best fibers are bast fibers and they are extracted from the stems of plants such as flax, jute and hemp. These fibers are composed of clusters made up of long elementary fibers. The elementary fibers have varying lengths depending on the kind of plant, ranging from 20 mm to 70 mm for flax against 2 mm to 3 mm for softwood. They have extremely thin cell walls (5 μm up to 15 μm) and a diameter between 15 μm and 35 μm [11]. These clusters of elementary fibers, whose cross section consists of 12 to 48 cells, are called technical fibers. Technical fibers are the basic element for both the textile industry and the preparation of composites. For example, flax technical fibers have lengths in the range 0.3 m to 0.6 m and diameters falling between 50 μm and 500 μm. As shown in Fig. 1, inside each technical fiber, the elementary fibers are joined together by a matrix (middle lamella) primarily consisting of pectin and hemicellulose (structures composed of low molecular weight polysaccharides). Typically, elementary fibers display a 5- to 7-edge polyhedral section, which improves the packaging capability with respect to a circular section. They consist mainly of cellulose, lignin and non-structural compounds such as waxes, salts and organic nitrogen compounds [11]. The structural characteristics of elementary fibers are mainly due to cellulose, which has a high molecular weight and a Young's modulus of E = 135 GPa [13].

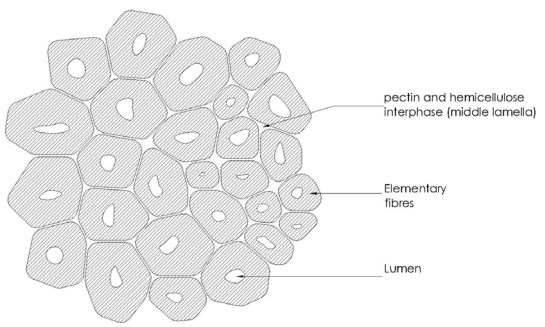

Fig. 1. *Cross section of a technical fiber (bundle of elementary fibers)*

Inside the cell wall, cellulose can be mainly found in the form of bundles of cellulose polymers, joined together by means of polysaccharides (hemicellulose) and lignin. The elementary fibers have an organized structure of multiple layers, with a very thin outer skin (the primary cell wall, for flax it is about 2 μm thick) and an intermediate zone (secondary cell wall), which is the main bearing element split into four parts. These are named S1 to S3, along with a hollow central part called the lumen (Fig. 2). The so-called S2 part is the most important in terms of volume amount, as it occupies about 80 % of the fiber volume. The secondary cell wall consists of cellulose microfibers spiral-wound with a certain tilt angle with respect to the elementary fiber axis. The secondary cell wall is included in a matrix of hemicellulose and lignin. In the S1 and S3 areas, microfibers are wound with both right hand and left hand helixes, hence forming a lattice structure. Conversely, in the S2 area, they are wound in one direction only and with a reduced helix angle in comparison with other areas. Referring to the S2 area, fibers derived from wood exhibit values for the tilt angle between 10° and 30°, whereas bast fibers have values lower than 10°, sometimes dropping down to as low as 2°.

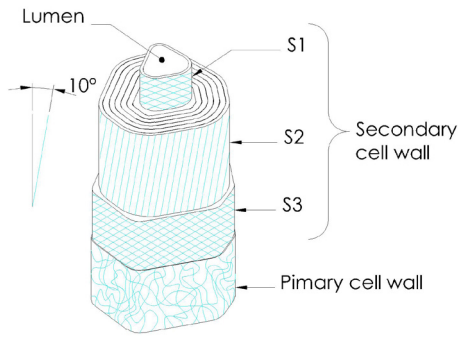

Fig. 2. *Structure of a bast elementary fiber*

It has been found that the mechanical properties of the fibers are related to the tilt angle in the S2 area. Small values of the tilt angle are generally associated with high values of tensile strength and of the elastic modulus of the elementary fiber. Therefore, the architecture of the S2 area is responsible for the tensile strength and the stiffness of the elementary fiber, the S1 area enhances the stability of the fiber against the compressive loads, whereas the S3 area reacts to the internal pressure of the cell [14]. The density of the cell wall is about 1500 kg·m^{-3} and appears to be almost independent of the plant species the fiber is extracted from. Conversely, the density of different plant fibers is mainly influenced by the extension of

the hollow central area (lumen) and, consequently, by the plant age. For instance, for fibers extracted from a mature plant, the lumen area is less than 10 % of the whole section of the fiber itself. Therefore, the average density of elementary fibers is quite low, on the order of 1350 kg·m^{-3}. As for the mechanical properties of the technical fibers, significant discrepancies can be found between the values reported by different authors [11] and [15] to [17]. This occurrence is due to one or more of the following reasons [18]: (a) cultivation of the fiber, growth conditions of the plant, position of the fiber in the plant, maturity of the fiber and collection technique; (b) machining and extraction technique or mechanical modification of the fiber [8]; (c) testing methodologies and measurements performed according to different standards, and different environmental conditions during the tests. Table 1 summarizes the main physical and mechanical properties found in the literature [18] to [20] for some natural fibers. The large scattering in the tensile strength values may depend on the clamping length. In fact, for clamping lengths greater than 25 mm, values of tensile strength of approximately $UTS = 500$ MPa can be found, whereas for lower clamping lengths (lower than 3 mm) the tensile strength may increase up to UTS = 800 MPa to 1000 MPa. Such behavior is due to the transition from a cohesive failure of the interface made of pectin adhesive, which joins the elementary fibers together, to the rupture of the elementary fibers themselves. Moreover, when the clamping length increases, more defects are found in the specimen [16].

1.2 Resins

The resins that are used in fibre-reinforced composites are composed of long chain-like molecules consisting of many simple repeating units. Resins can be classified under two types, 'thermoplastic' and 'thermosetting', according to the effect of heat on their properties. Thermoplastics are softened by heating and harden again after cooling. Widely used thermoplastics include nylon, polypropylene and ABS, which can be reinforced, usually by short, chopped fibres, such as glass. Thermosetting materials, or 'thermosets', are formed from an *in situ* chemical reaction, where the resin and hardener or the resin and catalyst are mixed together and undergo a non-reversible chemical reaction to form a hard, infusible product. Once cured, thermosets do not become liquid again if heated, although their mechanical properties experience a significant change above a certain temperature. This temperature is known as the glass transition temperature (Tg) and depends on the particular resin system used, on its degree of cure and on whether it was mixed correctly. Although there are many different types of thermosetting resins being used in the composite industry, the structural parts are mainly made of polyester, vinylester and epoxy. Most polyester resins are of the 'unsaturated' type. Unsaturated polyester resin is a thermoset, capable of being cured from a liquid or solid state under suitable conditions. Orthophthalic and isophthalic are the main types of polyester resins. The orthophthalic polyester resin is the most conventional and economical. The isophthalic resin is now becoming the preferred material in marine industries, due to its higher water resistance. The addition of styrene enables the resin to cure from a liquid to a solid by 'cross-linking' the molecular chains of the polyester. These resins can therefore be moulded without the use of pressure and are called 'contact' or 'low pressure' resins. Vinylester resins have a similar molecular structure, but different locations of their reactive sites, posed only at the ends of the molecular chains. An important issue is related to the molecular chain being able to absorb shock loads over its whole length. As a consequence, vinylester resins are made tougher and more resilient than polyesters. The vinylester molecule also features fewer ester groups. These ester groups commonly have a detrimental effect, as they suffer water degradation by hydrolysis. Therefore, a further important feature of vinylesters is their better resistance to water and many other chemicals than their polyester counterparts. Therefore, they are widely used in applications involving liquids, such as pipelines and chemical storage tanks. Epoxy resins are the resins exhibiting the best mechanical properties and a good resistance to environmental degradation, with many applications in aircraft construction. When used as laminating resins, their enhanced adhesive properties and resistance to water degradation, make them suitable to many applications in the marine industry.

2 MATERIALS AND METHODS

As mentioned in the introduction, the present study focuses on flax reinforced composites. In fact, flax is characterized by good mechanical and physical properties, such as tensile strength, elastic modulus, and density (Table 1), moreover its technical fibers are available in a wide variety of tissues. We chose a flax warp with a weight of 478 g·m^{-2}, whose properties are reported in Table 2 and provided by the Ta-Bru company. Since lamination was performed by

Table 1. *Physical and mechanical properties of some natural fibers*

	Diameter [μm]	Length [mm]	Density [kg·m^{-3}]	S2 spiral angle [°]	Tensile strength [MPa]	Elastic modulus [GPa]
sisal	20	1 to 8	1330	22	500 to 700	9 to 20
jute	20	2 to 5	1450	8	393 to 773	27
flax	13 to 22	20 to 70	1500	5 to 10	345 to 1100	28 to 100

hand, reduced environmental impact resins suitable for hand lamination were selected from among the class of thermosetting polymers. Thermosetting polymers have, in fact, good mechanical strength, chemical resistance, thermal stability and durability in comparison with thermoplastic resins. The latter, in spite of their better flexibility in terms of producing even complex shapes, have to reach process temperatures higher than the degradation threshold for flax (about 230 °C). In the set of thermosetting polymers available on the market and responding to the needs of low environmental impact, the authors have chosen two resins produced by the Polynt company. The first (Resin 181EN2X) is an isophthalic with 25% polyethylene terephthalate (PET), obtained from recycled material. The second (Resin VEef220ST) is a vinyl ester obtained from a bisphenolic epoxy resin with a low styrene content. Unlike the epoxy resins these two types of resins do not need thermal treatment after cure. In fact, thermal treatment may damage the flax fibres. The mechanical characteristics of the two resins are reported in Table 3 **[21]**. Considering the data reported in Table 3, it is possible to observe some differences between the isophthalic and the vinyl ester resins. In particular, the vinyl ester resin exhibits a lower elastic modulus and a higher ultimate strength than the isophthalic one. These different properties are in agreement with the related remarks in the Subsection 1.2, where it has been pointed out that a vinyl ester resin is more resilient than an isophthalic one. In order to investigate the mechanical properties of the manufactured composites, the tensile, the shear and the bending tests have been performed, following the most relevant standards **[22]** to **[25]**. The following instrumentation has been used: Instron 8033 standing press with a 25 kN load cell, MTS 3.1 station manager software, adjustable grips for tensile testing and an ad-hoc support for three-point loading, used for both bending and shear tests, according to **[24]** and**[25]**.

3 EXPERIMENTAL

3.1 Specimen Preparation

The specimens were prepared by hand, following the procedure described below: (a) spreading of a release agent on a glass plane, used as a base to facilitate the material removal at the end of the operations; (b) application of the first fabric layer, manually and uniformly wetted with the resin; (c) application of the second fabric layer, followed by manual application of the resin using a brush. The last operation was repeated until the desired thickness was reached.

After wetting the last layer, a layer of peel ply was applied on the top of the stack, in order to obtain a good surface finish.

Table 2. *Fabric properties*

	Units	Flax fabric 8615
Fiber content	[%]	100% flax
Specific weight	[g/m^2]	478
Yarns in warp	[threads/cm]	10
Warp count	[-]	22
Yarns in weft	[threads/cm]	5
Weft count	[-]	10

Table 3. *Mechanical properties of the resins*

		181EN2X	VEef220ST
Tensile strength	[MPa]	60	65
Young's modulus	[MPa]	4000	3500
Elongation at break	[%]	2	2
Flexural strength	[MPa]	98	105
Flexural modulus	[MPa]	4100	3600

After that, the peel ply was covered with a micro perforated film and an aerator layer. Then, the vacuum sack and the hoses for air extraction were applied. With a suitable choice of the porosity of the micro-perforated film, the excess resin distributed during the process was finally extracted, thus achieving the desired weight ratio between the matrix and the reinforcement. In the present experimentation, the weight was equally divided between the fibers and the resin, corresponding to a 0.5 matrix-reinforcement ratio. For tensile and bending tests, specimens made up of four layers, corresponding to an overall thickness of 3.5 mm ± 0.20 mm have been manufactured, whereas nine-layer, 8 mm ± 0.20 mm thick specimens, were prepared for the shear tests. In order to obtain the shapes prescribed by the standards, the plates were machined at low speed without cutting

oil [23], type 1 specimens with the dimensions shown in Fig. 3 were realized for the tensile tests. [24], method A (three-point bending) specimens with the dimensions shown in Fig. 4 were manufactured for the bending tests. In light of the difficulties encountered in manufacturing thin specimens, the specimens for the shear test were manufactured as shown in Fig. 5, following the procedure suggested by [24] for non-standard specimens. The whole set of specimens is characterized by a principal fiber orientation parallel to the greater dimension (length). The only fibers with perpendicular orientation with respect to the aforementioned direction are those needed for laying out the warp: they are on the order of 15% of the fabric by weight.

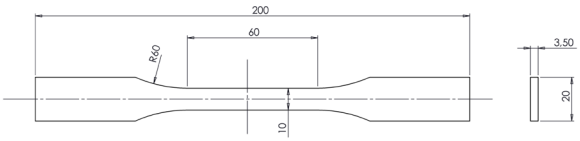

Fig. 3. *Specimen for tensile test*

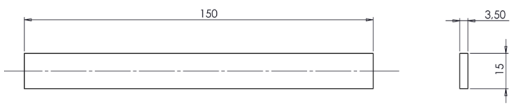

Fig. 4. *Specimen for bending test*

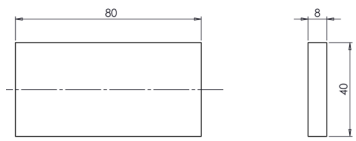

Fig. 5. *Specimen for interlaminar shear strength test (short-beam method)*

3.2 Testing

The tensile tests were performed according to [22] to [23]. Seven specimens for each resin were tested, at a room temperature (RT) of RT=23°C, and a relative humidity (φ) φ=50%. The standing press was equipped with a 25 kN load cell. The nominal strain was determined according to [22], method A. The same standard was used to evaluate the Young's modulus. Since results may be significantly affected by misalignments [26], the specimens were clamped by means of self-aligning grips, with a clamping length of 115 mm ± 1 mm. The velocity of the crosshead was set at 1.8 mm/min throughout the test.

The bending tests were run according to [24] standard, with a three-point bending loading configuration. The nominal span length of the specimen was L=60 mm. Six specimens for each resin were tested, at a room temperature of RT=23 °C and a relative humidity φ=50%. The standing press was equipped with a 25 kN load cell. The flexural modulus E_f was determined according to [24], method A. The crosshead velocity was set at 1mm/min throughout the test. The shear tests were run according to [25] standard. Six specimens were tested at a room temperature of RT=23 °C and a relative humidity φ=50%. The standing press was equipped with a 25 kN load cell. The crosshead velocity was set at 1 mm/min. At the end of each test, conducted under the aforementioned loading modes, the fracture surfaces were carefully examined in order to verify that the incurred failures conformed to the standard prescriptions.

3.3 Results

3.3.1 Tensile Tests

The results obtained for Resin 181EN2X and Resin VEef220ST are collected in Tables 4 and 5 and Figs. 7 and 8 respectively. Some data have been discarded (Rejected: Y) and were not considered for further analyses, as the cracking did not conform to [25] requirements.

3.3.2 Bending Test

Tables 6 and 7 and Figs. 9 and 10 show the bending test results for Resin 181EN2X and Resin VEef220ST, respectively.

Table 4. *Tensile test results for Resin 181 EN2X*

Specimen ID	σ_b [MPa]	E_t [MPa]	Rejected	σ_{bm} [MPa]	Std. dev. [MPa]	E_{tm} [MPa]	Std. dev [MPa]
1	76.91	5076	N				
2	77.43	4662	N				
3	79.94	5169	Y				
4	77.85	4898	N	75.24	3.80	4860	207
5	65.18	4679	Y				
6	68.64	4629	N				
7	75.38	5036	N				

Table 5. *Tensile test results for Resin VEef220ST*

Specimen ID	σ_b [MPa]	E_t [MPa]	Rejected	σ_{bm} [MPa]	Std. dev. [MPa]	E_{tm} [MPa]	Std. dev [MPa]
1	66.11	4698	Y				
2	72.14	4649	N				
3	70.48	4749	N				
4	73.39	4654	N	72.27	1.03	4822	158
5	71.95	4988	N				
6	73.01	4985	N				
7	72.65	4907	N				

Table 6. *Bending test results for Resin 181 EN2X*

Specimen ID	F_{max} [N]	σ_{fM} [MPa]	E_f [MPa]	Rejected	σ_{fMm} [MPa]	Std. dev. [MPa]	Efm [MPa]	Std. dev. [MPa]
1	0.232	113.6	4166	N				
2	0.235	115.1	4659	N				
3	0.201	98.45	3720	N				
4	0.187	91.59	4614	N	106.52	9.42	4437	414.2
5	0.222	108.7	4815	N				
6	0.228	111.7	4653	N				

Table 7. *Bending test results for Resin VEef220ST*

Specimen ID	F_{max} [N]	σ_{fM} [MPa]	E_f [MPa]	Rejected	σ_{fMm} [MPa]	Std. dev. [MPa]	Efm [MPa]	Std. dev.[MPa]
1	0.167	81.93	4368	N				
2	0.165	80.75	4503	N				
3	0.169	82.98	4301	N				
4	0.192	94.14	4906	N	83.05	5.73	4513	214
5	0.158	77.52	4435	N				
6	0.165	80.98	4570	N				

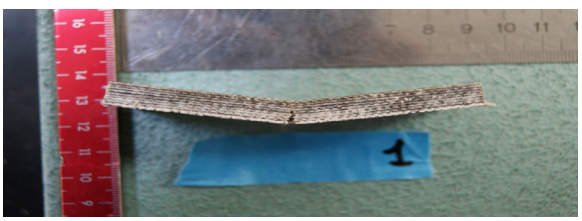

Fig. 6. *Specimen fractured in shear test*

3.4 Discussion

The data reported in Tables 4 and 5 for tensile tests and in Tables 6 and 7 for bending tests prove that the results are quite consistent with each other and repeatable. Moreover, the failure modes obtained comply with the relevant standards. Therefore, it may be concluded that both the matrix and the reinforcement contribute to the overall strength of the composite. On the other hand, results obtained in the shear test are not satisfactory due to an unacceptable failure mode of the whole set of specimens (Fig. 6). This outcome could be due to the characteristics of the laminated composite. The issue may be fixed by choosing a span length different from that suggested by the aforementioned standard, until an interlaminar failure mode is obtained. A comparison between the characteristics of the resins with and without reinforcement is reported in Table 8. The data referring to the resin without reinforcement are derived from [21] and are the same as those listed above in Table 3. In the case of resin 181 EN2X, the reinforcement increases the ultimate tensile strength UTS by about 25.4 %, the Young's modulus E_t by about 21.5 %, the flexural strength σ_{fM} by about 8.7 % and the flexural modulus E_f by about 8.2 % with respect to the resin itself. In the case of resin VEef220ST, the beneficial effect of the reinforcement is a bit less evident in tension strength. The results are slightly controversial in the case of the flexural response, since reinforcement leads to an increase in the elastic modulus, but produces a reduction in strength. Nevertheless, the reinforcement has a significant effect on improving the strength of the composites especially in the case of resin 181 EN2X, which behaves better than resin VEef220ST. The results obtained for the first one are consistent with those retrieved in the literature, even if some authors obtained better properties for similar composites [17], [18], [27] and [28]. The data for Table 8 are compared

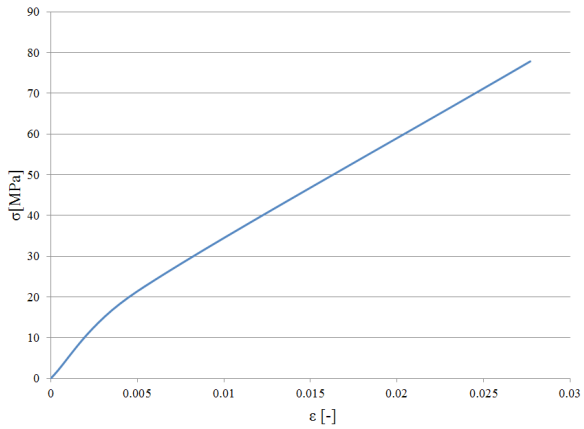

Fig. 7. *Tensile test for resin 181EN2X*

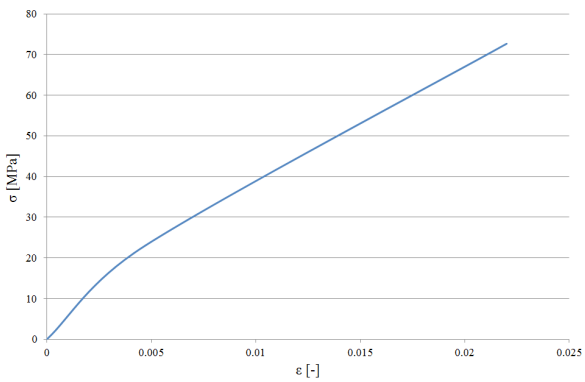

Fig. 8. *Tensile test for resin VEef220ST*

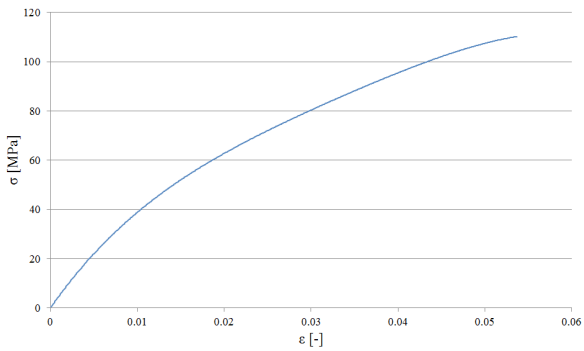

Fig. 9. *Bending test for resin 181EN2X*

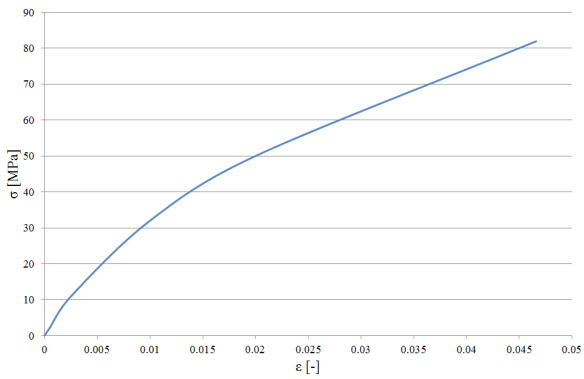

Fig. 10. *Bending test for resin VEef220ST*

to each other in the histograms of Figs. 11 and 12. Confidence intervals (±2·Std. Dev.) are added to account for the scatter in the results reported in Tables 4 to 7. The values of strengths and of elastic moduli for composites, having the same feature of being reinforced by flax fiber, but manufactured by conventional epoxy resins, are added in the bar graphs of Figs. 11 and 12 (data from **[28]**), as reference values. It can be remarked that, thanks to the enhancement provided by the reinforcement, the strength and the stiffness of the environmentally friendly composites made using flax fiber are comparable to those of the reinforced composites made using conventional resins.

In order to assess the matrix-reinforcement adhesion and the presence of defects, some specimens manufactured with the resin 181EN2X have been sectioned and then observed with an optical microscope. The assessment showed that the warp yarns have diameters of 500 μm to 600 μm (Fig. 13), whereas the weft yarns have diameters between 200 μm and 250 μm (Fig. 14). Air inclusions, shown in Fig. 15, are fewer and smaller with respect to the available data in the literature for composites manufactured for boat hulls. The analysis of the fracture surfaces of specimens tested in tension (Fig. 16) shows a homogeneous and regular surface. Such an occurrence demonstrates that both the matrix and the reinforcement participate together in the overall

Table 8. *Comparison of the characteristics of the resins with and without reinforcement*

	Resin 181EN2X [MPa]	Resin 181EN2X + 50% flax [MPa]	Variation [%]	Resin VEef220ST [MPa]	Resin VEef220ST + 50% flax [MPa]	Variation [%]
UTS	60	75.24	+25.4	65	72.27	+11.2
E_t	4000	4860	+21.5	3500	4822	+37.7
σ_{fM}	98	106.52	+8.7	105	83.05	–20.9
E_f	4100	4437	+8.2	3600	4513	+25.4

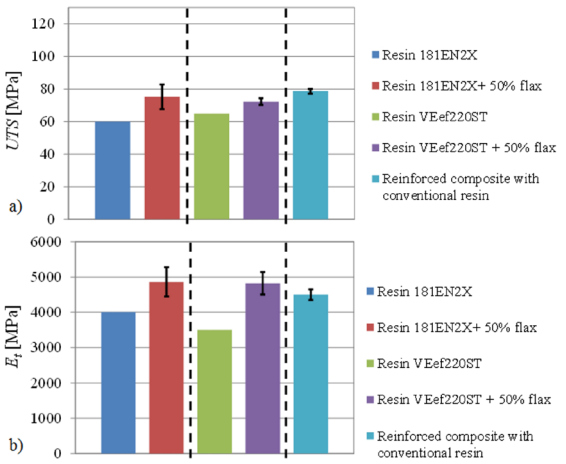

Fig. 11. *Comparison between a) the ultimate strengths and b) the Young's moduli of unreinforced and reinforced composites with environmentally friendly and conventional epoxy resins [28]*

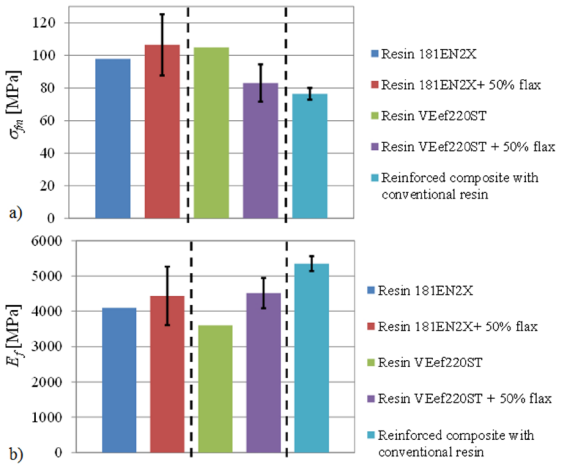

Fig. 12. *Comparison between a) the flexural strengths and b) the flexural Young's moduli of unreinforced and reinforced composites with environmentally friendly and conventional epoxy resins [28]*

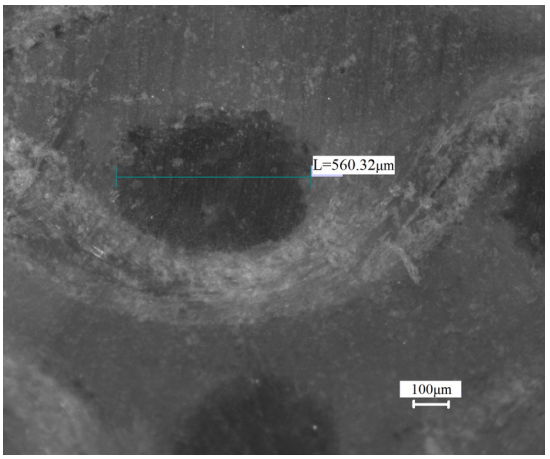

Fig. 13. *Cross section of a warp yarn*

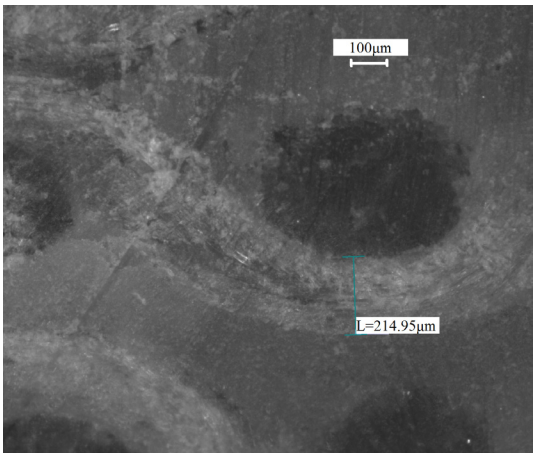

Fig. 14. *Cross section of a weft yarn*

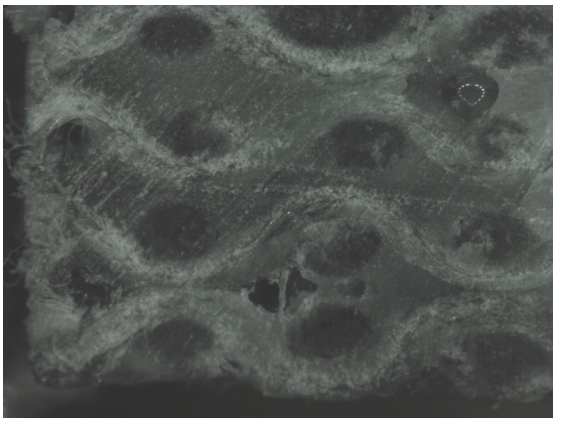

Fig 15. *Air inclusion in a sectioned specimen*

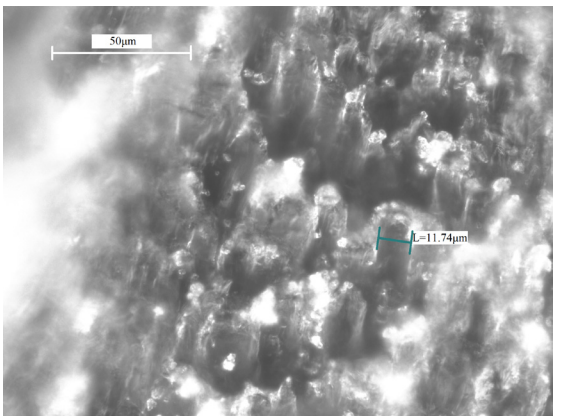

Fig. 16. *Fracture surface of a specimen broken in tension*

tensile strength of the composite. In other words, a good adhesion has been achieved between the two components. From the manufacturing standpoint, a drawback of the fibers used in the present study is that the fibers absorb a high amount of resin, making it

difficult to achieve a high reinforcement to the matrix ratio.

4 CONCLUSIONS

The present study compares the mechanical characteristics of two different composites made of natural fiber and obtained from two different environmentally friendly resins combined with the same flax fiber reinforcement. Thirty-two specimens were manufactured by hand. They were then tested for tension, bending and shear according to the relevant international standards. The results obtained in the case of tensile and bending tests are acceptable according to the standards, whereas those coming from the shear tests have been discarded, due to unacceptable failure modes observed. Therefore, the comparison was carried out based on solely the tensile and bending test results. In light of this, the isophthalic resin (181EN2X) showed a more uniform improvement in its properties with respect to the vinylester resin (VEef220ST) in terms of strength and stiffness. In the case of the isophthalic resin, microscopic observations showed a good adhesion between the matrix and the fiber, with a small amount of air inclusions. The outcome is that the mechanical properties of the isophthalic resin are remarkably enhanced by the presence of the fiber reinforcement. In other words, this kind of resin is able to take advantage of the presence of flax fibers. Conversely, the addition of the same fibers may even have a detrimental effect with regard to the vinyl ester resin. The results of the present study show that the mechanical characteristics of composites created using environmentally friendly resins can be compared with those achievable with similar fibers but created using conventional resins.

5 NOMENCLATURE

ε_{tb}	nominal strain at break [-];
σ_b	stress at break [MPa];
E_t	slope of the stress/strain curve in the strain interval between $\varepsilon_1 = 0.05$ % and $\varepsilon_2 = 0.25$ % [MPa];
σ_{bm}	average value of σ_b [MPa];
E_{tm}	average value of E_t [MPa];
σ_{fM}	flexural strength of the test specimen at maximum load [MPa];
E_f	flexural modulus of elasticity [MPa];
σ_{fMm}	average value of σ_{fM} [MPa];
E_{fm}	average value of E_f [MPa];
F_{max}	failure or maximum load [N];
UTS	ultimate tensile strength of the elementary fiber [MPa];
RT	room temperature [°C];
φ	relative humidity [-];
L	span length [mm];
b	specimen cross section width [mm];
h	specimen cross section height [mm].

6 REFERENCES

[1] Hornsby, P.R., Hinrichsen, E., Tarverdi, K. (1997). Preparation and properties of polypropylene composites reinforced with wheat and flax straw fibers – Part I Fibre characterization. *Journal of Materials Science*, vol. 32, no. 2, p. 443-449, **DOI:10.1023/A:1018521920738**.

[2] Hornsby, P.R., Hinrichsen, E., Tarverdi, K. (1997). Preparation and properties of polypropylene composites reinforced with wheat and flax straw fibers – Part II Analysis of composite microstructure and mechanical properties. *Journal of Materials Science*, vol. 32, no. 4, vol. 1009-1015, **DOI:10.1023/A:1018578322498**.

[3] Croccolo, D., De Agostinis, M., Olmi, G. (2013). Experimental characterization and analytical modelling of the mechanical behaviour of fused deposition processed parts made of ABS-M30. *Computational Materials Science*, vol. 79, p. 506-518, **DOI:10.1016/j.commatsci.2013.06.041**.

[4] Croccolo, D., De Agostinis, M. (2013). Analytical solution of stress and strain distributions in press fitted orthotropic cylinders. *International Journal of Mechanical Sciences*, vol. 71, p. 21-29, **DOI:10.1016/j.ijmecsci.2013.03.002**.

[5] Kopfer, H., Friedrich, C., De Agostinis, M., Croccolo, D. (2012). Friction characteristics in light weight design focusing bolted joints. *Proceedings of ASME International Mechanical Engineering Congress and Exposition*, Houston, vol. 3, p. 839-846, **DOI:10.1115/IMECE2012-85940**.

[6] Troiani, E., Donati, L., Molinari, G., Di Sante, R. (2014). Influence of plying strategies and trigger type on crashworthiness properties of carbon fiber laminates cured through autoclave processing. *Strojniški vestnik - Journal of Mechanical Engineering*, vol. 60, no. 6, p. 375-381, **DOI:10.5545/sv-jme.2013.1506**.

[7] Movaghghar, A., Lvov, G.I. (2012) Theoretical and experimental study of fatigue strength of plain woven glass/epoxy composite. *Strojniški vestnik - Journal of Mechanical Engineering*, vol. 58, no. 3, p. 175-182, **DOI:10.5545/sv-jme.2011.135**.

[8] Shah, D.U., Schubel, P.J., Clifford, M.J., (2013). Modelling the effect of yarn twist on the tensile strength of unidirectional plant fibre yarn composites. *Journal of Composite Materials*, vol. 47, no. 4, p. 425-436, **DOI:10.1177/0021998312440737**.

[9] Mukhopadhyay, S., Fangueiro, R. (2009). Physical modification of natural fibers and thermoplastic films for composites - A review. *Journal of Thermoplastic Composite Materials*, vol. 22, no. 2, p. 135-162, **DOI:10.1177/0892705708091860**.

[10] Faruk, O., Bledzki, A.K., Fink, H., Sain, M. (2012). Biocomposites reinforced with natural fibers: 2000-2010.

Progress in Polymer Science, vol. 37, no. 11, p. 1552-1596, **DOI:10.1016/j.progpolymsci.2012.04.003**.

[11] Hughes, M. (2012). Defects in natural fibres: their origin, characteristics and implications for natural fibre-reinforced composites. *Journal of Materials Science*, vol. 47, no. 2, p. 599-609, **DOI:10.1007/s10853-011-6025-3**.

[12] Baley, C. (2002). Analysis of the flax fibres tensile behavior and analysis of the tensile stiffness increase. *Composites - Part A: Applied Science and Manufacturing*, vol. 33, no. 7, p. 939-948, **DOI:10.1016/S1359-835X(02)00040-4**.

[13] Sakurada, I., Nukushina, Y., Taisuke, I. (1962). Experimental determination of the elastic modulus of crystalline regions in oriented polymers. *Journal of Polymer Science*, vol. 57, no. 165, p. 651-660, **DOI:10.1002/pol.1962.1205716551**.

[14] Booker, R.E. Sell, J. (1998). The nanostructure of the cell wall of softwoods and its functions in a living tree. *Holz als Roh - und Werkstoff (European Journal of Wood and Wood Products)*, vol. 56, no. 1, p. 1-8, **DOI:10.1007/s001070050255**.

[15] Symington, M.C., Banks, W.M., West, O.D., Pethrick, R.A. (2009). Tensil testing of cellulose based natural fibres for structural composite applications. *Journal of Composite Materials*, vol. 43, no. 9, p. 1083-1108, **DOI:10.1177/0021998308097740**.

[16] Bos, H.L., Van Den Oever, M.J.A., Peters, O.C.J.J. (2002). Tensile and compressive properties of flax fibres for natural fibre reinforced composites. *Journal of Materials Science*, vol. 37, no. 8, p. 1683-1692, **DOI:10.1023/A:1014925621252**.

[17] Zhu, J., Zhu, H., Njuguna, J., Abhyankar, H. (2013). Recent development of flax fibres and their reinforced composites based on different polymeric matrices. *Materials*, vol. 6, no. 11, p. 5171-5198, **DOI:10.3390/ma6115171**.

[18] Yan, L.A., Chouw, N.A., Jayaraman, K.B. (2014). Flax fibre and its composites - A review. *Composites Part B: Engineering*, vol. 56, p. 296-317, **DOI:10.1016/j.compositesb.2013.08.014**.

[19] Oksman, K., Mathew, A.P., Långström, R., Nyström, B., Joseph, K. (2009). The influence of fibre microstructure on fibre breakage and mechanical properties of natural fibre reinforced polypropylene. *Composites Science and Technology*, vol. 69, no. 11-12, p. 1847- 1853, **DOI:10.1016/j.compscitech.2009.03.020**.

[20] Ku, H., Wang, H., Pattarachaiyakoop, N. Trada, M. (2011). A review on the tensile properties of natural fiber reinforced polymer composites. *Composites Part B: Engineering*, vol. 42, no. 4, p. 856-873, **DOI:10.1016/j.compositesb.2011.01.010**.

[21] Polynt (2014), from *http://www.polynt.it/ENG/homepage.aspx*, accessed on 2014-06-10.

[22] ISO 2012.527-1 (2012). *Plastics-Determination of tensile properties-General principles, II ed.* International Organization for Standardization, Geneva.

[23] ISO 1997.527-4 (1997). *Plastics-Determination of tensile properties-Test conditions for isotropic and orthotropic fobre-reinforced plastic composites, I ed*. International Organization for Standardization, Geneva.

[24] ISO, 1998.14125 (1998). F*ibre-Renforced plastic composites-Determination of flexural properties, I ed.* International Organization for Standardization, Geneva.

[25] ISO 2003.14130 (2003). *Technical corrigendum 1. Fibre-Renforced plastic composites-Determination of apparent interlaminar shear strength by short-beam method*. International Organization for Standardization, Geneva.

[26] Olmi, G. (2011). A new loading-constraining device for mechanical testing with misalignment auto-compensation. *Experimental Techniques*, vol. 35 no. 6, p. 61-70, **DOI:10.1111/j.1747-1567.2010.00678.x**.

[27] Petrucci, R., Santulli, C., Puglia, D., Sarasini, F., Torre, L., Kenny, J. M. (2013). Mechanical characterisation of hybrid composite laminates based on basalt fibres in combination with flax, hemp and glass fibres manufactured by vacuum infusion. *Materials and Design*, vol. 49, p. 728-735, **DOI:10.1016/j.matdes.2013.02.014**.

[28] Fiore, V., Valenza, A., Di Bella, G., (2011). Mechanical behavior of carbon/flax hybrid composites for structural applications. *Journal of Composite Materials*, vol. 46, no. 17, p. 2089-2096, **DOI:10.1177/0021998311429884.**

Strojniški vestnik - Journal of Mechanical Engineering 61(2015)4, 237-244

DOI:10.5545/sv-jme.2014.2318 Original Scientific Paper
Received for review: 2014-11-21
Received revised form: 2015-01-15
Accepted for publication: 2015-02-06

Design Method of Dual Phase Hy-Vo Silent Chain Transmission System

Yabing Cheng* – Yang Wang – Lei Li – Shuaibing Yin – Lichi An – Xiaopeng Wang
Jilin University, School of Mechanical Science and Engineering, China

Based on the theory that the Hy-Vo silent chain meshes with the sprocket, and the related condition that the Hy-Vo silent chain sprocket meshes with a tool, multi-variations of the Hy-Vo silent chain and sprocket are designed. The meshing design system of the dual phase Hy-Vo silent chain plate-sprocket-tool is built. The design method of the dual phase Hy-Vo silent chain transmission system is presented. Combined with a concrete example, the dual phase Hy-Vo silent chain transmission system model is established, and the dual phase transmission system is decomposed into two single-phase transmission systems. The research shows that the instantaneous transmission ratio of a dual phase transmission system may be different from the instantaneous transmission ratio of a decomposed single-phase transmission system. If the two pitches of the dual phase sprocket are equal and the two groups of pressure angles are the same, the largest fluctuation quantity of the dual phase transmission system is less in comparison with the single-phase transmission system, and the polygon effect is smaller. The design method will provide a corresponding theoretical guidance for the design of other multi-phase chain systems.
Key words: dual phase transmission, Hy-Vo silent chain, multi-variation, fluctuation quantity, polygon effect

Highlights
- *Designed the multi-variation Hy-Vo silent chain and sprocket.*
- *Established the design system of the dual phase Hy-Vo silent chain plate-sprocket-tool.*
- *Studied the polygon effect through mathematical analysis and simulation analysis.*
- *Reduced the largest fluctuation quantity and the polygon effect of drive system.*
- *Provided the theoretical guidance for the design of multi-phase chain system.*

0 INTRODUCTION

The Hy-Vo silent chain is a series of high-end products in the field of mechanical transmission. In recent years, with the continuous development of high-speed chain transmission technology and the growth of different personalized needs regarding automotive engines, the Hy-Vo silent chain and sprocket have undergone a continuous variation development trend; this trend represents significant change and innovation for Hy-Vo silent chain transmission technology.

Research on Hy-Vo silent chain transmission systems has a long history. Meng et al. proposed the proper meshing conditions for the Hy-Vo silent chain and the sprocket [1], and the meshing system of the new silent chain plate-sprocket-hob was built; meanwhile, the design system of Hy-Vo silent chain transmission system was established [2] to [3], and the wear failure mechanism was explored through the road experiments [4] to [5]. Wang et al. designed a new sprocket tooth profile to reduce the polygonal action and meshing impact. If this method were adopted, the meshing impact and friction of the chain would be decreased [6]. Liu et al. changed the plate with a nano-structured metal mesh-polyurethane composite material, and proposed a new type of double pitch silent chain and a new silent chain assembly method [7] to [8]. Sun et al. obtained the ANSI sprocket tooth profile and involute sprocket tooth profile, and studied the effects of the dynamic tension of the chain in the silent chain drive [9]. Bucknor et al. developed a quasi-static model for a silent chain drive and modelled the kinematic effects of rocker-pin clearances [10]. Troedsson and Vedmar [11] and Stephenson et al. [12] researched the oscillations and forces of the chain drive; the model has been established to work at moderate and high speed conditions. Schwab et al. presented [13] a procedure to estimate the maximum contact force of the impact model, and Flores et al. [14] presented a general methodology to constrain rigid multibody systems. Based on these findings, Pereira et al. [15] built chain drive automatic multibody models from a minimal set of data, and aimed to overcome the difficulty of building manually complex models of chain drives.

At present, the multi-variation design on Hy-Vo silent chain and sprocket includes meshing mechanism variation, shape variation and parameter variation. The change process for meshing mechanism variation is outer meshing, inner-outer compound meshing and outer meshing with inner-outer compound meshing. "Shape variation" refers to major parts structure variations of Hy-Vo silent chains, such as plate hole shape variation, shape variation about pin

*Corr. Author's Address: Jilin University, School of Mechanical Science and Engineering, Renmin street 5988 , Changchun, China. chengyb@jlu.edu.cn

cross section, guide plate shape variation. "Parameter variation" refers to the main parameter variations of the Hy-Vo silent chain and sprocket, including the positioning offset angle variation, the distance variation of benchmark circle centre, apothem variation, big side surface curvature radius variation of rocker-pin, the variation of plate tooth profile angle, the variation of sprocket pressure angle, and the variation of tool normal tooth angle.

It should be noted that regardless of what the abovementioned variation is, they are all variations in the single-phase transmission system. In this paper, the variation of the transmission system is studied based on the single-phase Hy-Vo silent chain transmission system, the dual phase Hy-Vo silent chain transmission system is designed, and the multi-variation design method of the dual phase Hy-Vo silent chain plate and sprocket are proposed, and the fluctuation quantity of the dual phase Hy-Vo silent chain transmission system is researched.

1 THE MESHING DESIGN OF THE DUAL PHASE Hy-Vo SILENT CHAIN TRANSMISSION SYSTEM

1.1 The Parameter Design of the Dual Phase Hy-Vo Silent Chain Plate

Supposing that A is the hole pitch, P is the basic pitch. r is the big side surface curvature radius of the rocker-pin. S_m is the distance between the circle centre O of the chain plate hole and the big side surface of the rocker-pin. γ is the positioning offset angle when the rocker-pin is locked in the chain plate. α is the tooth profile angle of the Hy-Vo silent chain plate. f is the benchmark apothem between the circle centre O and chain plate outside linear profile. Fig. 1 shows the schematic diagram of the dual phase Hy-Vo silent

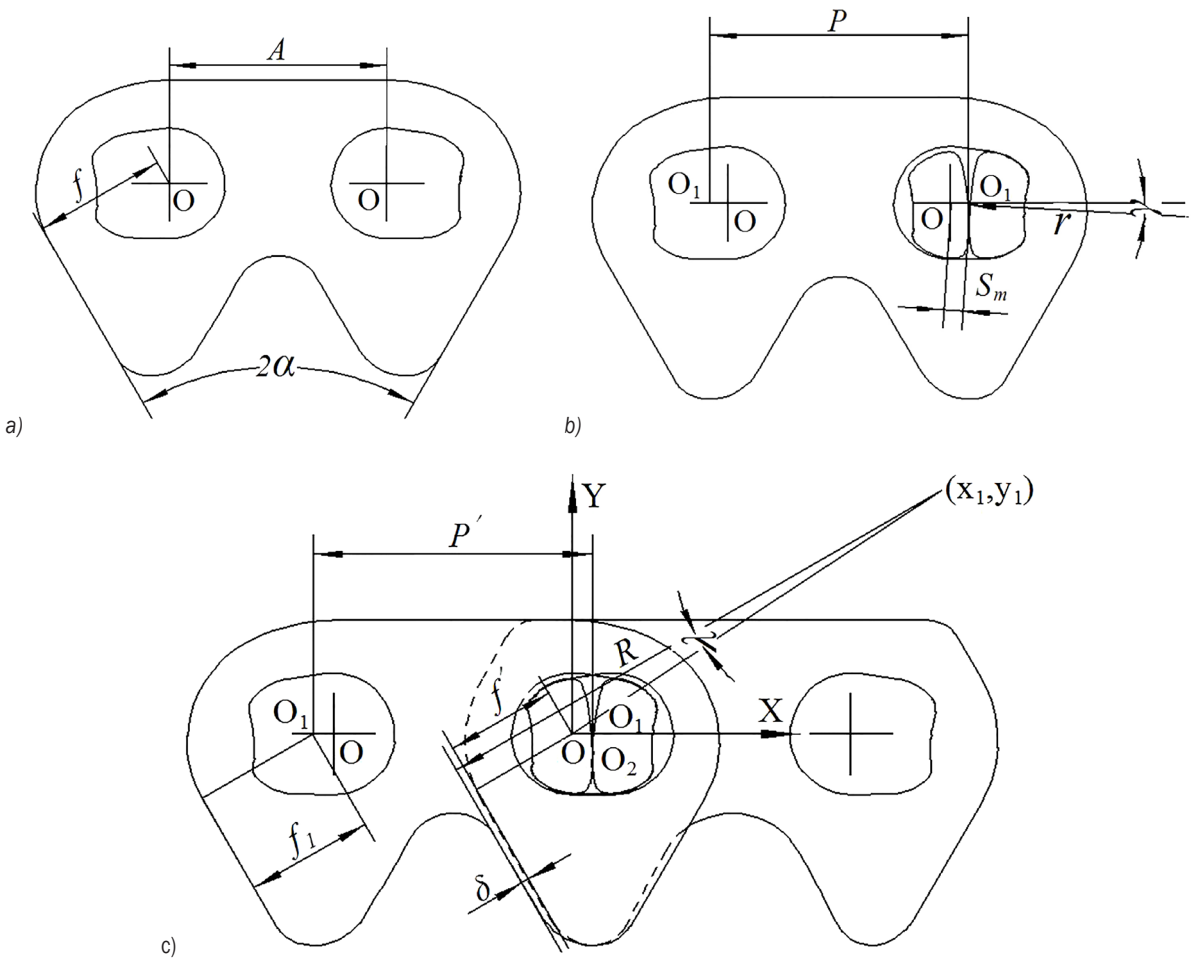

Fig. 1. *The schematic diagram of the dual phase Hy-Vo silent chain in straightening*

chain in straightening. The coordinate system *xoy* is established on the circle centre *O*. O_1 is the extension intersection of the adjacent benchmark circle centre lines. O_2 is the contact point of two rocker-pin at the action of tension.

Defining the distance of $O_1 - O_1$ as the pitch of the dual phase Hy-Vo silent chain, in straightening:

$$P' = P = A + 2\left[\left(r + S_m\right)\cos\gamma - r\right], \tag{1}$$

where f_1 is the equivalent apothem between the point O_1 and chain plate outside linear profile:

$$f_1 = f - \left[\left(r + S_m\right)\cos\gamma - r\right]\cos\alpha. \tag{2}$$

The inside profile overhang about the internal meshing plate is δ, and the tooth profile curvature is *R*. A straight line goes through the inside tooth profile curvature centre and the circle centre *O*, and another straight line is not only perpendicular to chain plate outside linear profile but also passes through the inside tooth profile curvature centre, and the angle between the two straight lines is λ. The coordinates of the inside tooth profile curvature centre is as follows:

$$\begin{cases} x_1 = \dfrac{\left(R - f' - \delta\right)\sin\left(\lambda + 60°\right)}{\cos\lambda} \\ y_1 = \dfrac{\left(R - f' - \delta\right)\cos\left(\lambda + 60°\right)}{\cos\lambda} \end{cases}, \tag{3}$$

where $f' = f - \left(p' - A\right)\cos\alpha$.

The load is transferred through the rolling role of the two rocker-pins in the dual phase Hy-Vo silent chain transmission system. When the adjacent links rotate mutually, the contact point in the big side surface of the rocker-pin will gradually move up, as shown in Fig. 2. The h_y is the distance between the point O_1 and the point O_2. When the relative angle of the adjacent links is 2θ:

$$h_y = \left(S_m + r\right)\sin\left(\gamma - \theta\right) + \\ + \tan\theta\left[\left(S_m + r\right)\cos\left(\gamma - \theta\right) - r\right]. \tag{4}$$

When $h_y > 0$, the point O_1 is below the point O_2. When $h_y = 0$, the point O_1 coincides with the point O_2. When $h_y < 0$, the point O_1 is above the point O_2.

At this moment, the working chain plate pitch is:

$$P'' = A + 2\left[\frac{r + S_m\cos\left(\theta - \gamma\right) - r}{\cos\theta}\right]. \tag{5}$$

Equivalent apothem f_1 is changed to:

$$f_2 = f - \left[\frac{\left(r + S_m\right)\cos\left(\theta - \gamma\right) - r}{\cos\theta}\right]\cos\alpha. \tag{6}$$

1.2 The Design System of the Dual Phase Hy-Vo Silent Chain Plate-Sprocket-Tool

The dual phase sprocket structure (with 35 teeth, for example) is shown in Fig. 3. Because the dual phase sprocket teeth have a phase difference, each phase tooth may have a difference in pitch, module, pressure angle parameters, and the tools processing each phase tooth are different. Supposing the dual phase sprocket pitches are P_{11} and P_{12}, the modules are m_{11} and m_{12}, and the pressure angles of sprockets are α_{11} and α_{12}.

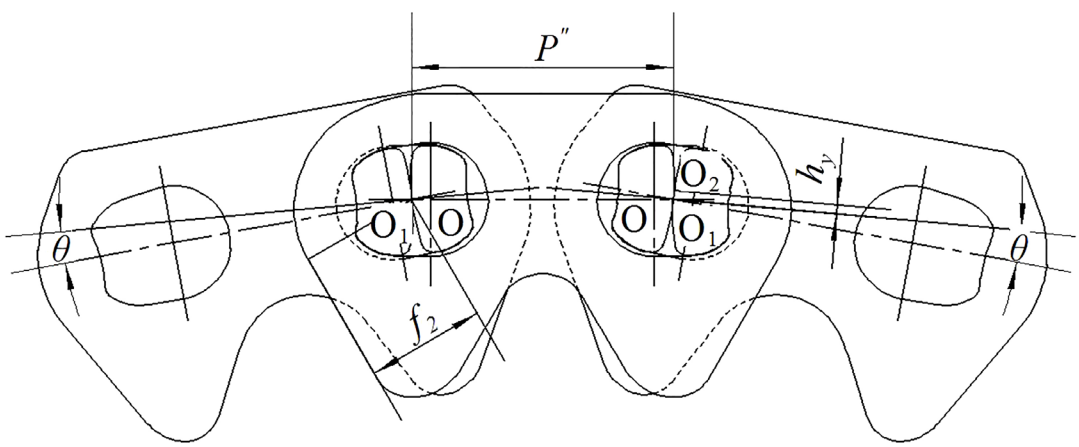

Fig. 2. *The rotation schematic of dual phase Hy-Vo silent chain*

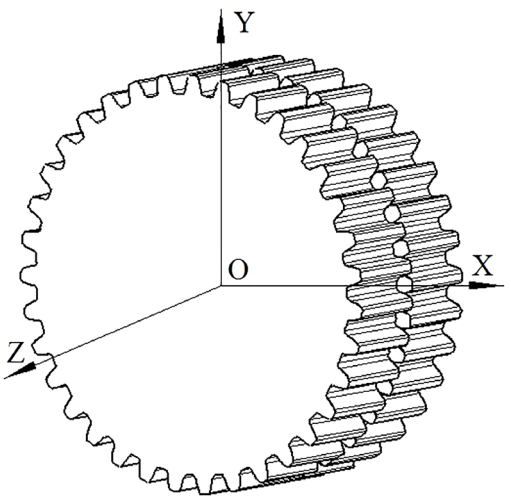

Fig. 3. *The schematic diagram of the dual phase sprocket*

The dual phase sprocket is projected onto *xoy*, as shown in Fig. 4. The solid line represents phase teeth whose sprocket tooth pitch is P_{11}, and the dotted line represents phase teeth that sprocket tooth pitch is P_{12}, and the phase difference of the sprocket tooth is σ. In the process of the chain plates are meshing with the dual phase sprocket, the working chain plate is regarded as a tool of the involute tooth. When the Hy-Vo silent chain plates are surrounding the dual phase transmission sprocket in the proper meshing place, the twining round is formed, and the twining round diameter is d_c. The tooth slot symmetric centreline is $n-n$. The tooth slot symmetric centreline is intersected with the twining round one point O_1. The first tool normal tooth angle is α_{21}, the first tool normal pitch is P_{21}, and the first tool module is m_{21}. According to conjugate meshing condition $P_{11}\cos\alpha_{11}=P_{21}\cos\alpha_{21}$ and making $\alpha_{21}=\alpha$, the first design system of the dual phase Hy-Vo silent chain plate-sprocket-tool is established. The dual phase sprocket centre is regarded as coordinate origin, the symmetrical centreline of the dual phase sprocket tooth is regarded as the vertical axis, the horizontal line that is through the centre of sprocket and vertical to the symmetrical centreline of the dual phase sprocket tooth is regarded as the horizontal axis, and the coordinate systems is established.

Supposing the Hy-Vo silent chain initial pitch is $P_{01}(P_{01}=P_{21})$ and the initial apothem is f_{01}, the meshing between the tool (P_{21},α_{21}) and the sprocket (P_{11},α_{11}) could be regarded as the meshing between the Hy-Vo silent chain $(P_{01},\alpha f_{01})$ and the sprocket (P_{11},α_{11}). If the dual phase sprocket tooth number is Z, and the relative rotating angle of the adjacent working plates is $2\theta=2\pi/z$.

The initial apothem f_{01} is:

$$f_{01}=f_2-\left(\cot\frac{\pi}{z}-\sqrt{3}\right)\left(P''-P_{21}\right)/4. \tag{7}$$

The modification coefficient x corresponds to the tool (P_{21},α_{21}) is:

$$x=\frac{\pi\cot\alpha_{21}}{4}-\frac{z}{2}+\frac{\pi}{2\tan\left(\pi/z\right)}-\frac{\pi f_{01}}{P_{21}\sin\alpha_{21}}. \tag{8}$$

When the outside linear profile of working link is fully meshed and located, providing AC is the involute tooth profile tangent line, the sprocket base circle radius is r_b, and the involute tooth profile is:

$$\Gamma\begin{cases}x=r_b\left(\sin\left(\varnothing+\theta\right)-\varnothing\cos\left(\varnothing+\theta\right)\right)\\ y=r_b\left(\cos\left(\varnothing+\theta\right)+\varnothing\sin\left(\varnothing+\theta\right)\right)\end{cases}. \tag{9}$$

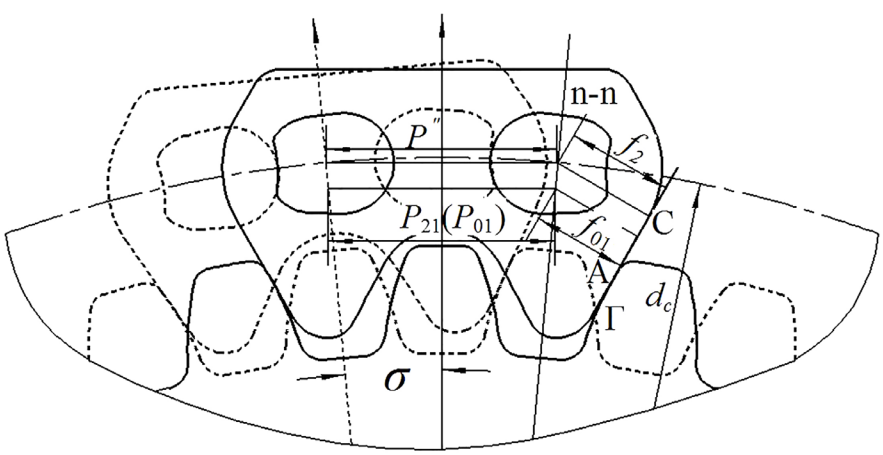

Fig. 4. *The design system of the dual phase Hy-Vo silent chain plate- sprocket–tool*

The coordinate of the point C is:

$$\begin{cases} x_C = \dfrac{P''}{2} + f_2 \cos\alpha \\ y_C = \dfrac{P''}{2} / \tan\dfrac{\pi}{z} - f_2 \sin\alpha \end{cases}, \quad (10)$$

the coordinate of the tangent point A is:

$$\begin{cases} x_A = r_b \sin\alpha - r_b \varnothing_A \cos\alpha \\ y_A = r_b \cos\alpha + r_b \varnothing_A \sin\alpha \end{cases}, \quad (11)$$

in which, $\varnothing_A = \dfrac{y_C \sin\alpha - x_C \cos\alpha}{r_b}$.

Assuming the diameter of the column is d_R, and when Z is an even number, the measuring distance of sprocket column is:

$$M_R = \frac{m_{21} z \cos\alpha_{21}}{\cos\alpha_{B1}} + d_R. \quad (12)$$

When Z is an odd number, the measuring distance of sprocket column is:

$$M_R = \frac{m_{21} z \cos\alpha_{21}}{\cos\alpha_{B1}} \cos\frac{90°}{z} + d_R. \quad (13)$$

α_{B1} is the involute pressure angle when the involute tooth profile is through the centre of sprocket column,

$$inv\alpha_{B1} = \frac{2x\tan\alpha_{21}}{z} + inv\alpha_{21} + \frac{d_R}{m_2 z \cos\alpha_{21}} - \frac{\pi}{2z}.$$

Assuming the first tool normal pitch P_{21} is equal to P_{11} and the first tool normal tooth angle α_{21} is equal to α_{11}, the modification coefficient x_1 corresponds to the tool ($P_{21}=P_{11}$, $\alpha_{21}=\alpha_{11}$) can be obtained by a transformation formula which is:

$$\frac{2x_1\tan\alpha_{21}}{z} = inv\alpha_{B1} - inv\alpha_{21} - \frac{d_R}{m_{21} z \cos\alpha_{21}} + \frac{\pi}{2z}. \quad (14)$$

Similarly, the second design system of dual phase Hy-Vo silent chain plate-sprocket -tool is established by using another dual phase sprocket pitch P_{12}, module m_{12}, pressure angle of sprocket α_{12}.

2 DESIGN EXAMPLE

The basic pitch of dual phase Hy-Vo silent chain P is 9.525 mm; the hole pitch A is 8.16 mm; the big side surface curvature radius of the rocker-pin r is 7.4 mm; the distance between the circle centre O of chain plate hole and the big side surface of the rocker-pin S_m is 0.7 mm; the positioning offset angle that rocker-pin is locked in the chain plate γ is 3.667°; the tooth profile angle of Hy-Vo silent chain plate α is 30°; the benchmark apothem between the circle centre O, and the chain plate outside linear profile f is 5 mm.

According to the Eq. (1),

$$P' = A + 2\left[\left(r + S_m\right)\cos\gamma - r\right] = 9.5268 \text{ mm}.$$

Making $\delta = 0.10 \sim 0.30$ mm, $R = 93$ mm, $\lambda = 1.6°$, according to the Eq. (3), it could obtain:

$$\begin{cases} x_1 = \dfrac{\left(R - f' - \delta\right)\sin\left(\lambda + 60°\right)}{\cos\lambda} = 78.287 \\ y_1 = \dfrac{\left(R - f' - \delta\right)\cos\left(\lambda + 60°\right)}{\cos\lambda} = 42.33 \end{cases}.$$

Making $P_{11}=P_{12}=P=9.523$ mm, $\alpha_{11}=\alpha_{12}=31.5°$, $\sigma = \pi/z$.

When $Z=35$, $2\theta = 2\pi/z$.

According to the Eq. (5),

$$P'' = A + 2\left[\frac{r + S_m\cos\left(\theta - \gamma\right) - r}{\cos\theta}\right] = 9.5603 \text{ mm}.$$

According to the Eq. (7),

$$f_{01} = f_2 - \left(\cot\frac{\pi}{z} - \sqrt{3}\right)\left(P'' - P_{21}\right)/4 = 3.966 \text{ mm}.$$

According to the Eq. (8), the modification coefficient x corresponds to the hob (P_{21}, α_{21}) is:

$$x = \frac{\pi\cot\alpha_{21}}{4} - \frac{z}{2} + \frac{\pi}{2\tan\left(\pi/z\right)} - \frac{\pi f_{01}}{P_{21}\sin\alpha_{21}} = -1.344,$$

so the modification coefficient x corresponds to the hob (P_{22}, α_{22}).

Making $d_R = 5.225$ mm, according to the Eq. (13),

$$M_R = \frac{m_{21} z \cos\alpha_{21}}{\cos\alpha_{B1}} \cos\frac{90°}{z} + d_R = 103.239 \text{ mm},$$

according to Eq. (14), the modification coefficient x_1 corresponds to the tool ($P_{21}=P_{11}$, $\alpha_{21}=\alpha_{11}$) can be got, $x_1=-1.531$, so the modification coefficient x_1 corresponds to the tool ($P_{22}=P_{12}$, $\alpha_{22}=\alpha_{12}$).

When $Z=35$, $x=-1.319$, $M_R=109.456$ mm, $x_1=-1.523$.

3 THE FLUCTUATION ANALYSIS OF THE DUAL PHASE TRANSMISSION SYSTEM

3.1 Fluctuation Quantity Mathematical Analysis

Based on the above design example, the dual phase Hy-Vo silent chain transmission system is built, as shown in Fig. 5. The transmission system is decomposed into two single-phase Hy-Vo silent chain transmission systems. Fig. 6 shows a single-phase Hy-Vo silent chain transmission system that the top of sprocket tooth is up, while Fig. 7 shows a single-phase Hy-Vo silent chain transmission system so that the slot of the sprocket tooth is up.

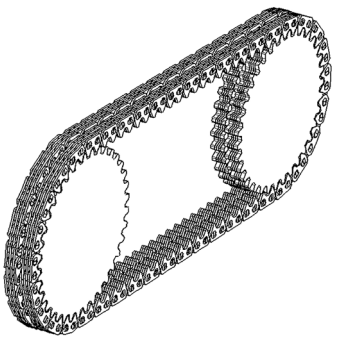

Fig. 5. *The dual phase Hy-Vo silent chain transmission system*

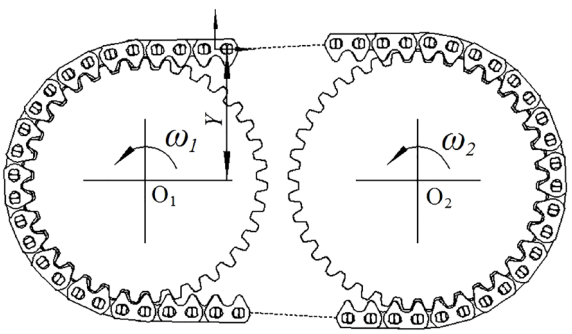

Fig. 6. *Single-phase Hy-Vo silent chain transmission system that the top of the sprocket tooth is up*

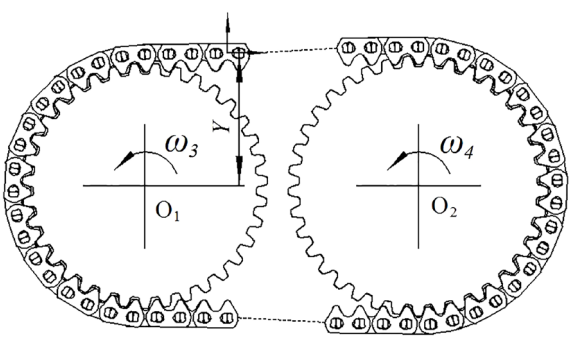

Fig. 7. *Single-phase Hy-Vo silent chain transmission system that the slot of the sprocket tooth is up*

The instantaneous transmission ratio in Fig. 6 is $i_1=\omega_1/\omega_2$, and the instantaneous transmission ratio in Fig. 7 is $i_2=\omega_3/\omega_4$. When two single-phase Hy-Vo silent chain transmission systems in Figs. 6 and 7 are engaging independently and simultaneously, at any time, i_1 is not necessarily equal to i_2, but in the dual phase transmission system, $i_1=i_2$. The instantaneous transmission ratio of dual phase transmission system may be different from the instantaneous transmission ratio of decomposed independently operating single-phase transmission systems, and the different instantaneous transmission ratio has a different effect on the tight-side centreline fluctuation quantity and the polygon effect; therefore, the tight-side centreline fluctuation quantity in the dual phase transmission system will be different from the fluctuation quantity in the independent operation single-phase transmission system .

The Fourier series of period $T=2\pi$ about two hanging tight side fluctuations is established. Because $\sigma=\pi/z$, the Fourier series phase difference is π. It is assumed that fluctuation functions are:

$$\begin{cases} f_1=\sum_1^{\infty}\left[a_n\cos(kt)+b_n\sin(kt)\right] \\ f_2=\sum_1^{\infty}\left[a_n\cos(kt+\pi)+b_n\sin(kt-\pi)\right] \end{cases}. \quad (15)$$

Therefore, for the round pin silent chain system, the outer meshing Hy-Vo silent chain system and the inner-outer compound meshing Hy-Vo silent chain system, $f_1+f_2=0$, namely, the fluctuation quantity of two tight sides can be superimposed on a straight line in the dual phase Hy-Vo silent chain transmission system. For the new type Hy-Vo silent chain systems that include outer meshing Hy-Vo silent chain and the inner-outer compound meshing Hy-Vo silent chain, $f_1+f_2\approx 0$, namely, the fluctuation quantity of two tight side can be superimposed on a straight line approximately.

3.2 Fluctuation Quantity Simulation Analysis

The silent chain polygon effect has an important role in the stability of chain transmission process and the reduction of vibration noise. The tight-side centreline fluctuation quantity is the important indicator of the silent chain polygon effect. Based on the above design example, the new type Hy-Vo silent chain system model of the single-phase transmission is established, as shown in Fig. 8; so does the new type Hy-Vo silent chain system model of the dual phase transmission, as

shown in Fig. 9. The tight-side centreline fluctuation quantity is extracted, and the silent chain polygon effect is studied.

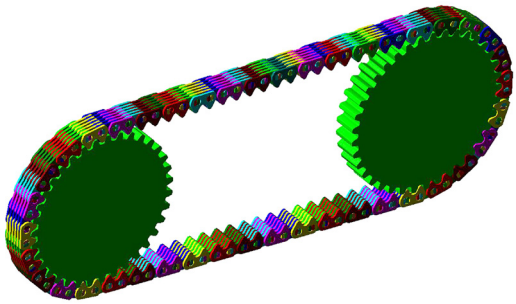

Fig. 8. *The new type Hy-Vo silent chain system model of the single-phase transmission*

The largest fluctuation quantity in a meshing period is extracted, Fig. 10 shows the largest fluctuation quantity about the single-phase transmission system. The horizontal axis is the time *t*, and the vertical axis *Y* is the coordinate whose link plate centroid is in the vertical direction. The parameter *Y* is illustrated in Figs. 6 and 7, and the maximum fluctuation quantity of the measuring link plate is 0.40 mm.

Fig. 11 shows the largest fluctuation quantity about the dual phase transmission system and the maximum fluctuation quantity of the measuring link plate is 0.26 mm. In comparison with the new type Hy-Vo silent chain system of the single-phase transmission, the largest fluctuation quantity about the new type Hy-Vo silent chain system of the dual phase transmission is reduced by 35 percent, and the polygon effect of dual phase transmission system is smaller.

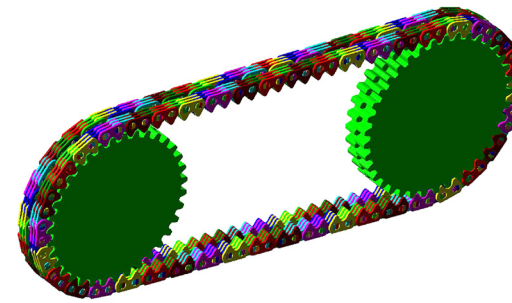

Fig. 9. *The new type Hy-Vo silent chain system model of the dual phase transmission*

4 CONCLUSIONS

(1) Based on the theory that the Hy-Vo silent chain plate profile is regarded as a tool profile of involute tooth, The meshing design system of

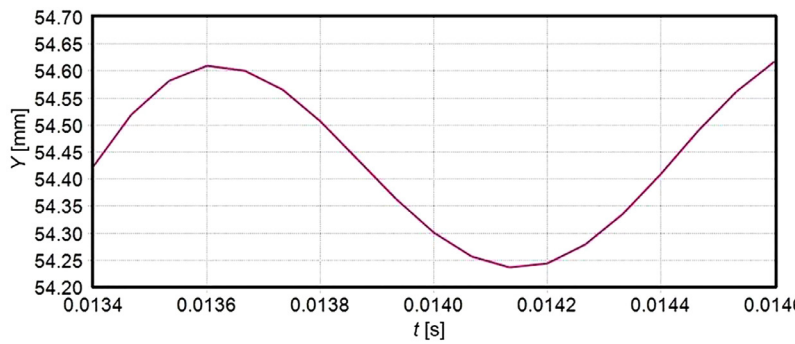

Fig. 10. *The largest fluctuation quantity about the single-phase transmission system*

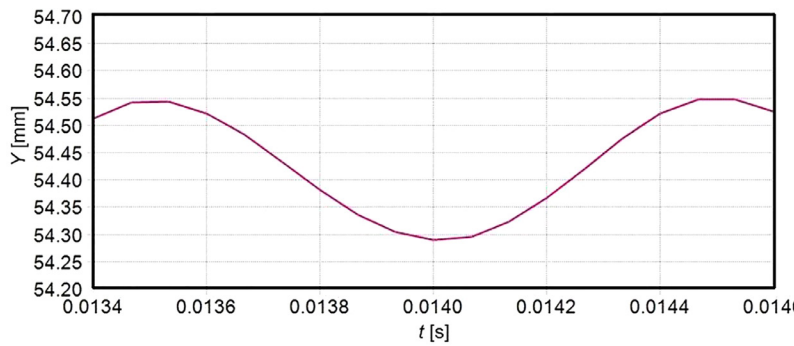

Fig. 11. *The largest fluctuation quantity about the dual phase transmission system*

Hy-Vo silent chain-sprocket-tool is established. It is not only suitable for the design of the single-phase Hy-Vo silent chain transmission system, but also for the design of the dual phase Hy-Vo silent chain transmission system, the design method of the dual phase Hy-Vo silent chain plate-sprocket-tool is a new kind of design method.

(2) If $P_{11} \neq P_{12}$ or $\alpha_{11} \neq \alpha_{12}$, the two design system of the dual phase Hy-Vo silent chain plate- sprocket-tool will be different. If $P_{12} \neq P_{22}$, $\alpha_{12} \neq \alpha_{22}$, the design system of the dual phase Hy-Vo silent chain plate-sprocket-tool can be built through the relevant parameters transformation.

(3) When $P_{11} = P_{12}$ or $\alpha_{11} = \alpha_{12}$, the instantaneous transmission ratio of dual phase transmission system may be different from the instantaneous transmission ratio of decomposed independent operation single-phase transmission system. In comparison with the single-phase transmission system, the polygon effect of dual phase transmission system is smaller.

5 ACKNOWLEDGEMENTS

The research presented in this paper was supported by National Natural Science Foundation of China (No. 51305154).

6 REFERENCES

[1] Meng, F., Li, C., Cheng, Y. (2007). Proper conditions of meshing for Hy-Vo silent chain and sprocket. *Chinese Journal of Mechanical Engineering*, vol. 20, no. 4, p. 57-59. (in Chinese)

[2] Liu, X. Ding, S. Sun, W. Liu, J. Lu, J. Xu, M. (2011). Study on join fastness of silent chain. *Proceedings of International Conference on Management Science and Intelligent Control*, p. 275-278. (in Chinese)

[3] Meng, F., Feng, Z., Chu, Y. (2006). Meshing theory and design method of new silent chain and sprocket. *Chinese Journal of Mechanical Engineering*, vol. 19, no. 3, p. 425-427, **DOI:10.3901/CJME.2006.03.425**. (in Chinese)

[4] Meng, F., Liu, X., Xu, S. (2008). Meshing analysis and design of rotundity-datum-aperture Hy-Vo silent chain. *Proceedings of the Institution of Mechanical Engineers, Part C: Journal of Mechanical Engineering Science*, vol. 222, no. 7, p. 1297-1303, **DOI:10.1243/09544062JMES865**.

[5] Meng, F., Wang, S., Lan, H., Xu, R., Xu, H. (2005). Wear failure mechanism and multi-impact property of automotive engine chain. *Chinese Journal of Mechanical Engineering*, vol. 18, no. 3, p. 401-404, **DOI:10.3901/CJME.2005.03.401**. (in Chinese)

[6] Cheng, Y., Meng, F., Xu, H., Wu, J. (2007). Experimental study on high speed characteristics of automotive engine Oil-pump chain. *Chinese Journal of Mechanical Engineering*, vol. 20, no. 1, p. 36-39, **DOI:10.3901/CJME.2007.01.036**. (in Chinese)

[7] Wang, Y., Ji, D., Zhan, K., (2013). Modified sprocket tooth profile of roller chain drives. *Mechanism and Machine Theory*, vol. 70, p. 380-393, **DOI:10.1016/j.mechmachtheory.2013.08.006**.

[8] Liu, X., Wang, W., Sun, W., Wu, T., Liu, J.., Liu, J.. (2012). Design and experimental analyse of low noise double-pitch silent chain for conveyor. *Procedia Engineering*, vol. 29, p. 2146-2150, **DOI:10.1016/j.proeng.2012.01.277**.

[9] Sun, W., Liu, X., Liu, J. (2012). Experimental investigation of sprocket tooth form effect on dynamic tension of silent chain. *Research Journal of Applied Sciences, Engineering and Technology*, vol. 4, no. 7, p. 846-850.

[10] Bucknor, N.K., Freudenstein, F. (1994). Kinematic and static force analysis of rocker-pin jointed silent chains with involute sprockets. *ASME Journal of Mechanical Design*, vol. 116, no. 3, p. 842-848, **DOI:10.1115/1.2919458**.

[11] Troedsson, I., Vedmar, L. (2001). A dynamic analysis of the oscillations in a chain drive. *ASME Journal of Mechanical Design*, vol. 123, no. 3, p. 395-401, **DOI:10.1115/1.1374196**.

[12] Stephenson, R., Glennie, D., Fawcett, J.N., Hale, J.M. (2000). A method of measuring the dynamic loads in high-speed timing chains. *Proceedings of the Institution of Mechanical Engineers, Part D: Journal of Automobile Engineering*, vol. 214, no. 2, p. 217-226, **DOI:10.1177/095440700021400211**.

[13] Schwab, A.L., Meijaard, J.P., Meijers, P. (2002). A comparison of revolute joint clearance models in the dynamic analysis of rigid and elastic mechanical systems. *Mechanism and Machine Theory*, vol. 37, no. 9, p. 895-913, **DOI:10.1016/S0094-114X(02)00033-2**.

[14] Flores, P., Ambrósio, J., Claro, J.C.P., Lankarani, H.M., Koshy, C.S. (2009). Lubricated revolute joints in rigid multibody systems. *Nonlinear Dynamics*, vol. 56, no. 3, p. 277-295, **DOI:10.1007/s11071-008-9399-2**.

[15] Pereira, C.M., Ambrósio, J.A., Ramalho, A.L. (2010). A methodology for the generation of planar models for multibody chain drives. *Multibody System Dynamics*, vol. 24, no. 3, p. 303-324, **DOI:10.1007/s11044-010-9207-x**.

Strojniški vestnik - Journal of Mechanical Engineering 61(2015)4, 245-253
DOI:10.5545/sv-jme.2014.2345
Original Scientific Paper
Received for review: 2014-12-02
Received revised form: 2015-01-21
Accepted for publication: 2015-02-05

Surface Roughness Control Simulation of Turning Processes

Franci Čuš – Uroš Župerl*
University of Maribor, Faculty of Mechanical Engineering, Slovenia

The aim of this paper is to present a surface roughness control in turning with an associated simulation block diagram. The objective of the new model based controller is to assure the desired surface roughness by adjusting the machining parameters and maintaining a constant cutting force. It modifies the feed rate on-line to keep the surface roughness constant and to make machining more efficient. The control model was developed based on simplified models of the turning process and the feed drive servo-system. The experiments were performed to find the correlation between surface roughness and cutting forces in turning and to provide functional correlation with the controllable factors. Simulation setup and results are presented to demonstrate the efficiency of the proposed control model. In terms of surface roughness fluctuations and cutting efficiency, the suggested control model is much better than a conventional CNC controller alone. Integrating the developed control model with the CNC machine controller significantly improves the quality of machined components.
Keywords: machining, turning, surface roughness, model based control, simulation

Highlights
- *A surface roughness control simulation of turning is accomplished.*
- *A transfer function that describes the controlled plant model is carried out.*
- *A correlation is found between surface roughness and the cutting force.*
- *Simulation results confirm the efficiency of the control simulation model.*
- *The system is insensitive to disturbances due to tool wear and variations of cutting depth.*
- *Maintaining constant cutting force leads to a better (constant) quality of surface.*

0 INTRODUCTION

The machining quality on computerized numerically controlled (CNC) machine tools is sensitive to the machining parameters. With modern machine tools, an operator still manually adjusts controlling parameters, such as feed rate and cutting speed. The adjusted values mainly depend on operator experience and knowledge. Standard machining catalogues and commercial cutting condition prediction software [1] generally offer only recommended values, which are far from optimum. Usually, technicians set the highest feed rate possible. The limitations are the available machine power, tool strength and surface roughness tolerance. The increase of the cutting force due to the higher feed rates increase the tool and work piece deflection, machine chatter; consequently, work piece precision is reduced. Therefore, maintaining the cutting force on the tool tip at the appropriate value is a method to ensure dimensional accuracy. To solve this problem, it is necessary to modify the controlling parameters on-line [2]. Adaptive control (AC) accomplishes this. The AC of turning operations is a logical continuance of the evolution of CNC systems. The goal of adaptive control is to control the turning process via the on-line adjusting of controlling parameters [3], which are subject to machining constraints. An AC system is introduced in the cutting process by Stute and Goetz [4].

Such systems to maximize the feed rate for a specified cutting force in turning operations have been proposed in the past [5]. Many AC systems that employed on-line adjustment of the feed rate to ensure a stable and efficient turning have been proposed [6] and [7]. Thus far, no control system has been proposed to adjust cutting condition to maintain surface roughness constant in prescribed tolerances.

Model reference adaptive control (MRAC) systems have been also developed for turning [8]. MRAC systems, developed from AC theory, are widely used due to their robustness and disturbance rejection capability. The basic adaptive model reference adaptive controller approach was originally investigated by Landers and Ulsoy [9]. These controllers were simulated and evaluated and physically implemented by [10]. Numerous forms of MRAC system have been developed, especially in milling [11] and [12]. Non-deterministic MRAC controllers are not always suitable for real time control [13] because the controller requires an explicit model and significant computation. The neural network-based MRAC systems [14] and [15] allow much faster development of the models and thus make these controllers practical. The main drawback of integrating MRAC systems in turning is that many algorithms generate significant oscillatory behaviour at low depths of cutting [10]. The model-based control system developed in our research overcomes this

*Corr. Author's Address: University of Maribor, Faculty of Mechanical Engineering, Smetanova 17, 2000 Maribor, Slovenia, uros.zuperl@um.si

problem by employing off-line numerical simulations. Via simulations, the performance and stability of the control system are determined. The optimum control parameters for turning have been investigated. Via simulations, we also attempted to determine if the proposed control model has been justified for all test conditions. The proposed control model is conceived in such a way that there is no need to perform complicated modelling since the simulations depend only on easily measurable cutting force signals.

Recent studies show that force signals contained the most useful information for determining the output process variables, especially surface roughness [16].

However, in many cases, the use of force sensors is not practical for retrofit applications and the spindle power signal is often used as an alternative. By analysing the cutting force characteristics, it is possible to assess the changes in the quality of surface finish [17]. Therefore, the experiments were performed to find the correlation between surface roughness and the resultant cutting force. Correlations found for various machining conditions are incorporated into simulation models.

The resulting control model maintains an almost constant surface roughness throughout the cutting process regardless of the work piece material used, cutting tool and machining parameters, especially depth of cutting.

In this paper, an AC system is described for turning on a lathe with a constant cutting force constraint. The detailed structure of an adaptive surface control system for turning is presented. The model based controller modifies the feed rate on-line in order to keep the surface roughness constant and to maintain the cutting efficiency. Due to the very encouraging simulation results, the control model has been implemented successfully on a commercial lathe. The experimental results from an actual machining operation will be presented in the future work.

1 STRUCTURE OF ADAPTIVE CONTROL SYSTEM

The idea of this research is to implement on-line AC in conjunction with an off-line cutting condition prediction algorithm.

A model-based control system is a controller that modifies its behaviour in response to change in the dynamics of the process.

The structure of the proposed control system of turning is presented in Fig. 1. The system consists of a cutting conditions prediction model, a reference, a comparison block and control block, a cutting process, a CNC servo system, a feed rate override command element and a sensor that measures the output process variable.

The defined constraints of all output process variables are fed into the comparison block. Then they are compared with current feed values and send to the control block. The control block algorithm adapts cutting parameters in such a way that it improves the cutting tool life and surface roughness.

The objective of the proposed control is, therefore, to adjust the feed rate in order to maintain the turning resultant cutting force and surface roughness as constant. If the resultant cutting force is maintained as constant during the process of turning, then the surface finish also remains stable. In order to control the process, force information must be available to the control algorithm at every 10 ms. LabVIEW data acquisition software is used to

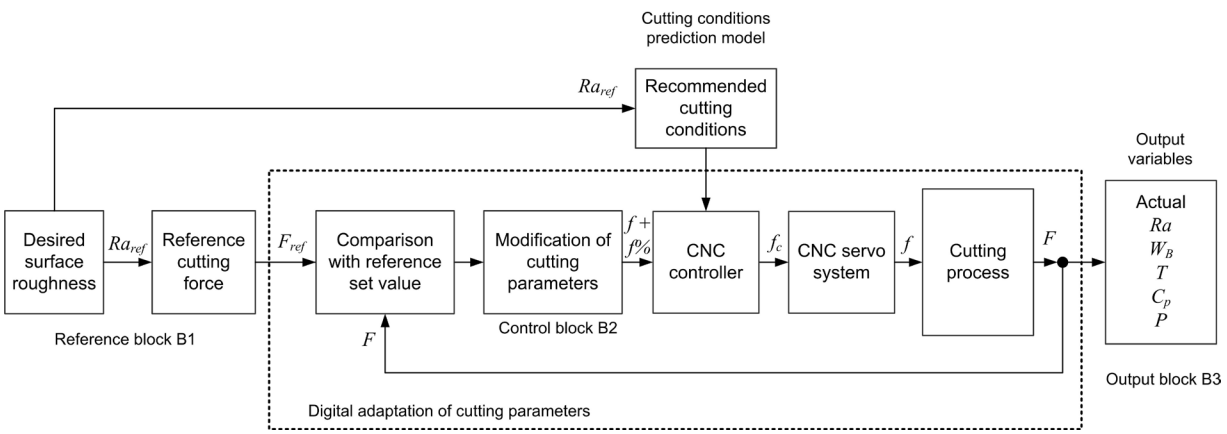

Fig. 1. *Structure of surface roughness control in turning*

provide this information. The cutting force resultant is obtained using a Kistler force dynamometer. These measured cutting force signals are used in the control model to regulate the surface roughness.

The command feed rate calculated from the control model algorithm is converted to a percentage of the programmed feed rate. The control model adjusts the feed rate by assigning an override percentage to the CNC controller of the turning machine, based on a measured cutting force. The actual feed rate is the product of the feed rate override percentage f% and the recommended feed rate f.

The output block determines output process variables (W_B tool wear [18], T tool life, C_P operation cost, F resultant cutting force).

A simulation block diagram for testing the stability and fine tuning of the control parameters is developed. After simulations, the control model can be installed on real CNC turning machine tool.

1.1 Sequence of Steps for Adaptive Control of Turning Process

The sequence of steps for surface roughness control of the turning process is presented below.

1. The desired value Ra_{ref} is initiated;
2. Based on desired Ra_{ref}, the recommended cutting conditions are determined off-line by an artificial neural network model [19];
3. Based on desired Ra_{ref}, the reference force F_{ref} is predicted according to the reference block B1;
4. When the force F_{ref} is known, the command value f_c is determined;
5. The other recommended cutting conditions are sent to the CNC of the machine tool;
6. The measured resultant cutting forces are compared with reference value and sent to the control (block for modification of cutting parameters);
7. Actual Ra is determined based on the measured cutting force F;
8. The control block adjusts the feed rates and sends it back to the machine;
9. Steps 6 to 9 are repeated until termination of machining.

The algorithm of the proposed control structure is presented in Fig. 2.

The objective of control algorithm is to adjust the turning process parameters to achieve the required values of surface finish.

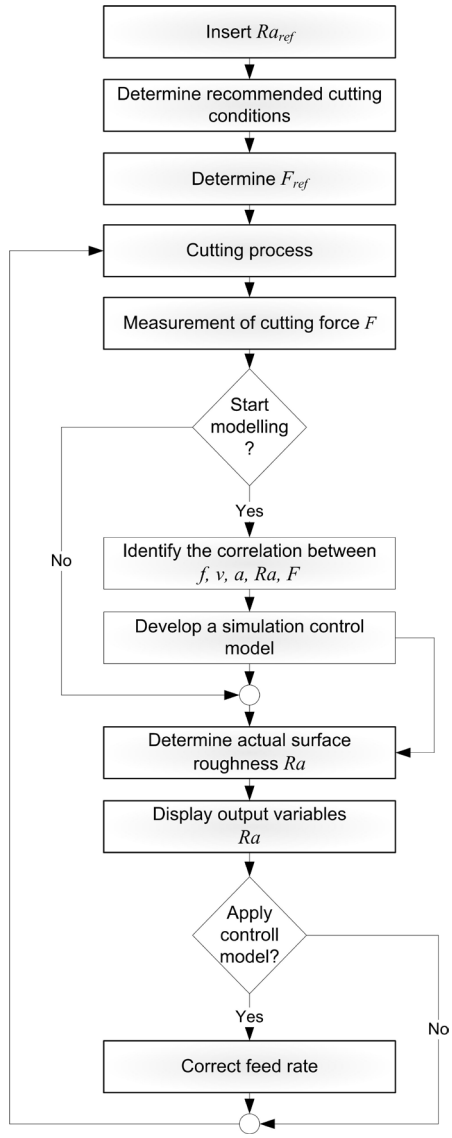

Fig. 2. *Flow chart of adaptive surface roughness control*

2 CONTROL MODEL SIMULATION BLOCK DIAGRAM

The block diagram of the proposed control model is presented in Fig. 3. It enables a closed loop control of cutting force and thus produces a desired surface roughness in turning.

The simulator input is the desired surface roughness, and the output is the actual surface quality.

The control model is developed in Matlab Simulink. It comprises of simulator of cutting, a simulator of the feed servo-drive, a reference block, an output variables block, a block for modification of cutting parameters and the models determining the mutual relations between influencing cutting

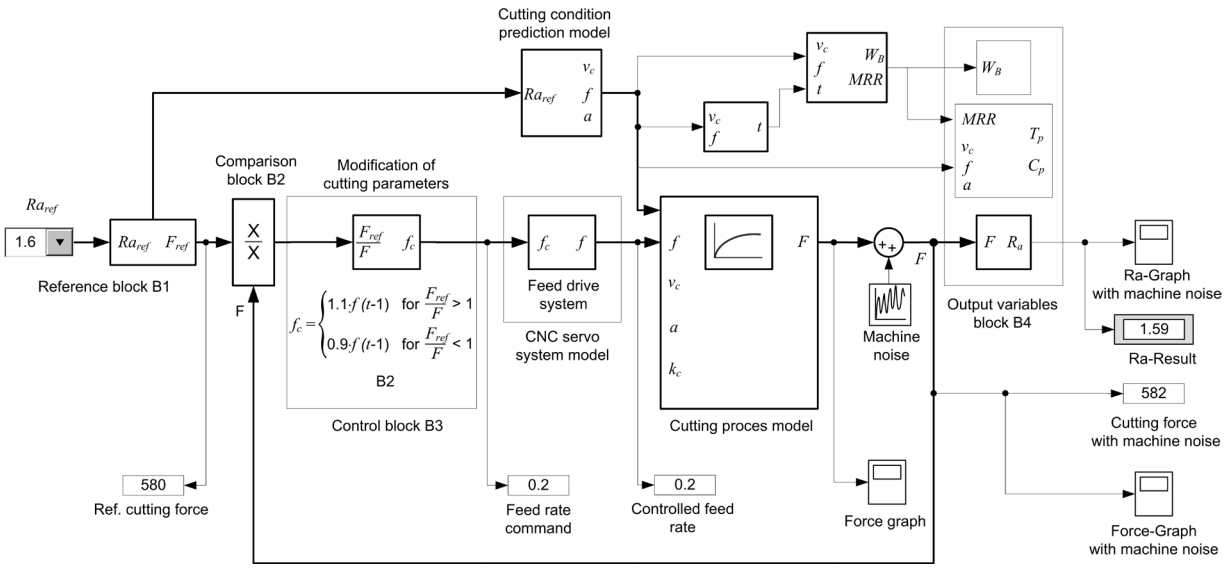

Fig. 3. *Simulation block diagram for the surface roughness control model*

quantities. These elements describe the dynamics of the control model.

The objective of the block for the modification of cutting parameters is to minimize control errors and to provide the appropriate feed rate for a specific machining situation.

Digital adjustment of feed rate is accomplished in such a way that the output process variable is first compared with the reference value. If the value of actual *Ra* exceeds the desired surface roughness Ra_{ref}, then the control algorithm immediately reduces the feed rate in order to reduce the produced surface roughness, while the cutting speed remains constant.

If the value of actual *Ra* does not reach the desired surface roughness, then the control algorithm immediately increases the feed rate. The plant to be controlled includes the cutting process and the CNC servo system.

The machine tool used in the study was a typical CNC lathe controlled by a CNC whose model allows feed rate override commands ranging from 0 % to 150%.

The cutting process and the CNC servo system model can be represented as:

$$H_p(s) = \frac{F(s)}{f(s)} = \frac{k_c \cdot a}{n} \cdot \frac{1}{1 + t_c \cdot s}, \quad (1)$$

$$H_s(s) = \frac{f(s)}{f_c(s)} = \frac{1}{1 + t_s \cdot s}, \quad (2)$$

where n is the spindle speed in [rpm], k_c is the specific cutting force [N/mm²], a is the depth of cut, t_c is the time constant of the cutting process, and t_s is the time constant of the CNC servo system.

The feed servo-drive model simulates the machine response to changes in the desired feed rate. The objective of the feed servo-drive system is to minimize the error and provide the appropriate and actual feed rate for a specific machining situation.

The step response of the CNC system used in our research is shown in Fig. 4. The pre-programmed feed rate (0.2) is overridden from 0 % to 150 %. The time to reach 0.632 of the step input is found graphically. The time constant t_s is measured to be 0.13 s.

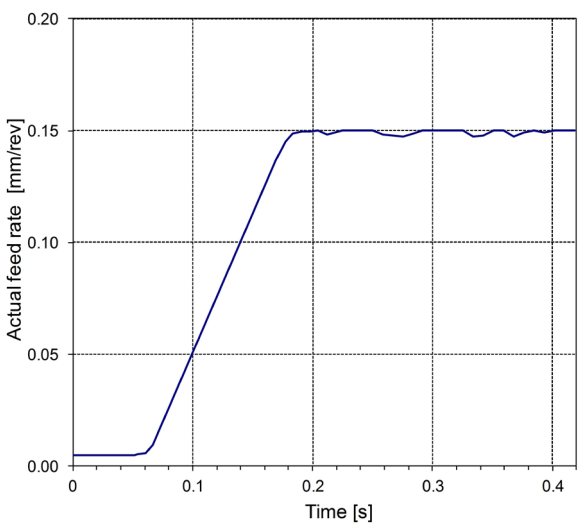

Fig. 4. *Step response of the x-axis feed drive system*

The whole turning plant system can be represented with the transfer function:

$$H(s) = \frac{1}{n} \cdot \frac{k_c \cdot a}{1 + (0.13 + t_c) \cdot s + 0.13 \cdot t_c \cdot s^2}. \quad (3)$$

The uncontrollable measurement noise is not included in the above transfer function due to the difficulties of describing its random nature mathematically.

The transfer functions of the machine dynamics are based on the technical specifications of the GF NDM 16 CNC lathe.

The predicting models of the output variables developed in this work are based on experimental results performed in research **[20]**.

The experimental datum contains the value of the predicted (modelled) quantity and the relevant influencing parameters (cutting parameters). Statistical and mathematical modelling is used to provide functional relationships with the most important parameters and variables, i.e. feed rate, spindle speed, surface roughness and the resultant cutting force.

The results of modelling are the simulation models, which can be easily included into the Simulink simulation package. These models are depicted in Fig. 3.

Prior machining the required quality of the surface finish Ra_{ref} is defined. The model defining the correlation between the desired surface roughness and the appurtenant resultant cutting force is labelled as M1.

In order to develop the M1 model, the experiments were carried out for all combinations of the chosen parameters that significantly affect the turning process. These input parameters are cutting conditions, depth of cut, feed rate, and cutting speed. Other parameters, such as cutting tool geometry, type of raw material, etc., are kept constant for the scope of this study. A total of 1500 combinations of input parameters (depth of cut, feedrate, and spindle speed) were selected to measure cutting forces and the corresponding roughness of the machined surface.

The measurements of the tool wear during machining were not carried out, despite the fact that it has a significant effect on the rise of cutting force and on the achieved surface roughness. The aim of this study is to take into account the tool condition in the prediction of cutting forces without expensive in-process tool wear measurements.

Recent studies show that cutting force signals and the surface roughness values contain the most useful information for determining the tool condition (tool wear) **[5]**. Therefore, the influence of the tool wear in the prediction of cutting forces is captured indirectly through increased surface roughness due to changes of the cutting edge geometry.

Based on the values of these 1500 experimental data, the relation between the cutting force and the surface roughness was determined according to Eq. (4). This equation was obtained by using single regression formula for steel machining at low depths of cut.

$$F_{ref} = -279.26 \cdot Ra_{ref}^{\ 5} + 2946.9 \cdot Ra_{ref}^{\ 4} - 12032 \cdot Ra_{ref}^{\ 3} + 23636 \cdot Ra_{ref}^{\ 2} - 22062 \cdot Ra_{ref} + 8250.8. \quad (4)$$

Eq. (4) determines the reference cutting force necessary to reach and maintain the desired surface roughness regardless of the cutting tool condition. It indirectly takes into account the condition of the tool in the calculation of cutting forces.

The output variables block (B4) tests if the simulated *Ra* corresponds with the desired *Ra*. The produced surface roughness was calculated from the above mentioned experimental data according to Eq. (5):

$$Ra = 0.2401 \cdot e^{0.0034 \cdot F}. \quad (5)$$

Similar to Eq. (4), Eq. (5) is obtained by using an exponential regression formula. Both equations are based on the same experimental data.

The outputs of block B4 were also compared to the predictions of the artificial neural network surface roughness model developed by **[21]**. The predictive capability of the block B4 and neural network approach is compared using statistics, which showed that neural network predictions for surface roughness were only 2 % closer to the experimental measurements, in comparison to block B4.

A much simpler and faster B4 is used in the simulation model, despite the lower accuracy of predictions.

When the simulation model of the feed drive system (shown in Fig. 3) and the simulator of cutting process are replaced by the real machine tool, a harmonized system for dynamic adjustment of feed rate is obtained.

The system with an adjustment of feed rate override assures the required surface roughness. The following algorithm is used to on-line adjust the feed rate.

$$f_c = \begin{Bmatrix} 1.1 \cdot f(t-1) & for \ \dfrac{F_{ref}}{F} > 1 \\ 0.9 \cdot f(t-1) & for \ \dfrac{F_{ref}}{F} < 1 \end{Bmatrix}, \quad (6)$$

where, f_c is a feed rate command [mm/rev], and $f(t\text{-}1)$ previous actual feed rate command.

This algorithm determines the optimal feed rate required to obtain the controllable surface roughness.

3 SIMULATION RESULTS AND DISCUSSION

Via simulations, the efficiency and stability of the control model with different requirements of the surface quality are tested. The criterion for the efficiency of the control model is the difference between the desired and simulated *Ra*.

The starting cutting conditions and the desired Ra_{ref} are the input data.

The following paragraphs present the simulation example (Sim. No. 1 and Sim. No. 3; Table 1) in which the model-based control was applied to demonstrate its performance. The simulation outputs are shown in Fig. 5.

Recommended cutting conditions for each cut are first determined off-line, and then simulation tests are made without and with control model action. The recommended cutting parameters are determined with the prediction model [19]. The spindle speed is set at 610 rpm, and the resultant cutting force undergoes random changes up to 10 %. The simulation time is

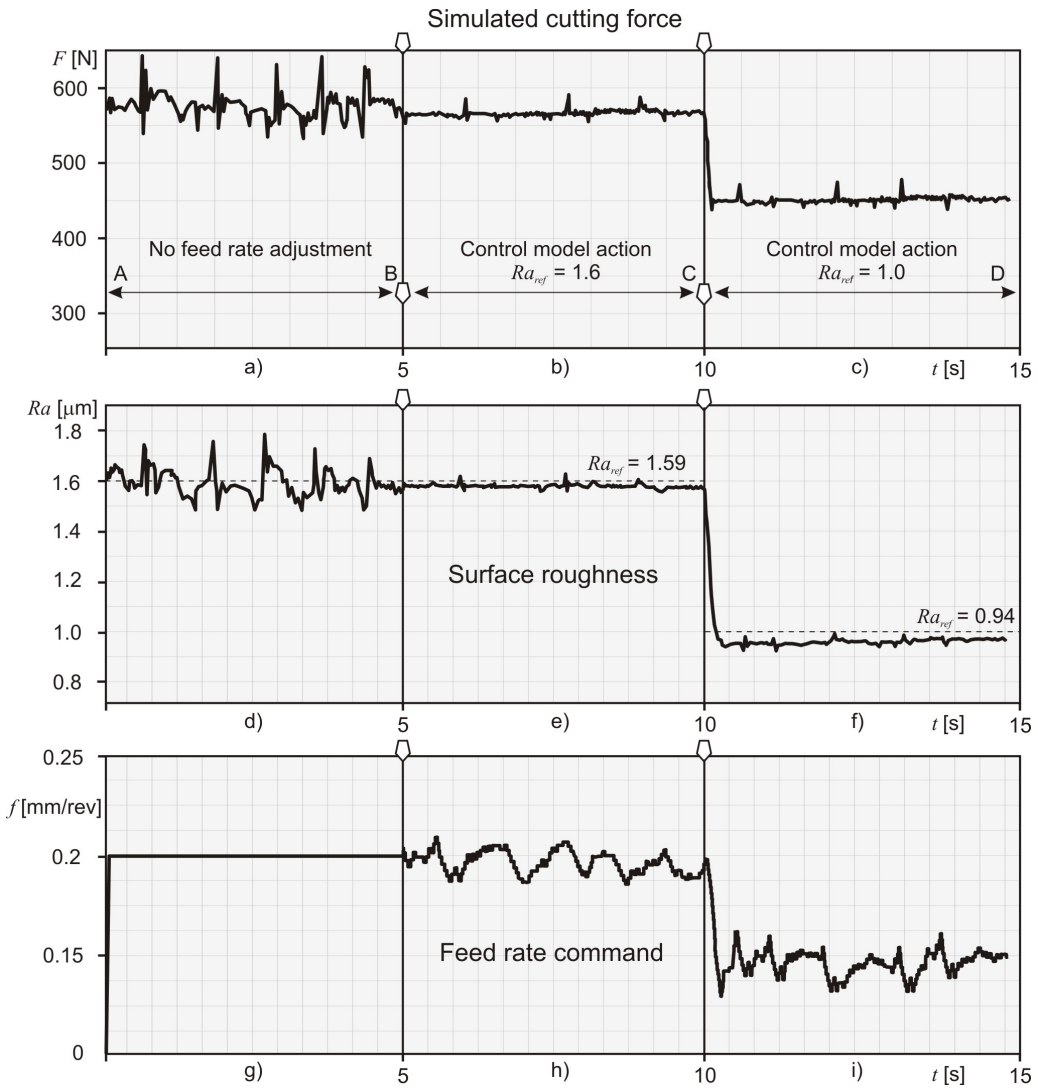

Fig. 5. *Simulated control model response with in without feed rate adjustment*

Table 1. *The simulation requirements and result*

Sim. No.	Desired surface roughness Ra_{ref} [mm]	Results without control model action		Results with control model action		
		F [N]	f [mm/rev]	F[N]	f [mm/rev]	Actual surface roughness Ra [mm]
1	**1.0**	**460.63**	**0.17**	**448.06**	**0.15**	**0.95**
2	1.3	465.54	0.18	522.86	0.17	1.28
3	**1.6**	**556.23**	**0.2**	**582.12**	**0.2**	**1.59**
4	1.9	628.78	0.23	615.5	0.22	1.87
5	2.2	641.5	0.24	638.28	0.23	2.1
6	2.5	661.83	0.25	683.73	0.25	2.45
7	2.8	735.77	0.28	727.0	0.27	2.77
8	3.1	762.35	0.29	750.0	0.28	2.98

15 s. In Table 1, the requirements and the results of simulations are indicated.

The undesirable aspects of the experimental results of the measured cutting forces were represented by the model of machine noise, which is shown on Fig. 3. This model has been generated to simulate the uncontrollable measurement noise resulting especially from the non-homogeneity of raw material, tool wear and tool breakage. The machine noise model is generated by using a random of variation, which relates to the settings of cutting force data acquisition software. It adds noise in the simulation model in order to test the reference of the output with the effect of the noise. When the noise is eliminated from the model, an ideal simulation result was obtained.

The signals of resultant cutting force and the quality of surface are mutually related and have identical trends.

Fig. 5d and e show the surface roughness of the workpiece without and with control model action. The *Ra* in Fig. 5d is not constant when machining without control action, because the feed rate is not adjusted when the output exceeds the reference value.

Fig. 5d is the response of the surface roughness where there is no feed rate adjustment. The *Ra* is constant when using dynamic adjusting of feed rates (Fig. 5d; Section B to D).

The control model is initiated by the selection of the reference value Ra_{ref}; afterwards, reference cutting force F_{ref} is predicted according to reference block B1. To use the proposed control system and to adjust the feed rate, the desired surface roughness is 1.6 mm, the recommended feed is 0.2 mm/rev and its allowable adjusting rate is [0 % to 150 %].

The data of simulation example is marked as No. 3 and is presented in Table 1. The depth of cutting was set to 1 mm. When the reference force is known, the command value f_c is determined according to the B3 block. The initial value f_c is 0.2 mm/rev, thus allowing the feed to be overridden from 0 mm/rev to 0.3 mm/rev.

The control bock is changing the initial value f_c, until the optimum controlled feed rate of 0.2 mm/rev has been reached. The CNC servo drive model generates the actual feed rate f from the command signal f_c. Dynamic adjustment of feeding is a prerequisite for maintaining constant surface roughness of 1.6 mm.

The actual *Ra* is determined by the output variables block B4. The result is a roughness of 1.59 mm, which is acceptable if compared with the desired value of 1.6 mm (Fig. 5e).

In the first simulation using constant feed rates the *Ra* reaches its proper value only in the last second of Sections A and B (Fig. 5d). However, by applying control action, the average *Ra* achieved is much more close to the reference *Ra*. It reaches and maintains the value of 1.59 mm (Fig. 5e).

The resultant cutting force for the control model is maintained at about 570 N (Fig. 5b).

The control system responds to the fall of the desired *Ra* by immediate reduction of feeding (Fig. 5f; Section C to D). As a result, the cutting force drops to value of 448 N (Fig. 5c). It can be seen that by continuously adjusting the feed rate (section B to D), the cutting force is maintained at a constant so that the desired surface roughness can be attained.

The results confirm that the proposed control model is efficient in obtaining the desired surface roughness and that it is efficient in fine machining. Constant cutting forces lead to better surface quality.

Although the system remains stable in all performed simulation tests, one obvious problem appears if the measured resultant cutting force approaches zero. In this situation, the feed rate command values would increase to infinity. A very

small value of cutting force would lead to incorrect increase in the feed rate, causing excessive forces when the tool enters the workpiece.

This problem has been efficiently eliminated by restricting the controller action to sample periods when the measured forces are above a certain user-specified threshold for a specified time. In our study, the threshold to start the control action is set to be 100 N.

This solution ensures that the control algorithm is activated only when the tool is engaged in the workpiece. When the forces are bellow a user-defined threshold, the tool is assumed to be out of the work piece, and the control actions are paused. The developed solution also includes the restrictions of the control actions for feedrates limited by chip thickness.

After simulations, the simulation model of CNC servo system (shown in Fig. 5) and the simulator of cutting process were replaced by the real CNC machine tool GF NDM 16. The performance of the suggested system was then verified by a serial of experimental works on the lathe for Ck 45 steel workpieces with variation of cutting conditions. The machine tool was connected with a personal computer. The connection was designed to allow GF NDM16 to be under digital control implemented in the PC. The model control was developed in Matlab. The experimental testing results are not described in this paper.

4 CONCLUSION

In this research, the model-based controller is proposed to control the turning process with constant surface roughness. The control model modifies the feed rate in real time in order to keep the surface roughness constant and to make machining more efficient.

The surface roughness control model was developed based on the simplified models of the feed drive servo system and the turning process.

The correlation between the process output variables (cutting forces, surface roughness) and cutting parameters is determined by using statistics. A high degree of correlation is found between surface roughness and the resultant cutting forces for various machining conditions.

The effects of the developed control model on *Ra* control have been studied through simulations. They have shown that the proposed control model makes the system insensitive to disturbances due to tool wear, non-homogeneity of work piece material and variations of depth of cutting.

The performance of the developed control model is much better in comparison to classic CNC turning in the aspects of surface roughness fluctuation.

The control system was also realized experimentally due to the excellent results of the simulations.

5 REFERENCES

[1] Çolak, O. (2014). Optimization of machining performance in high-pressure assisted turning of Ti6Al4V alloy. *Strojniški vestnik – Journal of Mechanical Engineering*, vol. 60, no. 10, p. 675-681, **DOI:10.5545/sv-jme.2013.1079**.

[2] Grigoriev, S.N., Starkov, V.K., Gorin, N.A., Krajnik, P., Kopač, J. (2014). Creep-feed grinding: an overview of kinematics, parameters and effects on process efficiency. *Strojniški vestnik – Journal of Mechanical Engineering*, vol. 60, no. 4, p. 213-220, **DOI:10.5545/sv-jme.2013.1547**.

[3] Koren, Y. (1983). *Computer Control of Manufacturing Systems*. McGraw-Hill, New York.

[4] Stute, G., Goetz, F.R. (1995). Adaptive control system for variable gain in ACC systems. *Proceedings of the 16th International Machine Tool Design and Research Conference*, Manchester, p. 117-121.

[5] Pitstra, W.C., Pieper, J.K. (2000). Controller designs for constant cutting force turning machine control. *ISA Transactions*, vol. 39, no. 2, p. 191-203, **DOI:10.1016/S0019-0578(00)00008-2**.

[6] Hwang, C.L. (1993). Adaptive turning force control with optimal robustness and constrained feed rate. *International Journal of Machine Tools and Manufacture*, vol. 33, no. 3, p. 483-493, **DOI:10.1016/0890-6955(93)90054-X**.

[7] Ruey, J.L. (2012). Intelligent control of a constant turning force system with fixed metal removal rate. *Applied Soft Computing*, vol. 12, no. 9, p. 3099-3111, **DOI:10.1016/j.asoc.2012.05.012**.

[8] Daeshmend, L.K., Pak, H.A. (1986). Model reference adaptive control of feed force in turning. *ASME Journal of Dynamic Systems, Measurement and Control*, vol. 108, no. 3, p. 215-222, **DOI:10.1115/1.3143770**.

[9] Landers, R.G., Ulsoy, G.A. (1998). Supervisory machining control: design approach and experiments. *CIRP Annals - Manufacturing Technology*, vol. 47, no. 1, p. 301-306, **DOI:10.1016/S0007-8506(07)62838-8**.

[10] Landers, R.G., Ulsoy, A.G., Ma, Y.-H. (2004). A comparison of model-based machining force control approaches. *International Journal of Machine Tools and Manufacture*, vol. 44, no.7-8, p. 733-748, **DOI:10.1016/j.ijmachtools.2004.02.005**.

[11] Tomizuka, M., Oh, J.H., Dornfeld, D.A. (1983). Model reference adaptive control of the milling process. *ASME Control of Manufacturing Processors and Robotic Systems*, vol. 11, p. 55-64.

[12] Lauderbaugh, L.K., Ulsoy A.G. (1989) Model reference adaptive force control in milling. *ASME Journal of Engineering for Industry*, vol. 111, no. 1, p. 13-21, **DOI:10.1115/1.3188726**.

[13] Yamazaki, K., Kojima, N., Sakamoto, C., Saito, T. (1991). Real-time model reference adaptive control of 3-D sculptured surface machining. *CIRP Annals - Manufacturing*

Technology, vol. 40, no. 1, p. 479-482, **DOI:10.1016/S0007-8506(07)62034-4**.

[14] Psaltis, D, Sideris, A, Yamamura, A.A. (1988). A multilayered neural network control. *IEEE Control Systems Magazine*, vol. 8, no.2, p.17-21, **DOI:10.1109/37.1868**.

[15] Tarng, Y.S., Hwang, S.T., Wang, Y.S., (1994). A neural network controller for constant turning force. *International Journal of Machine Tools and Manufacture*, vol. 34, no. 4, p. 453-460, **DOI:10.1016/0890-6955(94)90077-9**.

[16] Zuperl, U., Cus, F. (2004). Tool cutting force modeling in ball-end milling using multilevel perceptron. *International Journal of Materials Processing Technology*, vol. 153-154, p. 268-275, **DOI:10.1016/j.jmatprotec.2004.04.309**.

[17] Korkut, I., Donertas, M.A. (2007). The influence of feed rate and cutting speed on the cutting forces, surface roughness and tool–chip contact length during face milling. *Materials & Design*, vol. 28, no. 1, p. 308-312, **DOI:10.1016/j.matdes.2005.06.002**.

[18] Brezak, D., Majetić, D., Udiljak, T., Kasać, J. (2014). Tool wear estimation using an analytic fuzzy classifier and support vector machines. *Journal of Intelligent Manufacturing*, vol. 23, no. 3, p. 797-809, **DOI:10.1007/s10845-010-0436-x**.

[19] Cus, F., Zuperl, U. (2006). Approach to optimization of cutting conditions by using artificial neural networks. *Journal of Materials Processing Technology*, vol. 173, no. 3, p. 281-290, **DOI:10.1016/j.jmatprotec.2005.04.123**.

[20] Zuperl, U., Cus, F. (2003). Optimization of cutting conditions during cutting by using neural networks. *Robotics and Computer-Integrated Manufacturing*, vol. 19, no. 1-2, p. 189-199, **DOI:10.1016/S0736-5845(02)00079-0**.

[21] Asiltürk, I., Çunkaş, M. (2011). Modeling and prediction of surface roughness in turning operations using artificial neural network and multiple regression method. *Expert Systems with Applications*, vol. 38, no. 5, p. 5826-5832, **DOI:10.1016/j.eswa.2010.11.041**.

Strojniški vestnik - Journal of Mechanical Engineering 61(2015)4, 254-264

DOI:10.5545/sv-jme.2014.2185
Original Scientific Paper
Received for review: 2014-09-19
Received revised form: 2015-03-03
Accepted for publication: 2015-03-11

BEM-Based Algorithm for URANS Simulations of Flow over a Square Cylinder

Janez Lupše* – Leopold Škerget – Jure Ravnik
University of Maribor, Faculty of Mechanical Engineering, Slovenia

The boundary element method (BEM) is extended for the discretisation of the incompressible Navier-Stokes equations in the velocity-vorticity form for the URANS formulation. BEM uses fundamental solutions as weighting functions, thus the approach enables inclusions of some of the governing physics in the method itself. For testing purposes the flow around the square cylinder in the two-dimensional channel with a blockage ratio of 1/8 was chosen as the appropriate test case. The flow was calculated for the Reynolds numbers ranging from 100 to 1000. At Reynolds number 1000, the governing equations were solved directly in a quasi DNS manner and in the RANS form using the Spalart-Allmaras turbulence model within an URANS simulation.

Keywords: boundary element method, velocity-vorticity form, incompressible flow, URANS, square cylinder

Highlights

- *Extension of the boundary element based algorithm is proposed for simulation of turbulent flows.*
- *Velocity vorticty formulation of Navier - Stokes equations is employed.*
- *Simulation of flow over a square cylinder inside a channel at blockage of 1/8.*
- *Simulations were performed within the unsteady laminar regime of the flow and within the low turbulent regime of the flow.*
- *Comparison between the unsteady RANS model and the quasi-DNS simulation.*

0 INTRODUCTION

The boundary element method has been seen as a very successful method for solving various problems. In general, this method has an advantage over other numerical methods when the fundamental solution to the governing equations exists, thus effectively reducing the dimension of the problem [1]. Using the description of the governing physics regarding the fundamental solution, a stable and highly accurate numerical scheme is obtained, even on coarse numerical meshes. Unlike most of the other discretisation methods, using fundamental solutions this method relies on capturing the governing physics instead of the brute force. Furthermore, the derivatives of the transported variables, normal to the boundary of the domain or sub-domain, are a part of the solution of the system. This enables accurate representation of these values and the corresponding integral parameters such as the Nusselt number for example. Unfortunately, the governing equations for the fluid flow in general are of convective-diffusive type with important and non-trivial source terms. Even when the convective-diffusive fundamental solution is used, discretisation of the whole solution domain is needed. In addition, when a fundamental solution that includes more of the governing physics of the flow is used (with the exception of the Laplace fundamental solution), the integrals that arise from the discretisation of the governing equations need to be re-evaluated every time the corresponding field of variables (e.g., velocity) is changed. However, the inclusion of the flow physics into the discretisation usually leads to coarser numerical meshes.

Whilst there are various approaches for the discretisation of domain terms (dual reciprocity method [2], the green element method [3], etc.) arising regarding the discretisations of the Navier-Stokes equations the so-called boundary-domain integral method (BDIM) [4] is used in our case. This approach gives discretisation of the solution domain similar to the finite element method, with each cell representing a separate sub-domain. The appropriate compatibility and equilibrium conditions have to be applied in order to interconnect the sub-domains. This results in an over-determined linear system of equations with a non-symmetric sparse system matrix that is solved by the LSQR solver [5] using diagonal-preconditioning.

In Lupše et al. [6] the method was extended for solving the Reynolds averaged Navier-Stokes equations (RANS). This article is aimed at testing the developed algorithm for the intrinsically unsteady flows that can also be described using the unsteady RANS (URANS) approach. In regard to this purpose the flow over a square cylinder inside a channel was chosen as a relevant test case.

The confined flow around the square cylinder is a challenging test for numerical methods as a multitude of interesting flow phenomena are present within relatively simple geometry. This type of flow

*Corr. Author's Address: University of Maribor, Faculty of Mechanical Engineering, Smetanova 17, 2000 Maribor, Slovenia, janez.lupse@yahoo.ca

is important during many engineering applications ranging from the cooling of electronics to building aerodynamics. Although free-flow around the circular cylinders has been the focus of extensive research [7], less effort has been put into researching the confined flow around bluff bodies, especially around the square cylinders. Additional parameters need to be defined for the confined flow, namely those inflow velocity profiles and blockage ratios of the channel that do not appear in free-flow cases. Davis et al. [8] performed experiments and numerical simulations of the flows for two different blockage ratios (B = 1/4 and B = 1/6) and a wide variety of Reynolds numbers ranging from 100 and up to 1800. Later, [9] performed numerical simulations for blockage ratio of 1/8 and Reynolds numbers of the flow up to 900. A common argument about simulations of [9] is that the meshes used were too coarse around the vicinity of the cylindrical obstacle, hence the discrepancies of the obtained results with other authors. Breuer et al. [10] tested two different numerical methods on this type of flow at the blockage ratio of 1/8 for Reynolds numbers up to 300. Their results are widely considered as the benchmark for the laminar part of the flow.

The results of [10] were later confirmed by the so-called multi-particle collision dynamics method tested at Reynolds numbers lower than 130 [11]. Galletti et al. [12] performed a test of a proper orthogonal decomposition-based model on the confined flow over a square cylinder and obtained comparable results to [10] having a blockage ratio of 1/8. Later the flow was also simulated for various laminar Reynolds numbers and extended those simulations to different blockage ratios and non-isothermal flows [13] and [14].

The flow chosen for the test case featured many interesting phenomena at different flow regimes. At the Reynolds number equal to 1 creeping flow is observed. The flow separates from the trailing edge of the cylinder with any increase in the Reynolds number. Although two recirculation bubbles are present and increase in length as the Reynolds number of the flow increases, the flow is steady up to a critical point. Authors in literature have reported different values for this critical number but agree that it lies somewhere between Re = 54 [15] and Re = 70 [16]. After this point the flow becomes unsteady but periodic. Separation occurs at the trailing edge at first and with increasing Reynolds number of the flow moves to the leading edge of the cylinder. Flow separation causes a distinct pattern of flow, known as the Von Karman vortex street. Spatial effects occur at about the Reynolds number 300 [10]. As the Reynolds number of the flow is defined by the cylinder diameter and not the channel width it is necessary to have in mind that with a used blockage ratio of 1/8 at about this Reynolds number, transition to turbulence in the channel flow is slowly starting to occur. Thus in reality, the flow beyond the Reynolds number 300 is be-coming increasingly turbulent. Consequentially, for the inlet profile the turbulent velocity profile would be more appropriate passed these Reynolds numbers of the flow. The data available in literature for the Reynolds numbers up to 1000 [8] is obtained by imposing the standard parabolic velocity profile. As such, the parabolic velocity profile in this work, used at the inlet boundary condition, was used purely for the testing purposes of the developed numerical algorithm and code in order to enable easier and more accurate comparison with the available data of [9].

1 GOVERNING EQUATIONS

Whilst the more common approach to describing the fluid flow is the use of the Navier-Stokes equations in their primitive forms, the velocity-vorticity formulation is used in our work. In this formulation the flow equations are split into kinematic and kinetic parts. In general, the approach gives us the advantage of eliminating the pressure gradient from the governing equations. However, the boundary conditions for the vorticity field in Eqs. (1) and (2) are generally unknown intuitively, unlike the velocity boundary condition in the momentum transport equation.

The flow kinetics is described by the vorticity transport equation obtained from the momentum transport equation by applying the curl operator [17]. For the incompressible planar flow the following equation is obtained:

$$\frac{\partial \omega}{\partial t} + U_j \frac{\partial \omega}{\partial x_j} = \nu_0 \frac{\partial^2 \omega}{\partial x_j \partial x_j} - \frac{1}{\rho_0} e_{ij} \frac{\partial \rho g_i}{\partial x_j}, \qquad (1)$$

where ω is used for the vorticity, U_j for the components of the velocity vector and x_j the spatial coordinates; ν_0 the kinematic viscosity, ρ_0 the fluid density and g_i the components of the gravity acceleration vector. The vorticity vector is treated as a scalar within the planar flow since only the component of the vorticity normal to the plane of the flow has a non-zero value. In the RANS form of Eq. (1), an additional source term is obtained on the right hand side and the RANS form of the vorticity transport equation is then [6]:

$$\frac{\partial \omega}{\partial t} + U_j \frac{\partial \omega}{\partial x_j} = \nu_0 \frac{\partial^2 \omega}{\partial x_j \partial x_j} - \frac{1}{\rho_0} e_{ij} \frac{\partial \rho g_i}{\partial x_j} - \frac{1}{\rho_0} \frac{\partial f_i^m}{\partial x_j}, \qquad (2)$$

where the additional source term f_i^m is defined by:

$$f_i^m = -e_{ij}\frac{\partial \nu_t \omega}{\partial x_j} + 2e_{ij}\frac{\partial \nu_t}{\partial x_j}\omega + 2\frac{\partial \nu_t}{\partial x_j}\frac{\partial U_i}{\partial x_j}. \quad (3)$$

The effective viscosity is now comprised of the molecular part ν_0 and the modelled part ν_t. The over-bar indicating the averaging process is omitted for the sake of brevity.

The kinematics part is formed by the Poisson equation that links the velocity and vorticity fields. It is derived at from the continuity equation and the vorticity definition [1]. For the planar flow the following form of the kinematics equation is obtained:

$$\frac{\partial^2 U_i}{\partial x_j \partial x_j} + e_{ij}\frac{\partial \omega}{\partial x_k} = 0. \quad (4)$$

There exist very efficient algorithms for solving the velocity-vorticity forms of the equations [18] but they are only applicable for special cases using simplified geometry. Care has to be taken however since Eq. (4) admits solutions in which neither solenoidality of the velocity field nor vorticity definition hold true [19]. In order to obtain a general solution, an additional equation has to be included [1]:

$$\frac{\partial U_i}{\partial n} + e_{ij} n_j \omega = -e_{ij}\frac{\partial U_j}{\partial t}, \quad (5)$$

where the normal and tangential derivatives in respect to domain boundary are defined as:

$$\frac{\partial U_i}{\partial n} = n_j \frac{\partial U_i}{\partial x_j}, \quad (6)$$

and n and t are the unit normal and unit tangent vectors.

Finally, in order to close the system of equations, the Spalart-Allmaras model [20] is used as a closure model. The main equation of this closure model without the trip term is:

$$\frac{D\tilde{\nu}}{Dt} = C_{b1}\left[1 - F_{t2}\right]\tilde{S}\tilde{\nu} + \frac{1}{\sigma}\frac{\partial}{\partial x_j}\left(\left(\nu_0 + \tilde{\nu}\right)\frac{\partial \tilde{\nu}}{\partial x_j}\right) + \\ + \frac{1}{\sigma}C_{b2}\left(\frac{\partial \tilde{\nu}}{\partial x_j}\right)^2 - \left[C_{w1}F_w - \frac{C_{b1}}{\kappa^2}F_{t2}\right]\left[\frac{\tilde{\nu}}{d_n}\right]^2. \quad (7)$$

Eq. (7) is the transport equation for the so-called modified turbulent viscosity from which modelled viscosity ν_t, as used in Eq. (2) is obtained by simple algebraic expression. For the details on the functions and constants of the used model see the original reference [20].

2 BOUNDARY-DOMAIN INTEGRAL EQUATIONS

Prior to discretisation using the boundary element method, the governing equations need to be rewritten in integral form. If we use Ω for the solution domain and Γ for its boundary, then the integral form of the kinematics Eq. (4) can be written as

$$c\left(\xi\right)U_i\left(\xi\right) + \int_\Gamma U_i \frac{\partial u^*}{\partial n}d\Gamma - \int_\Gamma \frac{\partial U_i}{\partial n}u^* d\Gamma = \\ e_{ij}\int_\Gamma \omega n_j u^* d\Gamma - e_{ij}\int_\Omega \omega \frac{\partial u^*}{\partial x_j}d\Omega, \quad (8)$$

where we use ξ for the location of the source point, c for the geometric coefficient and u^* to denote the Laplace fundamental solution.

$$u^* = \frac{1}{2\pi}\ln\frac{1}{r}. \quad (9)$$

In Eq. (9) r is used for the distance between the integration and source points. The detailed derivation of the integral form of Eq. (8) can be found in [21]. Eq. (8) is then used for calculation of the velocity field inside the solution domain. In order to calculate the boundary conditions for the vorticity transport equation in a general case Eq. (4) has to be combined with Eq. (5). A new integral form of the kinematics Eq. (4) is obtained;

$$c\left(\xi\right)U_i\left(\xi\right) + \int_\Gamma U_i \frac{\partial u^*}{\partial n}d\Gamma = \\ = e_{ij}\int_\Gamma U_j \frac{\partial u^*}{\partial t_d}d\Gamma - e_{ij}\int_\Omega \omega \frac{\partial u^*}{\partial x_j}d\Omega, \quad (10)$$

with the tangential derivative defined as in Eq. (6).

The vorticity transport equation is a non-stationary convective-diffusive equation with nonlinear source terms. As such, several fundamental solutions can be used as weighting functions. If the parabolic diffusion fundamental solution is used the following integral form of the vorticity transport equation is obtained [6];

$$c\left(\xi\right)\omega\left(\xi, t_k\right) + \int_\Gamma \omega \frac{\partial u^*}{\partial n}d\Gamma - \int_\Gamma \frac{\partial \omega}{\partial n}u^* d\Gamma = \\ = \frac{1}{\nu_0}\int_\Omega \omega_{k-1}u^*_{k-1}d\Omega -$$

$$-\frac{1}{\nu_0}\left(\int_\Gamma \omega U_j n_j u^* d\Gamma - \int_\Omega \omega U_j \frac{\partial u^*}{\partial x_j} d\Omega\right) -$$
$$-e_{ij}\frac{1}{\nu_0\rho_0}\left(\int_\Gamma \rho g_i n_j u^* d\Gamma - \int_\Omega \rho g_i \frac{\partial u^*}{\partial x_j} d\Omega\right) -$$
$$-e_{ij}\frac{1}{\nu_0}\left(\int_\Gamma f_i^m n_j u^* d\Gamma - \int_\Omega f_i^m \frac{\partial u^*}{\partial x_j} d\Omega\right). \quad (11)$$

The index k is used for denoting the current time step, thus t_k denotes the current time. Instead of the parabolic diffusion fundamental solution the convection-diffusion fundamental solution can also be used. The following form of the equation is obtained [6];

$$c(\xi)\omega(\xi,t_k) + \int_\Gamma \omega Q^* d\Gamma - \int_\Gamma \frac{\partial \omega}{\partial n} u^* d\Gamma =$$
$$= -\frac{1}{\nu_0}\int_\Omega (\beta_1\omega_{k-1} + \beta_2\omega_{k-2}) u^* d\Omega -$$
$$-\frac{1}{\nu_0}\int_\Gamma \omega(U_j - U_{j0}) n_j u^* d\Gamma -$$
$$-\frac{1}{\nu_0}\int_\Omega \omega(U_j - U_{j0})\frac{\partial u^*}{\partial x_j} d\Omega -$$
$$-e_{ij}\frac{1}{\nu_0\rho_0}\left(\int_\Gamma \rho g_i n_j u^* d\Gamma - \int_\Omega \rho g_i \frac{\partial u^*}{\partial x_j} d\Omega\right) -$$
$$-e_{ij}\frac{1}{\nu_0}\left(\int_\Gamma f_i^m n_j u^* d\Gamma - \int_\Omega f_i^m \frac{\partial u^*}{\partial x_j} d\Omega\right), \quad (12)$$

where we use $\beta_1 = -2/\Delta t$, $\beta_2 = -1/(2\Delta t)$ and $Q^* = \partial u^*/\partial n + (U_{j0}n_{j0}/\nu_0)u^*$, for the time discretisation. As the transport equation of the turbulence model used is of the same type as the vorticity transport equation, a similar integral equation is derived at:

$$\left[c(\xi)\tilde{\nu}(\xi,t_k)\right] + \int_\Gamma \tilde{\nu}\frac{\partial u^*}{\partial n} d\Gamma - \int_\Gamma \frac{\partial \tilde{\nu}}{\partial n} u^* d\Gamma =$$
$$+\frac{\sigma}{\nu_0}\int_\Omega \tilde{\nu}_{k-1} u^*_{k-1} d\Omega + \frac{\sigma}{\nu_0}\int_\Omega I u^* d\Omega -$$
$$-\frac{\sigma}{\nu_0}\left(\int_\Gamma \tilde{\nu} U_j n_j u^* d\Gamma - \int_\Omega \tilde{\nu} U_j \frac{\partial u^*}{\partial x_j} d\Omega\right) -$$
$$-\frac{\sigma}{\nu_0}\left(\int_\Gamma \nu_t \frac{\partial \tilde{\nu}}{\partial x_j} n_j u^* d\Gamma - \int_\Omega \nu_t \frac{\partial \tilde{\nu}}{\partial x_j}\frac{\partial u^*}{\partial x_j} d\Omega\right), \quad (13)$$

where I is used for the model source terms. For the Spalart-Allmaras model it is defined as:

$$I = C_{b2}\left(\frac{\partial \tilde{\nu}}{\partial x_j}\right)^2 + C_{b1}\left[1 - F_{t2}\right]\tilde{S}\tilde{\nu} -$$
$$-\left[C_{w1}F_w - \frac{C_{b1}}{\kappa^2}F_{t2}\right]\left[\frac{\tilde{\nu}}{d_n}\right]^2. \quad (14)$$

In the final discrete form of the equation the source term I is split into the production and destruction terms and linearised to improve the numerical stability.

3 THE NUMERICAL ALGORITHM

3.1 Discrete Form

In order to obtain the solutions to the governing equations, the solution domain is divided into C domain cells also called sub-domains comprised of 9 nodes (Fig. 1) and E boundary elements;

$$\Omega = \sum_{c=1}^{C}\Omega_c, \quad \Gamma = \sum_{e=1}^{E}\Gamma_e, \quad (15)$$

The classic single domain BEM is used for the calculation of boundary vorticity values by Eq. (10). However, all other equations are discretised using the domain decomposition approach, also called sub-domain BEM. The basic idea behind this approach is to split the solution domain into multiple sub-domains, similar to the cells used in the finite element methods. The sub-domains are then interconnected by the appropriate compatibility and equilibrium conditions corresponding to each sub-domain. This approach leads to an overdetermined sparse system matrix and in comparison with the classical BEM enables large savings in CPU time and computer memory.

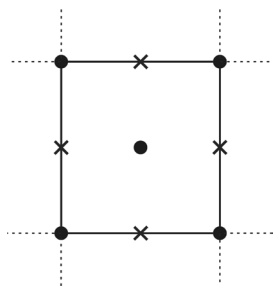

Fig. 1. *Sub-domain:the dot represents the function node and x the double node (node with function and its normal derivative as an unknown)*

As both the vorticity transport and the equations of the turbulence models are of convective-diffusive type, the general discrete form is presented in Eq. (16) where φ is used for the corresponding field function (vorticity, turbulent kinetic energy, etc.). The number of nodes in each element is marked with *n* and the general source term *S* is introduced that includes the sources obtained from time discretisation and various body source terms depending on the equation solved (f^m for the vorticity transport equation, *I* for the turbulence model etc.)

$$c(\xi)\phi(\xi,t)+\sum_{e=1}^{E}\{h_e\}^T\{\phi\}^n-\sum_{e=1}^{E}\{g_e\}^T\left\{\frac{\partial\phi}{\partial n}\right\}^n=$$
$$=\frac{1}{\nu_0}\left[-\sum_{e=1}^{E}\{a_{e,j}\}^T\{U_j\phi\}^n+\sum_{c=1}^{C}\{d_{c,j}\}^T\{U_j\phi\}^n+\right.$$
$$+\sum_{e=1}^{E}\{a_{e,j}\}^T\left\{\nu_t\frac{\partial\phi}{\partial x_j}\right\}^n-\sum_{c=1}^{C}\{d_{c,j}\}^T\left\{\nu_t\frac{\partial\phi}{\partial x_j}\right\}-$$
$$\left.-\sum_{c=1}^{C}\{b_c\}^T\{S\}^n\right]. \qquad (16)$$

The integrals introduced in Eq. (16) are defined as:

$$h_e=\int_{\Gamma_e}\Phi^n\frac{\partial u^*}{\partial n}d\Gamma,\qquad g_e=\int_{\Gamma_e}\chi^n u^* d\Gamma,$$
$$a_{e,j}=\int_{\Gamma_e}\Phi^n n_j u^* d\Gamma,\qquad d_{c,j}=\int_{\Omega_c}\Psi^n\frac{\partial u^*}{\partial x_j}d\Omega,$$
$$b_c=\int_{\Omega_c}\Psi^n u^* d\Omega, \qquad (17)$$

with the functions χ, Φ and Ψ in our case representing the constant, quadratic and biquadratic interpolations.

3.2 The Solution Procedure

A brief schematic of the algorithm is presented in Fig. 2. All equations are solved sequentially within a global nonlinear loop – depending whether the turbulence model is included the loop terminates after the solution of the kinetic equation for the domain vorticity values or after solutions of equations of the turbulence model. The main convergence criterion is the convergence of the vorticity field with additional monitoring of the convergence of the turbulence model's values. As the kinetics equations are highly nonlinear, an under relaxation procedure is introduced to enable convergence of the solution. When the convergence of the solution meets the predefined accuracy the next time-step is initiated and the solution process repeated.

In regard to the velocity-vorticity formulation of the Navier-Stokes equations, boundary conditions for the vorticity transport Eq. (2) need to be supplied. They are obtained from the proper velocity boundary conditions and an initial vorticity field by solving Eq. (10). Due to the unknown initial value of the vorticity field, the solution of Eq. (10) has to be coupled with the vorticity transport equation (Eqs. (11) or (12)) in an iterative way. The Laplace fundamental solution is used in Eq. (10), as the equation is of the Poisson type. Unfortunately, in order to preserve the solenoidality of the velocity field, the equation needs to be solved in a global sense and its discretisation leading to a fully populated system matrix. It is possible to reduce the memory requirements of the algorithm by introducing fast wavelet, or some other similar method for the matrix compression [22] with negligible loss of accuracy.

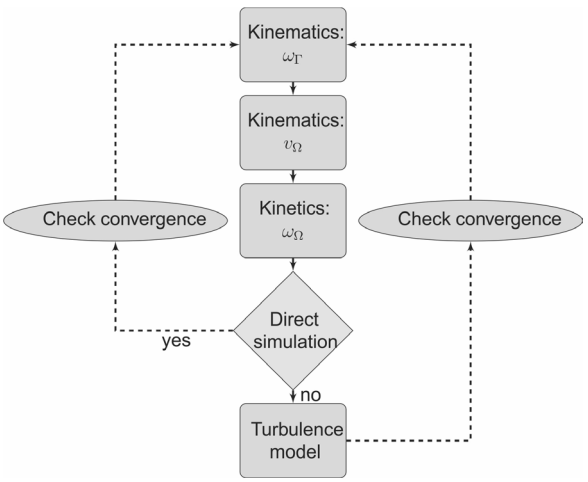

Fig. 2. *Flowchart of the numerical algorithm for the solution of governing equations in the velocity-vorticity form*

With the boundary values of the vorticity field known, Eq. (8) is solved for the domain velocity field. As Eq. (8) is the Poisson equation for the velocity field, the simple Laplace fundamental solution is used. The sub-domain integral method is used ([4] and [6]) for the discretisation of Eq. (8) and all the following Eqs. (11) or (12) and (13). This approach yields a rectangular system matrix, solved using the LSQR type solver and a diagonal pre-conditioner [5]. In general the sub-domains can be comprised of various numbers of nodes, depending on the interpolation used for the field function values. In our case, the sub-domains used contained nine mesh nodes, thus

enabling quadratic interpolation of the function values. The normal derivative (flux) values that are also part of the solution are interpolated with constant elements, so the same mesh nodes can be used as for the function values (see Fig. 1). Any higher order interpolation of the flux values would require either the inclusion of additional nodes or evaluation of the corner values of fluxes within each sub-domain, which is not recommended as the procedure can introduce additional errors.

The next step in the algorithm is the solving of the vorticity transport equations (Eqs. (11) and (12)) that provide the domain vorticity field values and thus complete the information needed for describing the laminar or (in the case of direct numerical simulation) the turbulent isothermal incompressible flow also. The algorithm iterates the steps described until satisfactory convergence within the vorticity field is achieved. Whilst in the first two parts of the algorithm (boundary vorticity values and domain velocity field calculations), the Laplace fundamental solution is used because of the mathematical simplicities of the equations in question, thus more advanced fundamental solutions can be used for the derivation of the integral statements of the vorticity transport equation. In our case the parabolic diffusion and the convection-diffusion fundamental solutions were implemented, as can be seen from Eqs (11) and (12).

In cases of non-isothermal flows or the RANS/URANS simulations, additional equations for the conservation of the energy and/or the turbulence models need to be solved. Those equations are of the same type as the vorticity transport equation and are thus solved in a similar fashion. It also has to be noted that when the low-Reynolds turbulence models are used, a classical linearisation procedure of the dissipation terms in the model's equations is used.

4 DESCRIPTION OF THE TEST CASE

The geometry of the test problem consisted of a plane channel with a square obstacle placed inside. For the unit length, the obstacle diameter D was taken (see Fig. 3), thus we defined the Reynolds number of the test case as $Re = DU_c/v_o$, where U_c was the centreline velocity at the inlet section. The blockage ratio of the test problem was defined by: $B = D/h = 1/8 = 0.125$, where h was the channel's height.

At the solid walls and on the surface of the square cylinder, no-slip boundary condition was prescribed. In order to enable better comparison with other authors **[8]** and **[10]**, the parabolic velocity profile was

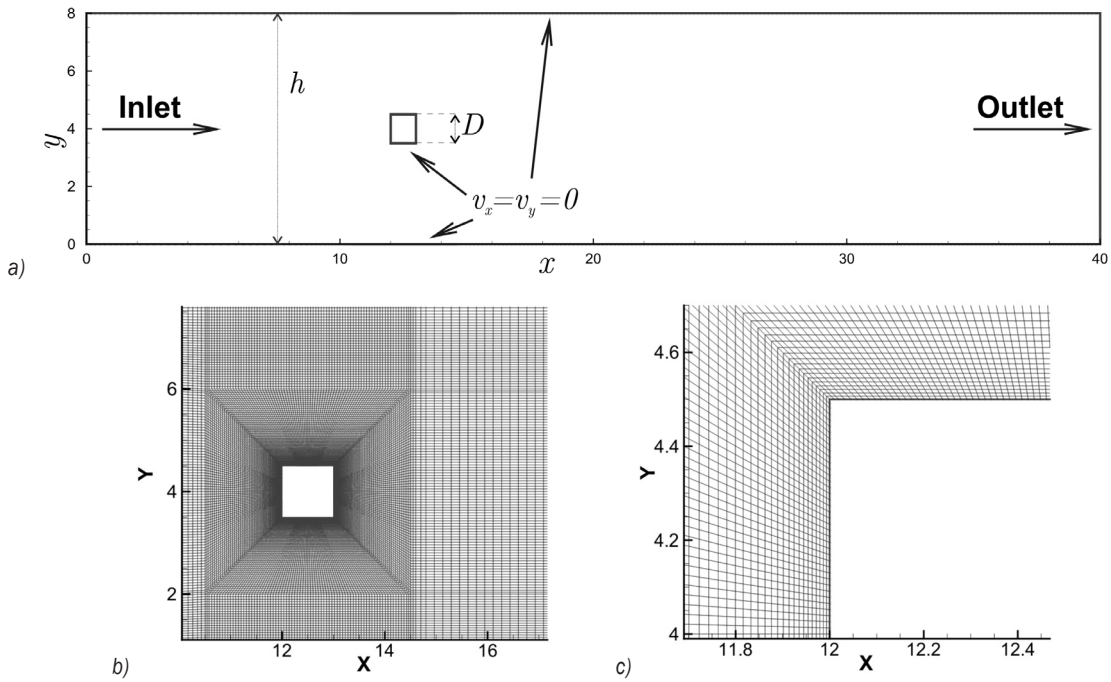

Fig. 3. *a) Geometry and boundary conditions of the test case, b) Mesh c: around the cylinder and c) Mesh c: zoom in; for finest numerical mesh used for the calculation, comprised of approximately 14700 sub-domains and 56342 mesh nodes (mesh lines connect the function nodes of sub-domains as presented in Fig. 1)*

prescribed at the inlet. The convective type boundary condition (as described in [23]) was used at the outlet for the velocity field whilst for all other variables the zero normal derivative was prescribed.

The flow was firstly calculated at the Reynolds numbers 100 and 150 on three different meshes, with the focus on increasing mesh density within the vicinity of the obstacle (see Fig. 3).

The coarsest mesh (mesh a) was comprised of around 4700 sub-domains (19132 mesh nodes), the mid-sized mesh (mesh b) had about 10700 sub-domains (43586 mesh nodes) and the finest one (mesh c) had about 14700 sub-domains (56342 mesh nodes). As the finest mesh had the greatest resolution within the vicinity of the cylinder, only this one was used in the calculation of flow at the Reynolds number 1000. The time-step used for simulations was $\Delta t = 2.5\times10^{-3}$ and $\Delta t = 2\times10^{-2}$ for URANS simulations, normalised as $t^* = (t\bar{U})/D$. t^* is non-dimensional time, t real time and $\bar{U}$ average velocity at the inlet of the channel.

4.1 Laminar Flow

Firstly the flow was calculated at the Reynolds numbers 100 and 150. For the initial values of the higher Reynolds simulation, the values were used as obtained by the $Re = 100$ simulation. Vortex shedding was initiated without introducing any artificial perturbations. Streamlines for quarters of the time period are shown in Fig. 4 for both flow cases. At the lower laminar Reynolds number the separation of the flow occurred at the cylinder trailing edge (see Fig. 4a). However, at the Reynolds number 150, the flow was also separated from the leading edges, as can be seen in Fig. 4b. The separations in both cases then caused periodic vortex shedding, also known as the Von Karman vortex street.

In Figs 5a and b the time variations of the drag and lift coefficients, evaluated from the forces acting on the cylinder are presented and the periodical nature of the flow can be clearly seen. The vortex shedding frequency f was evaluated from the lift coefficient

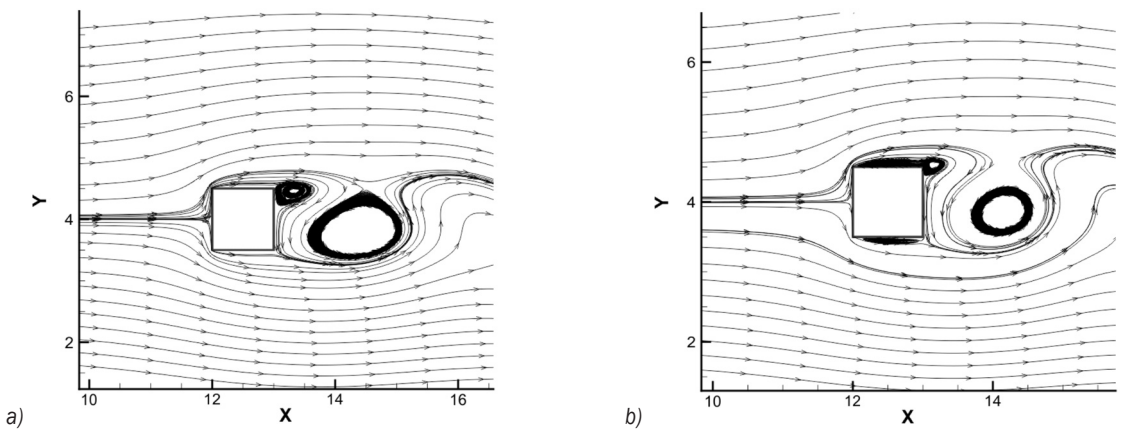

Fig. 4. *Streamlines of the flow at a) Re = 100 and b) Re = 150*

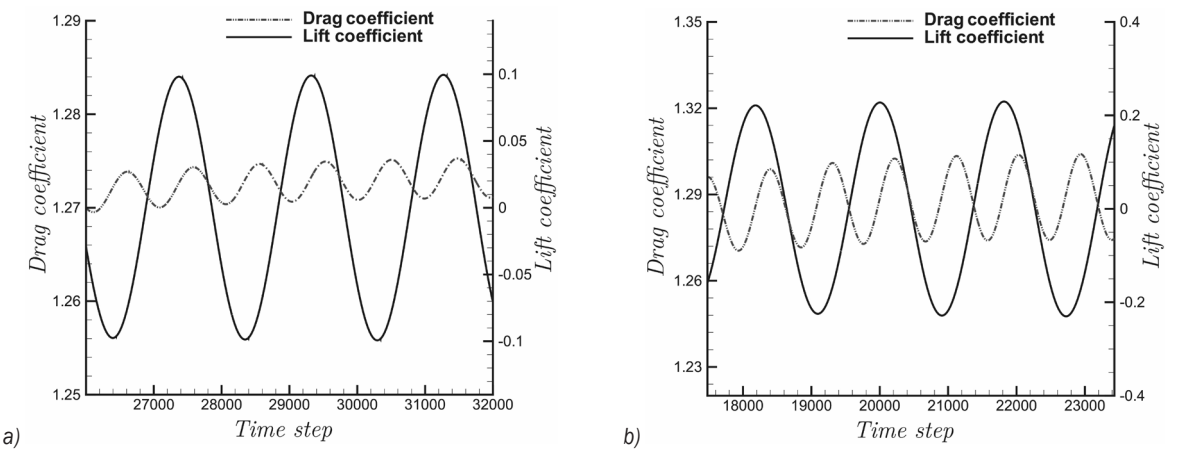

Fig. 5. *Time variation of the lift and drag coefficients for the Reynolds number; a) 100 and b) 150*

time series and used for the calculation of the Strouhal number, we defined by:

$$St = \frac{f \cdot D}{U_c}. \tag{18}$$

Table 1 presents the results for both the Strouhal number and the drag coefficient, together with comparison with available data from literature. General increases for both integral parameters were observed with the increase in the Reynolds number. When taken into account the results from the literature are quite widespread, the calculated Strouhal number matched the given data quite well, whilst the drag coefficient value seems to be systematically lower than the values from the literature.

A detailed comparison between the velocity profiles at the Reynolds number 100 was made with the results of Breuer et al. [10]. In order to make this comparison possible, the velocity profiles were extracted at approximately the same moment as described in the cited authors work; when the cross-stream velocity U_y at an axial position of 10 cylinder diameters downstream the cylinder, changed its sign from negative to positive. The comparisons between the velocity profiles are shown in Figs. 6a and b, where good agreement can be seen for meshes b and c used for the calculation of the flow, with minor deviations of the profiles towards the outlet section of the channel. Those deviations could most likely be attributed to the usage of relatively coarse mesh far away from the obstacle and a shorter computational domain as compared to [10].

Additional error was also produced by the finite length of time-step thus enabling only approximate determination of the time for the extraction of the velocity profiles.

The comparisons between the velocity profiles at the Reynolds number 150 are shown in Figs. 6c and

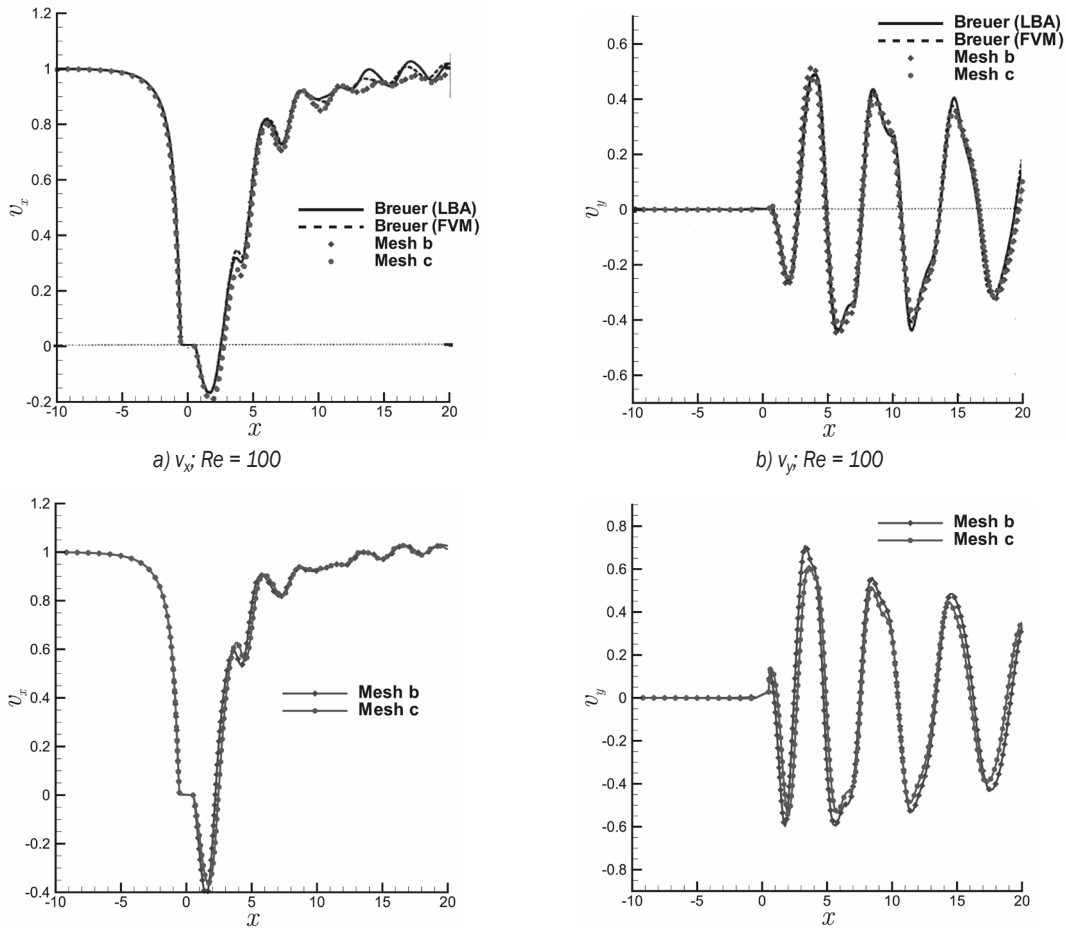

a) v_x; Re = 100 *b) v_y; Re = 100*

c) v_x; Re = 150 *d) v_y; Re = 150*

Fig. 6. *Instantaneous velocity profiles for Re = 100 and Re = 150 at the middle of the channel at a certain moment (see text for explanation), compared with the results of [9]*

d. As no data for the profiles could be found in the literature, the comparison was only made between meshes b and c.

At the higher Reynolds number the velocity profile was qualitatively similar to the profiles at the Reynolds number 100, with the higher maximum values within the velocity field.

Table 1. *Comparison between the Strouhal number and drag coefficient for Reynolds 100 and 150*

Re	Mesh	St	Cd
100	Breuer [10]	0.139	1.35
	Lamura [11]	0.133	1.38
	Turki [13] and [14]	0.134	1.40
	Galletti [12]	0.138	-
	Mesh a	0.129	1.33
	Mesh b	0.135	1.31
	Mesh c	0.137	1.27
150	Breuer [10]	0.147	1.33
	Turki [13] and [14]	0.136	1.38
	Galletti [12]	0.144	-
	Mesh a	0.133	1.43
	Mesh b	0.141	1.39
	Mesh c	0.147	1.29
200	Mesh c	0.151	1.37
250	Mesh c	0.155	1.46

4.2 Turbulent Flow

In order to obtain initial values for the flow field, the calculations were initiated at the Reynolds number 500 on the most refined grid for a few hundred time-steps in order to provide initial values for higher Reynolds calculations. The Reynolds number was then increased to the final value of $Re=1000$. As we have defined the Reynolds number in the same manner as in the reference literature (with obstacle width and maximum inlet velocity), it has to be noted that the Reynolds number based on the channel width and bulk velocity is around 5300. Although physically less appropriate, the parabolic velocity profile was used at the inlet in order to enable easier and more accurate comparisons between the experimental and numerical data of [8]. The flow was calculated for direct solutions of the governing equations (dubbed the quasi-direct numerical simulation (qDNS) due to the mesh being insufficiently refined) and the modified governing equations in the URANS mode.

In Figs. 7a and b the time series for the drag and lift coefficient are presented for the direct solution of the governing equations for both the parabolic-diffusive and the convective-diffusive fundamental solutions. From these series, the loss of periodicity

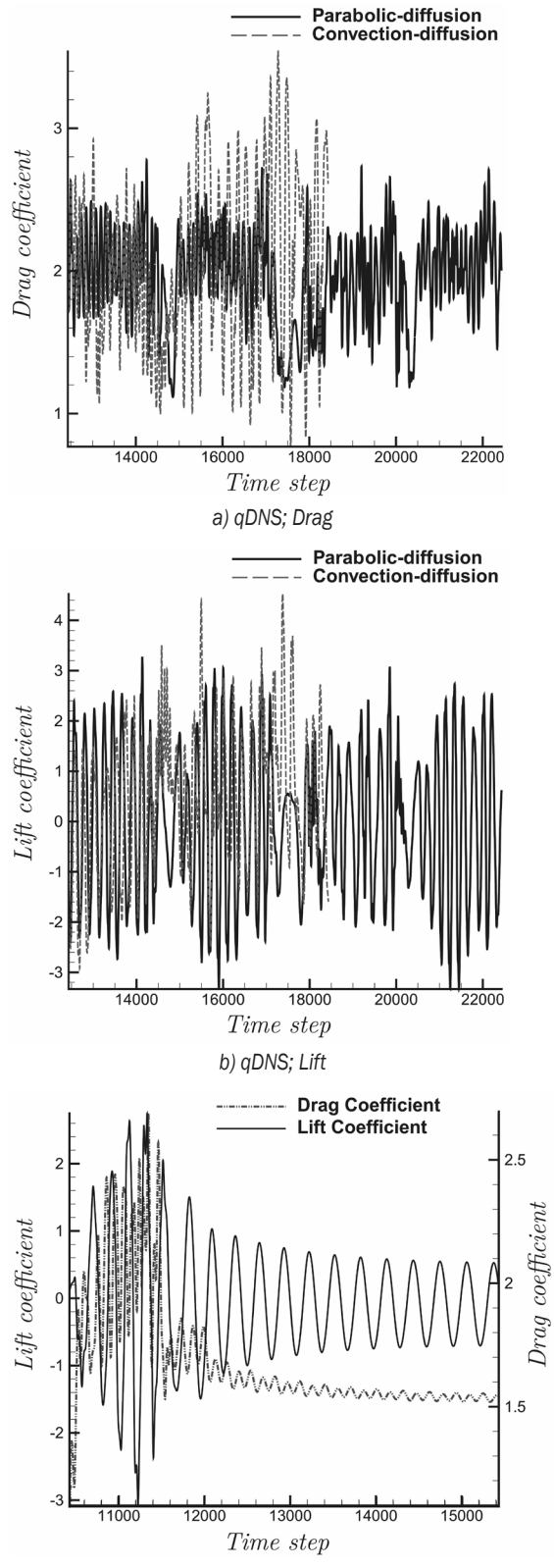

a) qDNS; Drag

b) qDNS; Lift

c) URANS; Drag and lift

Fig. 7. *Time series of lift and drag coefficient at Re = 1000 for qDNS and URANS simulations*

of the flow can be observed in the qDNS simulation. This is also confirmed by the experimental results of [8] at blockage ratios of 1/4 and 1/6. As the equations were solved in a direct manner, the small structures in the flow were limited only by a time-step and a mesh resolution. In Fig. 8a the streamlines are presented for the qDNS simulation showing a variety of different size flow structures. Fig. 7c presents the time series of the drag and lift coefficients for the URANS simulation. After a transient time, the smaller structures in the flow are dampened out by the imposed RANS model and the flow again becomes periodic. This is further shown in Fig. 8b regarding streamlines for the URANS simulation. Only large structures of the flow are observed. Having only large structures captured by the simulation, the simulated flow is qualitatively similar in behaviour to the laminar flow. Furthermore the dampening of the smaller structures by the increased viscosity of the URANS model seemed to lower the average value of the drag coefficient in comparison with the direct simulation result.

The flow at the Reynolds number 1000 showed highly nonlinear behaviour thus the frequency for the calculation of Strouhal number was obtained by FFT analysis of the lift coefficient signal (Fig. 7b). The drag coefficient was obtained by averaging the signal (Fig. 7a).

Table 2. *Comparison between the Strouhal number and the average drag coefficient for the flow at the Reynolds number of 1000*

	B	St	Cd
Davis exp.	1/4	0.179	2.37
Davis num.	1/4	0.144	1.88
Davis exp.	1/6	0.153	2.11
Davis num.	1/6	0.131	1.76
qDNS	1/8	0.157	1.94
URANS-SA	1/8	0.114	1.53

A comparison of the data from [8], found in the literature, was made between both the Strouhal number and the drag coefficient in Table 2. Although the ratio of the cylinder diameter to the channel width (B) was similar but not equal, no other data at this Reynolds number could be found for the geometry used in our simulations. The Strouhal number and the drag coefficient values in Table 2 given by the URANS simulation show values noticeably lower than in the reference data, most likely due to the imposed model dampening out smaller flow structures with the artificially increased eddy viscosity from the model.

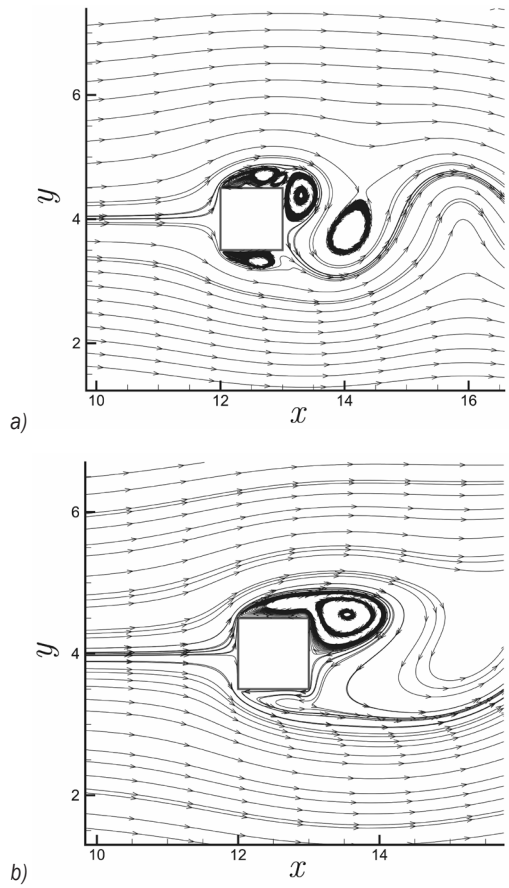

Fig. 8. *Streamlines at Re = 1000; a) in qDNS simulation and b) in URANS simulation*

5 CONCLUSIONS

Whilst many other discretisation methods received a lot more attention in the past, the usage of the boundary element method for the discretisation of the governing equations of the fluid flow is not widely known. The uses of fundamental solutions and with that the appropriate descriptions of some of the governing physics make this method appealing for use in fluids and could with more refinement come close or even surpass modern discretisation methods. Furthermore, as no artificial diffusivity is present within the discretisation scheme, as a direct consequence of the usage of Green's functions, the use of the DNS type simulations would be possible without additional changes of the algorithms.

This paper derived at URANS type turbulence models for the velocity-vorticity forms of the Navier-Stokes equations. The governing equations are discretized by the boundary element method. Boundary values of vorticity are determined as a part of the algorithm. Vorticity transport and

turbulence model equations are solved using a domain decomposition approach.

The algorithm is tested on the flow over the square obstacle in a channel at laminar and turbulent flow regimes. Velocity profiles, the estimated Strouhal number and drag coefficient for the laminar flow regime were compared with the benchmark results of other authors and proved the validity of the algorithm.

The turbulent flow regime was simulated at Reynolds number 1000 using quasi DNS and URANS approaches using Spalart-Allmaras turbulence model. Time traces of the drag and lift coefficient have been presented as well as average values compared with experimental data. Good agreement was observed.

6 REFERENCES

[1] Škerget, L., Hriberšek, M., Žunič, Z. (2003). Natural convection flows in complex cavities by BEM. *International Journal of Numerical Methods for Heat & Fluid Flow*, vol. 13, no. 6, p. 720-735, **DOI:10.1108/09615530310498394**.

[2] Popov, V., Power, H. (1999). The DRM-MD integral equation method: an efficient approach for the numerical solution of domain dominant problems. *International Journal for Numerical Methods in Engineering*, vol. 44, no. 3, p. 327-353, **DOI:10.1002/(SICI)1097-0207(19990130)44:3<327::AID-NME506>3.0.CO;2-6**.

[3] Taigbenu, A.E. (1995). The green element method. *International Journal for Numerical Methods in Engineering*, vol. 38, no. 13, p. 2241-2263, **DOI:10.1002/nme.1620381307**.

[4] Škerget, L., Rek, Z. (1995). Boundary-domain integral method using a velocity-vorticity formulation. *Engineering Analysis with Boundary Elements*, vol. 15, no. 4, p. 359-370, **DOI:10.1016/0955-7997(95)00036-N**.

[5] Paige, C.C., Saunders, M.A. (1982). LSQR: An algorithm for sparse linear equations and sparse least squares. *ACM Transactions on Mathematical Software (TOMS)*, vol. 8, no. 1, p. 43-71, **DOI:10.1145/355984.355989**.

[6] Lupše, J., Škerget, L., Ravnik, J. (2014). Velocity–vorticity RANS turbulence modeling by boundary element method. *Engineering Analysis with Boundary Elements*, vol. 39, p. 44-52, **DOI:10.1016/j.enganabound.2013.11.004**.

[7] Ternik, P., Rudolf, R. (2014). Laminar forced convection heat transfer characteristics from a heated cylinder in water based nanofluids. *International Journal of Simulation Modelling*, vol. 13, no. 3, p. 312-322, **DOI:10.2507/IJSIMM13(3)5.271**.

[8] Davis, F.W., Moore, F., Purtell, P. (1984). A numerical-experimental study of confined flow around rectangular cylinders. *Physics of Fluids*, vol. 27, no. 1, **DOI:10.1063/1.864486**.

[9] Mukhopadhyay, A., Biswas, G., Sundararajan, T. (1992). Numerical investigation of confined wakes behind a square cylinder in a channel. *International Journal for Numerical Methods in Fluids*, vol. 14, no. 12, p. 1473-1484, **DOI:10.1002/fld.1650141208**.

[10] Breuer, M., Bernsdorf, J., Zeiser, T., Durst, F. (2000). Accurate computations of the laminar flow past a square cylinder based on two different methods: lattice-boltzmann and finite volume. *International Journal of Heat and Fluid Flow*, vol. 21, no. 2, p. 186-196, **DOI:10.1016/S0142-727X(99)00081-8**.

[11] Lamura, A., Gompper, G. (2002). Numerical study of the flow around a cylinder using multiparticle collision dynamics. *The European Physical Journal E: SoftMatter and Biological Physics*, vol. 9, no. 5, p. 477-485, **DOI:10.1140/epje/i2002-10107-0**.

[12] Galletti, B., Bruneau, C.H., Zannetti, L., Iollo, A. (2004). Low-order modelling of laminar flow regimes past a confined square cylinder. *Journal of Fluid Mechanics*, vol. 503, p. 161-170, **DOI:10.1017/S0022112004007906**.

[13] Turki, S., Abbassi, H., Ben Nasrallah, S. (2003). Two-dimensional laminar fluid flow and heat transfer in a channel with a built-in heated square cylinder. *International Journal of Thermal Sciences*, vol. 42, no. 12, p. 1105-1113, **DOI:10.1016/S1290-0729(03)00091-7**.

[14] Turki, S., Abbassi, H., Nasrallah, S.B. (2003). Effect of the blockage ratio on the flow in a channel with a built-in square cylinder. *Computational Mechanics*, vol. 33, no. 1, p. 22-29, **DOI:10.1007/s00466-003-0496-2**.

[15] Kelkar, K.M., Patankar, S.V. (1992). Numerical prediction of vortex shedding behind square cylinders. *International Journal of Numerical Methods for Fluid*, vol. 14, no. 3, p. 327-341, **DOI:10.1002/fld.1650140306**.

[16] Okajima, A. (1982). Strouhal numbers of rectangular cylinders. *Journal of Fluid Mechanics*, vol. 123, p. 379-398, **DOI:10.1017/S0022112082003115**.

[17] Škerget, L., Samec, N. (2005). BEM for the two-dimensional plane compressible fluid dynamics. *Engineering Analysis with Boundary Elements*, vol. 29, no. 1, p. 41-57, **DOI:10.1016/j.enganabound.2004.08.007**.

[18] Kim, J., Moin, P., Moser, R. (1987). Turbulence statistics in fully developed channel flow at low Reynolds number. *Journal of Fluid Mechanics*, vol. 177, no. 1, p. 133-166, **DOI:10.1017/S0022112087000892**.

[19] Wu, J.C., Thompson, J.F. (1973). Numerical solutions of time-dependent incompressible Navier-Stokes equations using an integro-differential formulation. *Computers & Fluids*, vol. 1, no. 2, p. 197-215, **DOI:10.1016/0045-7930(73)90018-2**.

[20] Spalart, P.R., Allmaras, S.R. (1994). A one-equation turbulence model for aerodynamic flows. *La Recherche Aérospatiale*, vol. 1, no. 1, p. 5-21, **DOI:10.2514/6.1992-439**.

[21] Škerget, L., Ravnik, J. (2009). BEM simulation of compressible fluid flow in an enclosure induced by thermoacoustic waves. *Engineering Analysis with Boundary Elements*, vol. 33, no. 4, p. 561-571, **DOI:10.1016/j.enganabound.2008.08.003**.

[22] Ravnik, J., Škerget, L., Hriberšek, M. (2004). The wavelet transform for BEM computational fluid dynamics. *Engineering Analysis with Boundary Elements*, vol. 28, no. 11, p. 1303-1314, **DOI:10.1016/j.enganabound.2004.05.002**.

[23] Orlanski, I. (1976). A simple boundary condition for unbounded hyperbolic flows. *Journal of Computational Physics*, vol. 21, no. 3, p. 251-269, **DOI:10.1016/0021-9991(76)90023-1**.

Strojniški vestnik - Journal of Mechanical Engineering 61(2015)4, 265-272
DOI:10.5545/sv-jme.2014.2291
Original Scientific Paper
Received for review: 2014-11-10
Received revised form: 2015-02-27
Accepted for publication: 2015-03-05

Research on the Position-Pressure Master-Slave Control for a Rolling Shear Hydraulic Servo System

Wang Jun[1] – Sun Binyu[1,*] – Huang Qingxue[1] – Li Hongzhou[2] – Han Heyong[1]
[1] Taiyuan University of Science and Technology, China
[2] Hebei WenFeng Iron and Steel Co., China

The position-pressure master-slave control of hydraulic servo system is a dual closed-loop system, which takes position closed loop as the main control system, pressure closed loop as the supplementary, bringing these two seemingly contradictory theories together while simultaneously control the system. When the position error value is bigger than the threshold value, the system will transfer the pressure signal to the signal which will be added to the position signal, and regulate the system. This paper first builds a mathematical model of the hydraulic servo system position-pressure master-slave control, then simulates the system with AMEsim and Matlab softwares, which verifies the feasibility of this function. Finally, experiments are conducted using the new function, and the results show that position-pressure master-slave control can improve the precision and stability of hydraulic servo system; this new function can also be applied to other high speed, high precision and heavy equipment.

Keywords: position control, pressure control, master-slave control-hydraulic servo system, simulation, dual closed-loop system

Highlights
- *Proposed a new position-pressure master-slave control function for double-sided rolling shear.*
- *Calculating a position-pressure conversion model.*
- *Building a mathematical model of the hydraulic system of rolling shear.*
- *Improving the control precision and stability of hydraulic system.*

0 INTRODUCTION

Hydraulic double-sided rolling shear, the most advanced shearing machine, cuts off steel plates into a specified size [1], which is an important part of rolling production line and it will determine whether the quality of plates is good or not. Asymmetrical, valve controlling an asymmetrical cylinder (shown in Fig. 1) is the key to the hydraulic system of double-sided rolling shear, which uses a position-closed loop to make the cylinders move in order to ensure the rolling shear cutting off the steel plates according to the routine action.

Hydraulic rolling shear cuts off the steel plates with two cylinders moving harmonically along the given curve; the process is shown in Fig. 2. First, the left cylinder moves (shown as Fig. 2a). Then, when it moves to the designated place, the right cylinder begins to move (shown in Fig. 2b). Next, when the blade is moving to the place as shown in Fig. 2c, the rolling shear completes the action. Finally, the two cylinders retract to the initial position; a full action is completed, as shown in Fig. 2d. This equipment is simple, powerful, and highly reliable.

Usually, hydraulic rolling shear adopts position control to make the cylinder move along the specified curve, while (when shearing thick steel plates) the pressure of the two cavities of the cylinder is always too low to push the upper blade moving along the desired curve to cut off the steel plates. As a result, the quality of the sheared plates will be poor (shown as Fig. 3). Therefore, how to improve the effect of controlling of rolling shear is a widely studied issue

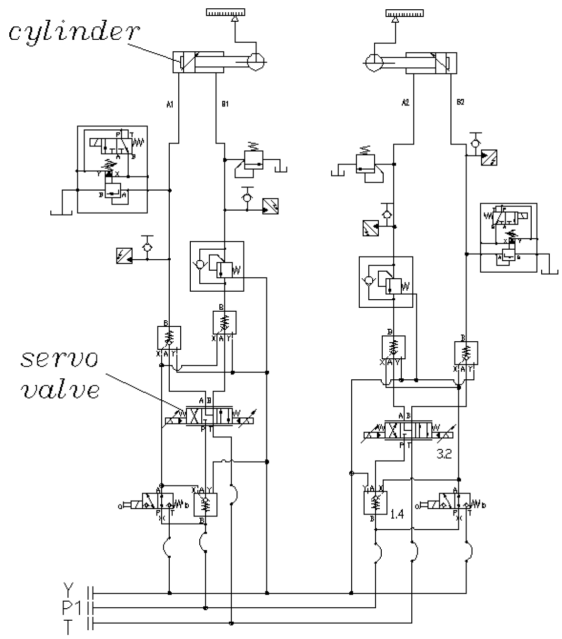

Fig. 1. *The hydraulic scheme of hydraulic rolling shear*

*Corr. Author's Address: Taiyuan University of Science and Technology, No. 66 Waliu Street, Taiyuan, China, sunby_sby@126.com

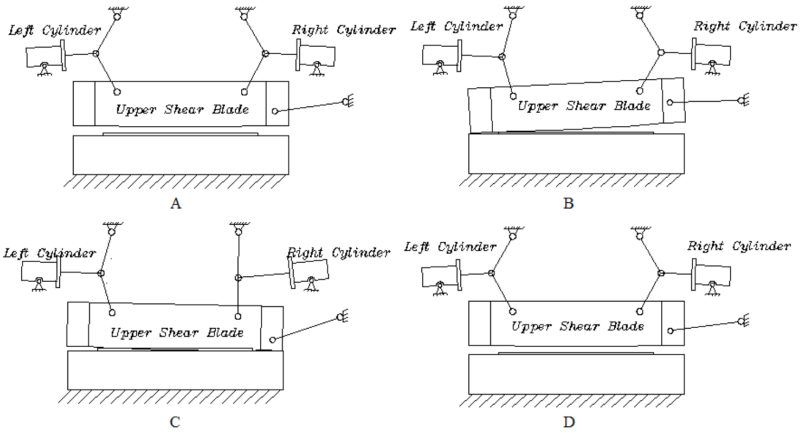

Fig. 2. *The shearing process of hydraulic rolling shear*

[2]. Some researchers want to improve the structure of the rolling shear. Huang et al. design a new mechanism [3], which is powerful but heavy. Optimizing the mechanism of rolling shear cannot solve the problem of powerless; some researchers propose new control algorithms to improve the performance of the position control: Quan and Xu [4] put forward a new control method combining pressure and position in series and parallel, while Madani and Moallem [5] propose position/force control, but both of them are unstable when switching the pressure either to position control or position to pressure control. Bessa et al. [6] put forward a new type of control using sliding mode control, while Kim et al. [7] use QFT to perfect the position control. These are too complex to apply to the production in factories.

This paper puts forward a new control method: pressure-position master-slave control for double-sided rolling shear, which takes the position closed loop as the main control system, and the pressure closed loop as supplementary. This new function can make the cylinder move along the desired curves and will not be affected by the external loads, so the shape of the sheared plates will be improved. It has both theoretical significance and practical significance for improving the control precision and performance of heavy and high-speed equipment.

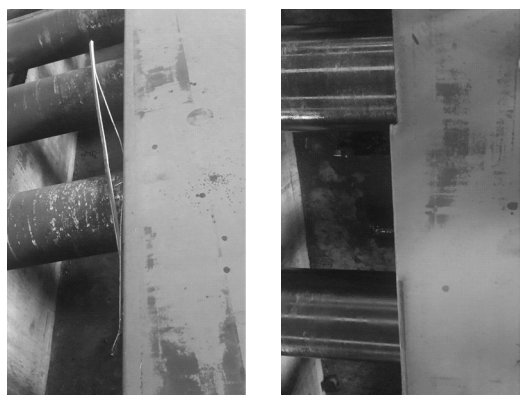

Fig. 3. *Defect of steel plate*

1 BUILD THE MATH MODEL

The structure diagram of position-pressure master-slave control is shown in Fig. 4.

The pressure signal from cylinder is detected by the pressure sensors and sent to the pressure-position conversion model; the master-slave controller will

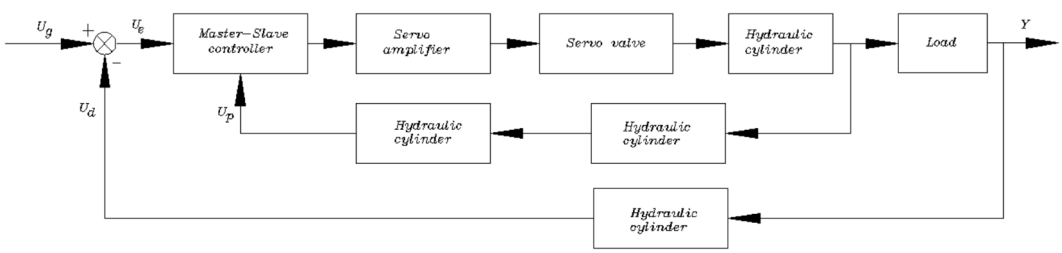

Fig. 4. *Structure diagram of position-pressure master-slave control*

then judge when the pressure signal will be added to the position signal, if the position signal error is bigger than the threshold, the pressure closed loop is connected, the converted pressure signal is a compensation for the position signal to adjust the input signal, rapidly enlarging the flow of servo valve , and accelerating the speed of cylinder, so the position error of cylinder will be small, the pressure and position of cylinder will be in control. Meanwhile, the position control will not be affected by the pressure control. Thus, this new function can simultaneously control the position and the pressure of the cylinder.

The schematic of the asymmetrical servo valve controlling asymmetrical cylinder is shown in Fig. 4. This paper researches the mathematical model when the blade begins to contact the steel plates, F_L is a constant, the equilibrium equation for the servo cylinder and the loads at two adjacent moments, which are the beginning and ending points of the shortest time that the pressure sensor can obtain:

$$A_1 p_{t-1} = m_t a_{t-1} + B_p \dot{x}_{t-1} + K x_{t-1} + F_L, \quad (1)$$

$$A_1 p_t = m_t a_t + B_p \dot{x}_t + K x_t + F_L. \quad (2)$$

Eq. (3) is subtracted from Eq. (2) to Eq. (1):

$$\frac{X_t - X_{t-1}}{P_t - P_{t-1}} = \frac{A_1}{K} - \frac{M_t(A_t - A_{t-1})}{P_t - P_{t-1}} - \frac{B_p(V_t - V_{t-1})}{P_t - P_{t-1}}. \quad (3)$$

When shearing the plates, $M_t(A_t - A_{t-1})$ and $B_p(V_t - V_{t-1})$ will be ignored because the accelerated speed and speed are changing so small.

The simplified Eq. (3) is shown as Eq. (4).

$$K_t = \frac{X_t - X_{t-1}}{P_t - P_{t-1}} = \frac{A_1}{K}. \quad (4)$$

Thus, the computation formula of position-pressure conversion coefficient is shown as Eq. (5):

$$K_t = \left|\frac{\Delta X}{\Delta P}\right| = \left|\frac{X_t - X_{t-1}}{P_t - P_{t-1}}\right|, \quad (5)$$

where K_t is the position-pressure conversion gain, ΔP is the difference in pressure between two moments, ΔX is the difference in position between two moments, X_t is the position signal of cylinder at NO.t moment, X_{t-1} is the position signal of cylinder at NO.t–1 moment, P_t is the pressure signal of cylinder at NO.t moment, and P_{t-1} is the pressure signal of cylinder at NO.t–1 moment.

When the upper blade begins to contact the steel plate, the equilibrium equation is shown as Eq. (6):

$$p_1 A_1 - p_2 A_2 = F_L, \quad (6)$$

where p_1 is the pressure of the blind end of the cylinder, p_2 is the pressure of the rod end of the cylinder, A_1 is the area of the piston, A_2 is the area of the piston rod, and F_L is the load of servo cylinder.

The positive direction is where the rod stretches out, the pressure of system load is P_L, flow is q_L:

$$P_L = \frac{F_L}{A_1}, \quad (7)$$

and $F_L = P_1 A_1 - P_2 A_2$.

So, the Eq. (7) can be transferred to be:

$$P_L = \frac{F_L}{A_1} = \frac{P_1 A_1 - P_2 A_2}{A_1} = P_1 - P_2 \frac{A_2}{A_1} = P_1 - \lambda P_2, \quad (8)$$

where $\lambda = \frac{A_2}{A_1}$.

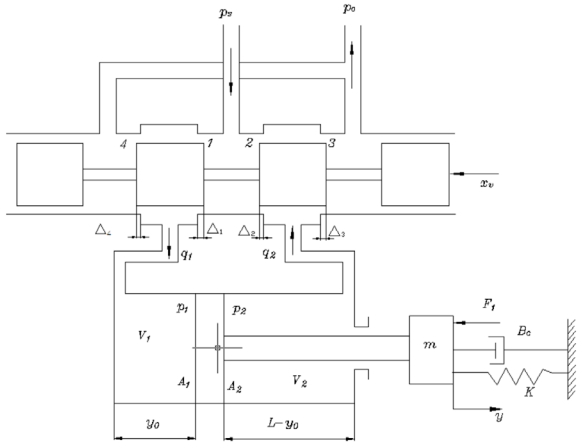

Fig. 5. *The schematic of servo asymmetrical controlling asymmetrical cylinder*

The flow equation of the valve is:

$$q_L = K_q x_v - K_c p_L. \quad (9)$$

Because this system uses asymmetrical valve to control asymmetrical cylinder, the flow gain K_q and flow-pressure coefficient K_c are shown as following:

$$K_q = \frac{\partial q_L}{\partial x_v} = C_d w_1 \sqrt{\frac{2(p_s - p_1)}{\rho(1+\lambda)}}, \quad (10)$$

$$K_c = \frac{\partial q_L}{\partial p_L} = \frac{C_d w_1}{\sqrt{2\rho(1+\lambda)(p_s - p_1)}}. \quad (11)$$

Assuming that the connect pipelines between servo valve and cylinder are short, symmetric and thick; the pressure loss due to frictional resistance

and dynamic effect of pipe are ignored; the oil bulk modulus and the oil temperature are constants; the internal and external leakage are laminar flow.

According to Fig. 5, the flow into the cylinder is q_1 out of cylinder is q_2, so, the flow equations are:

$$q_1 = \frac{dV_1}{dt} + C_{ip}\left(p_1 - p_2\right) + C_{ep}p_1 + \frac{V_1}{\beta_e}\frac{dp_1}{dt}, \quad (12)$$

$$q_2 = \frac{dV_2}{dt} + C_{ip}\left(p_1 - p_2\right) + C_{ep}p_2 + \frac{V_2}{\beta_e}\frac{dp_2}{dt}, \quad (13)$$

where V_1 is the effective volume of the blind end of the cylinder, V_2 is the effective volume of the rod end of the cylinder, C_{ip} is the internal leakage coefficient, C_{ep} is the external leakage coefficient, and β_e is the oil bulk modulus of elasticity.

The volumes of the cavities of cylinder in the initial state are V_{10} and V_{20}. When the piston of the cylinder is moving x_p, the equations are as follows:

$$V_1 = V_{10} + A_1 x_p, \quad (14)$$

$$V_2 = V_{20} + A_2 x_p, \quad (15)$$

and

$$\frac{dV_1}{dt} = A_1\frac{dx_p}{dt}, \quad (16)$$

$$\frac{dV_2}{dt} = -A_2\frac{dx_p}{dt} = -A_1\frac{dx_p}{dt}. \quad (17)$$

The flow of cylinder is shown as following:

$$q_L = q_1 + \lambda q_2. \quad (18)$$

Put Eqs. (10) to (15) into (18), and simplify it:

$$q_L = q_1 + \lambda q_2 = C_{ip}(p_1 - p_2)(1+\lambda) + \\ + C_{ep}(p_1 - \lambda p_2) + (1+\lambda^2)A_1\frac{dx_p}{dt} + \frac{V_{10}}{\beta_e}\frac{dp_1}{dt} - \\ - \lambda\frac{V_{20}}{\beta_e}\frac{dp_2}{dt} + \frac{A_1 x_p}{\beta_e}\left(\frac{dp_1}{dt} + \lambda^2\frac{dp_2}{dt}\right). \quad (19)$$

The cylinder flow continuity equation can be obtained by linearizing Eq. (19) :

$$q_L = A_1\frac{dx_p}{dt} + C_{tp}p_L + \frac{V_t}{2\left(1-\lambda^2\right)\beta_e}\frac{dp_L}{dt}, \quad (20)$$

where: C_{tp} is the leakage coefficient of cylinder and

$$C_{tp} = \frac{1+\lambda}{1-\lambda^2}C_{ip} + \frac{1}{1-\lambda^2}C_{ep}.$$

Equilibrium equation between cylinder and load **[8]** to **[10]** is Eq. (21):

$$A_1 p_1 - A_2 p_2 = m_t\frac{d^2x_p}{dt^2} + B_p\frac{dx_p}{dt} + Kx_p + F_L, \quad (21)$$

and $A_2 = \lambda A_1$, the left of the Eq. (21) can be simplified as: $A_1p_1 - A_2p_2 = A_1(p_1 - \lambda p_2) = A_1 p_L$.

Then, we arrive at the Eq. (22) **[11]** to **[13]**:

$$A_1 p_L = m_t\frac{d^2x_p}{dt^2} + B_p\frac{dx_p}{dt} + Kx_p + F_L, \quad (22)$$

where m_t is the total mass of piston and loads refferred to piston, B_p is the viscosity damping coefficient, K is the spring stiffness of the load, and F_L is the external load.

Eqs. (9), (20) and (22) are Laplace transformed **[14]**:

$$Q_L = K_q X_v - K_c P_L, \quad (23)$$

$$Q_L = A_1 s X_p + C_{tp}P_L + \frac{V_t}{2\left(1-\lambda^2\right)\beta_e}sP_L, \quad (24)$$

$$A_1 p_L = m_t s^2 X_p + B_p s X_p + KX_p + F_L. \quad (25)$$

According to the equations above, the transfer function of the servo cylinder can be obtained, Eq. (25a):

$$X_p = \frac{\frac{K_q}{A_1}X_v - \frac{K_{ce}}{A_1^2}\left(1 + \frac{V_t}{2\left(1-\lambda^2\right)\beta_e K_{ce}}\right)F_L}{\frac{m_t V_t}{2\left(1-\lambda^2\right)\beta_e A_1^2}s^3 + \left(\frac{K_{ce}m_t}{A_1^2} + \frac{V_t B_p}{2\left(1-\lambda^2\right)\beta_e A_1^2}\right)s^2 + \left(1 + \frac{B_p K_{ce}}{A_1^2} + \frac{KV_t}{2\left(1-\lambda^2\right)\beta_e A_1^2}\right)s + \frac{KK_{ce}}{A_1^2}}. \quad (25a)$$

The gain of position sensor is [15]:

$$K_d = \frac{U_d}{Y}, \tag{26}$$

where U_d is the output of the position closed loop.

The transfer function of slave pressure control is:

$$U_p = P_L \cdot K_P \cdot K_t, \tag{27}$$

$$U_e = U_g - U_P - U_d, \tag{28}$$

where U_P is the output of slave pressure control, K_P is the gain of the pressure sensor, and K_t is the position-pressure conversion coefficient.

2 SIMULATIONS

This paper uses AMEsim software to simulate the hydraulic system of rolling shear, and SIMULINK software to simulate its control system. The hydraulic system model of rolling shear in AMEsim is shown in Fig. 6, and the control system in SIMULINK is shown in Fig. 7.

The system parameters in the simulation model are shown in Table 1.

First, only the position closed loop is used in the simulation system. The position and pressure curves are shown in Fig. 8, which indicates that when the

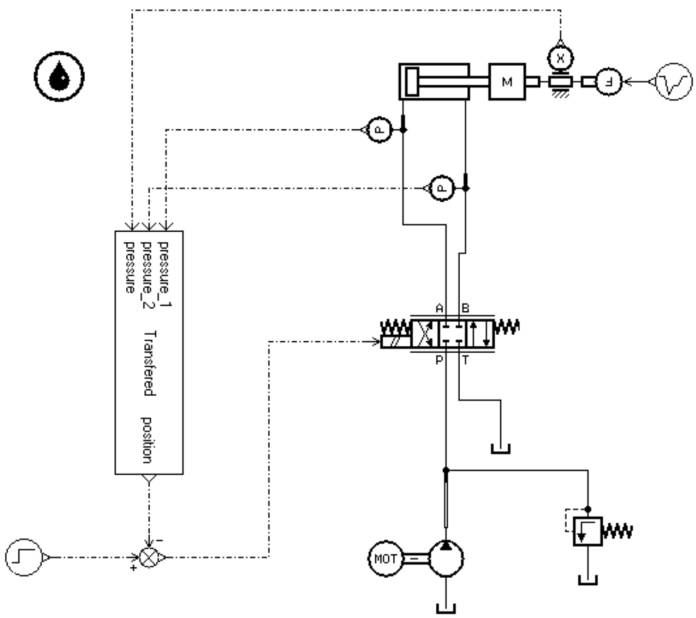

Fig. 6. *The hydraulic system model in AMEsim*

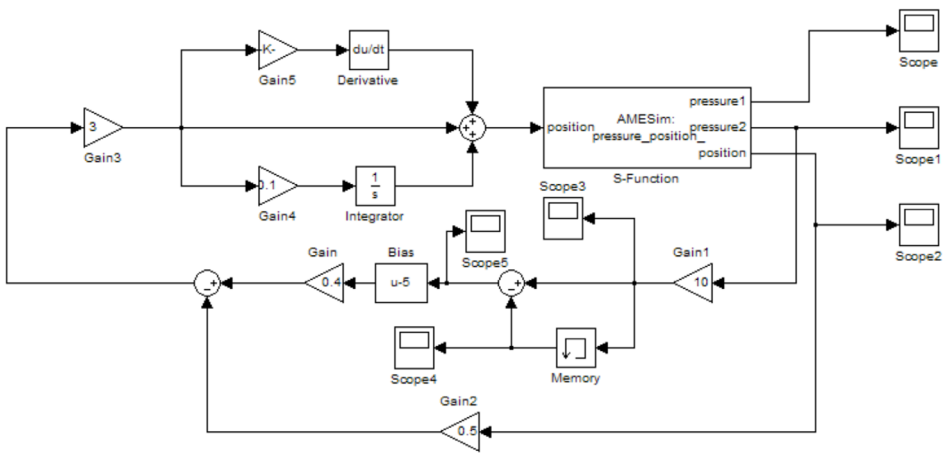

Fig. 7. *The control system model in SIMULINK*

external load is changing fast, the pressure will lag behind, and the cylinder cannot move along with the given curve, so that the rolling shear is not able to cut off the steel plates.

Table. 1. *Parameters of the system*

Working pressure	28 MPa	Oil elastic modulus	14000
Parameters of cylinder	510/380 mm	Cylinder stroke	477 mm
Oil density	900 kg/m^3	Dynamic mass	17000 kg
Frequency response of servo valve	35 Hz	Flow P-A of servo valve	1000 L/min
Pressure drop of servo valve	0.5 MPa	Flow B-T of servo valve	500 L/min
Damping ratio of servo valve	0.8	Flow A-T of servo valve	1000 L/min
Rated current of servo valve	40 mA	Flow P-B of servo valve	500 L/min
Gain 1	10	Gain 2	0.5
Gain 3	3	Gain 4	0.1
Gain 5	0.01	Gain	4
Flow gain of the servo valve	1.7 m^2/s	Flow-pressure gain of the servo valve	2.1×10^{-12} m^5/N×s

Fig. 9 shows the position and pressure curves when using position-pressure master-slave control, which indicates that the new function makes the system react fast and the position curve can follow the track of the given curve perfectly.

The results indicate that the cylinder can move along with the given curve using position-pressure master-slave control, and the pressure of the cylinder is stable, which is not affected by the external load. Thus, the pressure-position master-slave control can improve the precision and the stability of the hydraulic servo system.

3 EXPERIMENTS

The experiments are conducted on experimental double-sided rolling shear. The sheared steel plates are 30 mm in thick, 2100 mm in width. First, the experiments are conducted with the position closed loop only, and then using the position-pressure master-slave control instead. Finally, comparing the curves obtained by these two functions, the merits and demerits are analyzed. The servo valve used is 4WRTE32 produced by Rexroth; the pressure sensor used is HDA3840-A-400-000 produced by HYDAC.

Table 2 is the experimental data using the closed loop position only, and the Fig. 10 is the position

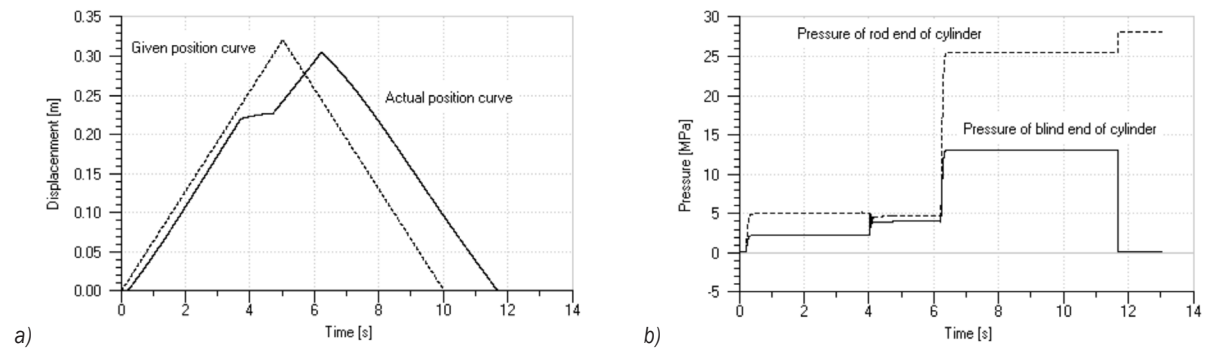

a) b)

Fig. 8. *a) The position curves and b) the pressure curves using position closed loop only*

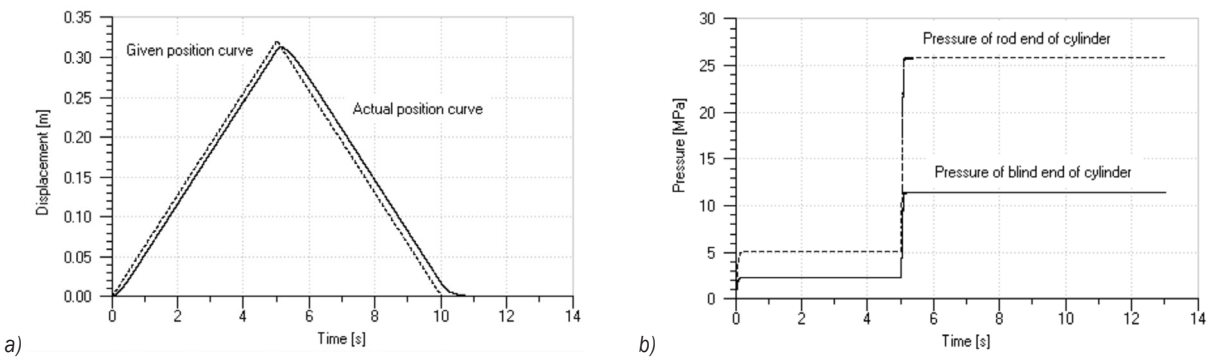

a) b)

Fig. 9. *a) The position curves and b) the pressure curves using position-pressure master-slave control*

curves and pressure curves fitted by software Origin according to the experimental data.

Table 2. *Experiment data*

Time [s]	Given displacement [mm]	Actual displacement [mm]	The rod end of the cylinder [mm]	The blind end of the cylinder [mm]
0	0	0	4.935	8.498
1	71.314	69.091	9.262	8.276
2	164.937	157.841	8.741	9.960
3	264.411	207.361	7.010	10.001
4	320	310.491	6.114	11.170
5	237.714	263.194	6.946	10.539
6	144.457	169.937	8.741	10.112
7	61.074	76.314	9.262	8.276
8	0	8.113	5.351	7.302

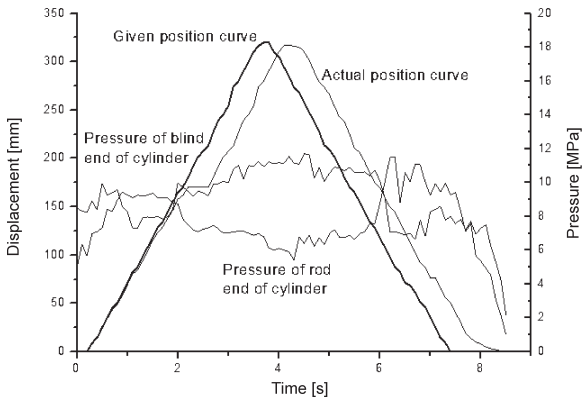

Fig. 10. *The position and pressure curves of rolling shear with position closed loop only*

Table 2 and Fig. 10 show that the actual position curve is defective; at about 2.3 s, the actual position curve is seriously deflected from the given position curve, the biggest error of position is 32 mm, and the pressure fluctuation is about 2.1 MPa.

Table 3. *Experiment data*

Time [s]	Given displacement [mm]	Actual displacement [mm]	The rod end of the cylinder [mm]	The blind end of the cylinder [mm]
0	0	0.264	4.9347	10.498
1	71.314	69.21	9.262	8.2764
2	164.937	163.18	9.7412	9.9609
3	264.411	262.832	6.2698	11.7554
4	320	320.424	5.9774	12.8276
5	237.714	241.722	6.9641	11.845
6	144.457	141.964	10.8895	6.982
7	61.074	59.064	10.4502	8.594
8	0	0.125	4.502	6.215

Then, the pressure closed loop is added to the system, using the position-pressure master-slave control. Table 3 shows data from laboratory, and the Fig. 11 shows position and pressure curves according to the data with the new method proposed in this paper.

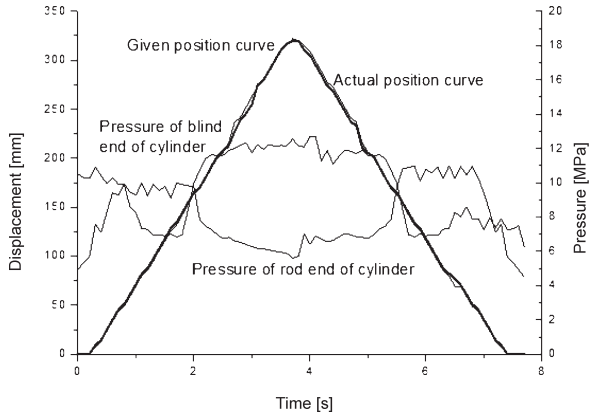

Fig. 11. *Position and pressure curves*

Table 3 shows the data of given displacement, actual displacement, pressure of the blind end of the cylinder and the pressure of the rod end of the cylinder in a whole process of rolling shear. Fig. 11 and Table 3 indicate that the biggest error between actual displacement and given displacement is 3 mm, the pressure fluctuation is less than what in which uses the closed loop position only. Compared to the results in Fig. 10, the position curve in Fig. 11 is perfect, and the following performance is better, so the rolling shear can cut off the steel plate to a level of quality that meets the standards of industrial production.

Simply put, when double-sided rolling shear using position-pressure master-slave control to cut off the steel plates, the position curve of the cylinder can follow the calculated curves well, the pressure is stable, the quality of sheared plates and the production efficiency are both improved, which can meet the demands of clients. Position-pressure master-slave control can improve the precision of the position and pressure of cylinider, making the rolling shear cut thicker plates.

4 CONCLUSIONS

Based on a practical issue, for solving the problems when the rolling shear cuts the steel plates, this paper puts forward a new position-pressure master-slave control function, which can improve the precision of position and pressure; putting these two seemingly contradictory theories together and improving the

quality of steel plates. This paper builds a mathematical model of the hydraulic system of rolling shear, and then simulates the hydraulic system by using AMEsim and SIMULINK; the results indicate that the new theory can be applied to practice. Experiments are conducted; the pressure curves and position curves obtained via simulation and experiment show that the position-pressure master-slave control is feasible and verify the theory put forward by this paper has practical value.

The position-pressure master-slave control proposed in this paper improves the anti-jamming capability, precision and stability of the system; thickness of sheared steel plates is increased by 35 % and the quality also be improved. It is easy to use in the plants and with other hydraulic servo systems with high speed, massive flows and heavy loads.

5 ACKNOWLEDGEMENT

This paper was supported by Technology Innovation Project for Postgraduate of Taiyuan University of Science and Technology (20134023); Ph.D. Programs Foundation of Ministry of Education of China (20111103); The Initial Funding of Doctor Research of Taiyuan University of Science and Technology (20122047); Provincial Fund for Young Scholars (2013021019-2), Provincial Fund for Technological Innovation (2013101013).

6 REFERENCES

[1] Han, H. Y., Huang, Q. X., Wang, J., Wang, J. (2013). The analysis of new hydraulic rolling shear servo system dynamic characteristics. *Proceedings of the Institution of Mechanical Engineers, Part B: Journal of Engineering Manufacture*, vol. 227, no. 3, p. 453-459, **DOI:10.1177/0954405412472667**.

[2] Yang, G. J., Yu, S. H., Zhang, H. C., Chen, G. D. (2009). Construction on the optimization designing system of shearing mechanism of rolling shear. *Journal of Machine Design*, vol. 29, no. 3, p. 63-66. (in Chinese)

[3] Huang, Q. X., Ma, L. F., Li, J. B. (2008). Principle of asymmetric crank mechanism of new-type rolling shear. *Chinese Journal of Mechanical Engineering*, vol. 44, no. 5, p. 119-123, **DOI:10.3901/JME.2008.05.119.** (in Chinese)

[4] Quan, L., Xu, X.Q. (2008). Simulation and test of electro-hydraulic servo position and pressure hybrid control principle. *Chinese Journal of Mechanical Engineering*, vol. 44, no. 9, p. 100-105 **DOI:10.3901/JME.2008.09.100.** (in Chinese)

[5] Madani, M., Moallem, M. (2011). Hybrid position/force control of a flexible parallel manipulator. *Journal of the Franklin Institute*, vol. 348, no. 6, p. 999–1012, **DOI:10.1016/j.jfranklin.2011.03.005**.

[6] Bessa, W.M., Dutra, M.S., Kreuzer, E. (2010). Sliding mode control with adaptive fuzzy dead-zone compensation of an electro-hydraulic servo-system. *Journal of Intelligent and Robotic Systems*, vol. 58, no. 1, p. 3-16, **DOI:10.1007/s10846-009-9342-x**.

[7] Kim, J.W., Xuan, D.J., Kim, Y.-B. (2008). Design of a force control system for a dynamic road simulator using QFT. *International Journal of Automotive Technology*, vol. 9, no. 1, p. 37-43, **DOI:10.1007/s12239-008-0005-x**.

[8] Tai, N.T., Kha, N.B., Ahn, K.K. (2010). Predictive position and force control for shape memory alloy cylinders. *Journal of Mechanical Science and Technology*, vol. 24, no. 8, p. 1717-1728, **DOI:10.1007/s12206-010-0504-3**.

[9] Zhao, W. Z., Sun, P. K., Liu, S., Lin, Y. (2012). Multi-objective optimization of active steering system with force and displacement coupled control. *Journal of Central South University*, vol. 19, no. 4, p. 974-981, **DOI:10.1007/s11771-012-1099-x**.

[10] Murakawa, M., Lu, Y. (1997). Precision cutting of sheets by means of a new shear based on rolling motion. *Journal of Materials Processing Technology*, vol. 66, no. 4, p. 232-239, **DOI:10.1016/S0924-0136(96)02529-0**.

[11] Lei, J. B., Wang, X. Y., Pi, Y. J (2013). Sliding mode control in position control for asymmetrical hydraulic cylinder with chambers connected. *Journal of Shanghai Jiaotong University (Science)*, vol. 18, no. 4, p. 454-459, **DOI:10.1007/s12204-013-1419-9**.

[12] Huang, F. (2011). *The Acceleration and Deceleration Algorithm and Simulation of Position and Pressure Control Conversion Process of Electro-Hydraulic Servo System*. Wuhan University of science and technology, HuBei.

[13] Han, H. Y., Wang, J., Wang, J., Huang, Q.X. (2012). Analysis of unsymmetrical valve controlling unsymmetrical cylinder stability in hydraulic leveler. *Nonlinear Dynamics*, vol. 70, no. 2, p. 1199-1203, **DOI:10.1007/s11071-012-0523-y**.

[14] Yu, J., Li, Y. (2011). Simulation on electro-hydraulic proportional position control system under pressure boundary conditions. *Advanced Materials Research*, vol. 186, p. 21-25, **DOI:10.4028/www.scientific.net/AMR.186.21**.

[15] Yi, J.G. (2015). Modelling and analysis of step response test for hydraulic automatic gauge control. *Strojniški vestnik - Journal of Mechanical Engineering*, vol. 61, no. 2, p. 115-122, **DOI:10.5545/sv-jme.2014.2046**.

Strojniški vestnik - Journal of Mechanical Engineering 61(2015)4, 273-282
DOI:10.5545/sv-jme.2014.2123
Original Scientific Paper
Received for review: 2014-08-15
Received revised form: 2015-01-14
Accepted for publication: 2015-02-26

Study of an Annular Two-Phase Thermosyphon Used as an Isothermal Source in Thermometry

Florencio Sánchez-Silva* – Ignacio Carvajal-Mariscal – Ariel E. Moreno-Cordobés – Pedro Quinto Diez – Miguel Toledo Velázquez

National Polytechnic Institute, School of Mechanical and Electrical Engineering, Mexico

The feasibility of using an annular two-phase thermosyphon (TPT) in thermometry was studied experimentally; the main results are presented in this paper. The TPT was conceived as an isothermal source for calibration purposes, using the comparison method. For this purpose, an annular TPT was designed, built and characterized, using water as a working fluid. In order to determine experimentally how isothermal the TPT annular surface can be, eight thermocouples were installed axially on its surface.

Tests were performed for two different cooling water flows 16.67 cm³/s and 4.17 cm³/s. For each cooling water flow, four heat power levels were supplied in the evaporation zone: (38, 154, 350, 1,385) W. The experimental results have shown that the thermal device works isothermal for power levels higher than 350 W, where the so-called bar effect is not present and the temperature measurement error is reduced.

Key words: thermometry, two-phase thermosyphons, isothermal, annular, calibration

Highlights

- *Using an annular two-phase thermosyphon as isothermal source in thermometry.*
- *Immersion depth of the temperature sensor is 21 cm.*
- *Higher values of heat supplied promoted isothermicity.*
- *Device efficiency was higher than 94%.*
- *The system accomplished all the requirements for calibration of temperature instruments using the comparative method.*

0 INTRODUCTION

The definition of a temperature scale, independent of the substance thermometric qualities used, was proposed by Kelvin in 1898 and was named the thermodynamic temperature scale, which coincides with a thermometer scale filled with a perfect gas. However, achieving this scale is practically impossible; therefore, another temperature scale was developed, the nearest possible to the thermodynamic one and fully characterized to remain convenient and maintain its precision.

Taking into account all these specifications, the international temperature scale (ITS) was created; it is updated every 20 years. This scale is based on a primary set of fixed points of temperature, for instance: the triple point of water, the melting point of gallium, the freezing point of zinc among many others. One of the calibration methods is based on the use of cells containing the fixed points cited in the ITS.

The other method of calibration is the comparison method, in which both the thermometer to be calibrated and the reference thermometer (calibrated one) are placed in an isothermal bath. The American Society for Testing and Materials (ASTM) established the calibration procedure to be followed when using this method [1]. For this purpose, a highly stable isothermal reservoir is required in order to avoid the so-called bar effect; this thermal phenomenon produces heat gains or losses due to the axial thermal gradient that appears when one end of the bar is in contact with the thermal source and transfers heat as a fin [2]. This situation leads to significant errors in temperature measurements, according to European Association of National Metrology Institutes EURAMET [3] and [4]. Reiss was a pioneer: he suggested using heat pipes to compensate the error induced by the bar effect in the calibration of thermometers [5].

Sostmann [6] and Bienert [7] proposed the use of heat pipes in thermometry; they pointed out that heat pipes are normally designed to transport the maximum heat flow with the minimum possible temperature difference. However, in thermometry applications, the heat transport capacity is less relevant than the device's isothermal behavior.

Tamba et al. evaluated a water heat pipe, controlling the operation pressure, when it was used as a comparative furnace in order to calibrate a standard platinum resistance thermometer (SPRT) in a range of 338.15 K to 430.15 K, in a direct comparison against the reference SPRT, the combined uncertainty was estimated as 3.1 mK. These results show that

*Corr. Author's Address: National Polytechnic Institute, School of Mechanical and Electrical Engineering Campus Zacatenco, Mexico, fsnchz@yahoo.com.mx

his system had a good performance for calibration purposes [8].

Noorma et al. used a water heat pipe as a black body, i.e. as a reference spectral radiator in order to be used as heat source between 323.15 K and 523.15 K; this was adopted by the National Institute of Standards and Technology NIST [9].

In contrast, isothermal furnaces have also been developed on heat pipe bases, but they require 30 minutes to achieve a stable operation temperature; Tasneem has proposed a cylindrical cavity in which the temperature is stabilized. The calibration is done using the cavity as a black body; the cylindrical cavity is filled with graphite in order to make the temperature uniform [10].

In this article, the experimental results of an annular TPT thermal characterization are presented; the goal is to determine its isothermal behavior and the time it takes to achieve this state of operation. The latter is the TPT's most significant characteristic for thermometry applications.

1 THEORY OF THERMOSYPHONS

1.1 Working Principles of Thermosyphons

Closed TPT, also known as wickless heat pipe, is a simple but effective two-phase heat transfer device. It performs better in a vertical position, with the evaporator or zone where the heat is supplied at the bottom; in this position, it takes advantage of the gravity acceleration for bringing down the condensed vapor as a liquid film [11].

The working fluid is stored at the TPT bottom as a liquid pool. The container is an evacuated closed pipe filled with a certain amount of a suitable working fluid. The TPT is divided into three main sections; the evaporator section, the adiabatic section, and the condenser section. If heat is added to the evaporator section, the working fluid inside the pipe vaporizes and carries heat from the heat source to the condenser section, where heat is removed by a cooling system. The condensed working fluid returns to the evaporator section, taking advantage of the gravity force, and closing the cycle. Therefore, the condenser section of the TPT must be located above the evaporator section.

1.2 Fundamentals for Calculation

In order to fully characterize the TPT, an experimental and analytical study must be undertaken. The condensation can be modeled as taking place inside a vertical pipe but with the interface liquid-vapor strain stress taken into consideration. The convection coefficient in the condenser is normally compared to the one given by the Nusselt theory or against the extended Nusselt theory [11].

In 1916, Nusselt was the first to consider the condensation phenomenon in a vertical plate without stress in the interface. Faghri et al. extended the Nusselt theory to a laminar and turbulent flow inside a thermosyphon, flow reduction due to the condensation rate was evaluated [12]. Spendel [17] also studied the condensation problem in the TPT; the momentum equation in the steam region was numerically solved for the laminar case and film condensing analysis in the condensing region was to coupled it.

In contrast, in the specialized literature there are two general approaches that are extensions of Nusselt's film condensation theory and are used to include the variable strain stress in the TPT condenser interface. The first method empirically stablishes the friction factor between the two phases in order to satisfy the mass balance to take into account the axial steam flow. The second numerically solves the steam flow in 2D and couples it with the Nusselt analysis for the film condensation.

When TPT is at steady state, the total pressure drop in a closed cycle is the addition of the both phases pressure drop in the different TPT regions. The total balance must be equal to zero [13].

$$P_g + \left(P_{VC} - P_{VE}\right) + \left(P_{LC} - P_{VC}\right) + \\ + \left(P_{LE} - P_{LC}\right) + \left(P_{VE} - P_{LE}\right) = 0. \quad (1)$$

In the above equation, $\left(P_{VC} - P_{VE}\right) = \Delta P_V$ is the pressure drop in the vapour phase flow, between the condenser and the evaporator.

$\left(P_{LE} - P_{LC}\right) = \Delta P_L$ is the pressure drop in the liquid phase flow between the evaporator and the condenser.

$\left(P_V - P_L\right)_E - \left(P_V - P_L\right)_C = 0$ represents the pressure difference in the interfaces liquid-vapour in the evaporator region and condenser region respectivelly, so that we can write:

$$P_g + \Delta P_V + \Delta P_L = 0. \quad (2)$$

This means that the total pressure drop in the three TPT regions must be equal to zero. Thereofre, the necessary condition for the TPT to function is:

$$P_g \geq \Delta P_V + \Delta P_L. \quad (3)$$

This means that gravity is the system driving force, which must always be equal or superior to the total pressure drop in the system. The pressure drop in

the liquid phase flow of the TPT working fluid can be determined using Darcy's equation:

$$\Delta P_L = -\frac{\mu_L}{\rho_L}\frac{\dot{m}_L}{K}\frac{l_{eff}}{A_L}. \quad (4)$$

Because TPT has not a wick on its inner wall, permeability K is a parameter depending on the system characteristics and the working fluid. Moreover, in the TPT, there is a countercurrent annular liquid-vapor flow, so the wavy interface is an important factor for the permeability magnitude. In contrast, l_{eff} is the TPT effective length and is given by:

$$l_{eff} = \frac{l_E}{2} + l_a + \frac{l_C}{2}. \quad (5)$$

In order to determine the pressure drop in the vapour phase, the following equation can be applied:

$$\Delta P_V = -\frac{8\mu_V}{\rho_V}\frac{\dot{m}_V}{\pi}\frac{l_{eff}}{r_V^4}. \quad (6)$$

Gravity effects are given by:

$$P_g = \pm\rho_L\, g\, l\, sin\theta, \quad (7)$$

where θ is the TPT inclination angle with respect to the horizontal. In our case, the TPT position is vertical with the evaporator at the bottom so, $\theta = 90°$ and the TPT gets the maximum driving force:

$$P_g = \pm\rho_L\, g\, l. \quad (8)$$

In contrast, it is well known that the transported heat flow by a TPT depends on the quantity of liquid working fluid that changes phase in the evaporator:

$$\dot{Q} = \dot{m}L, \quad (9)$$

in which L is the phase change enthalpy given by the expression:

$$L = h_V(T_S) - h_L(T_S). \quad (10)$$

In order to maintain the TPT steady state operation, the liquid mass flow that evaporates in the evaporator must be equal to the vapour mass flow that condenses in the condenser, that is $\dot{m}_L = \dot{m}_V$. Next, the liquid mass flow is obtained by adding Eqs. (4), (6) and (8):

$$\dot{m} = \frac{\rho_L^2 g\, l\, KA_L \pi\rho_V r_V^4}{l_{eff}\left(\mu_L \pi\rho_V r_V^4 + 8\mu_V \rho_L KA_L\right)}, \quad (11)$$

and the heat flow transported by a TPT is easily computed:

$$\dot{Q} = \frac{\left(h_V - h_L\right)\rho_L^2 g\, l\, KA_L \pi\rho_V r_V^4}{l_{eff}\left(\mu_L \pi\rho_V r_V^4 + 8\mu_V \rho_L KA_L\right)}. \quad (12)$$

2 EXPERIMENTAL SECTION

2.1 TPT Design

According to Faghri [11] and Sánchez et al. [14], the starting point in the TPT design for this kind of application is to know the temperature range in which the device is expected to work. With this information, the working fluid and the TPT body material are selected; both must be chemically compatible; moreover, in thermometry applications, the needed device dimensions are generally known, so it is desirable to use commercial pipes to build the annular TPT.

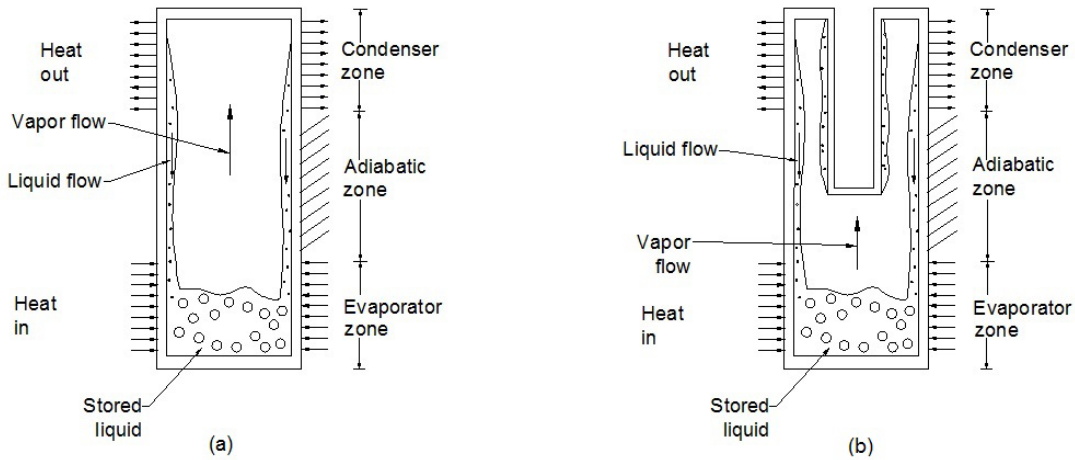

Fig. 1. *a) A conventional TPT; b) A two-phase closed annular thermosyphon*

Based on this information, the heat flux supplied to the evaporator zone can be determined as well as the magnitude of cooling water flow to obtain the stable temperature operation in the system.

Fig. 1 shows both a conventional TPT and the annular TPT for thermometry applications. Both the conventional and the annular TPT are pipes sealed on both sides and, using a pump, a vacuum was created before the introduction of the working fluid; the difference is that the annular TPT has an annular cross section in the condenser zone, and the annulus is used as a volume where the thermocouples will be installed for calibration. The annular TPT technical specifications are summarized in Table 1.

Table 1. *Annular TPT technical specifications*

Total length	500 mm
Evaporator zone length	200 mm
Adiabatic zone length	150 mm
Condenser zone length	150 mm
External diameter of the TPT internal pipe	28.6 mm
Internal diameter of the TPT internal pipe	26.2 mm
External diameter of the TPT external pipe	54 mm
Internal diameter of the TPT external pipe	50.8 mm
External diameter of the condenser sleeve	79.4 mm
Internal diameter of the condenser sleeve	74 mm
Thermal insulation material	Mineral wool
TPT body material	Copper
Working fluid	Water
Volume of the working fluid in the TPT	130 cm^3

For the 323.15 K to 523.15 K temperature range, the working fluid must be water. Copper type L was selected as the TPT body material; it withstands a pressure of 35 bar, even though the water saturation pressure at 373.15 K, which is the expected operation temperature, is 101.325 Pa. Both water and copper are chemically compatible so they can work together. The filling volume of working fluid was taken as 15 % of the TPT free volume according to Faghri [11], Sanchez [15] and Carvajal et al. [16]. The annular TPT dimensions are shown in Table 1.

2.2 Experimental System

For the experimental system, a 373 W centrifugal pump was selected to guarantee the cooling water circulation in the condenser. The experimental rig has two reservoirs to store cooling water for condensation with a volume of 1 m^3 each; both reservoirs are interconnected with a pipe located at the bottom of the tanks. For the heat supply system, a band electrical resistance was used; the resistance has an electrical power of 1,550 W and a resistance of 10.4 Ω. Fig. 2 shows a technical scheme of the experimental set up with all the elements. In Fig. 3 the annular TPT, the band type electrical resistance's installation, and the cooling system at the TPT top part are shown (all elements are without thermal insulation).

In order to change the power supply, a 120 VCA potentiometer was used. The potentiometer provides

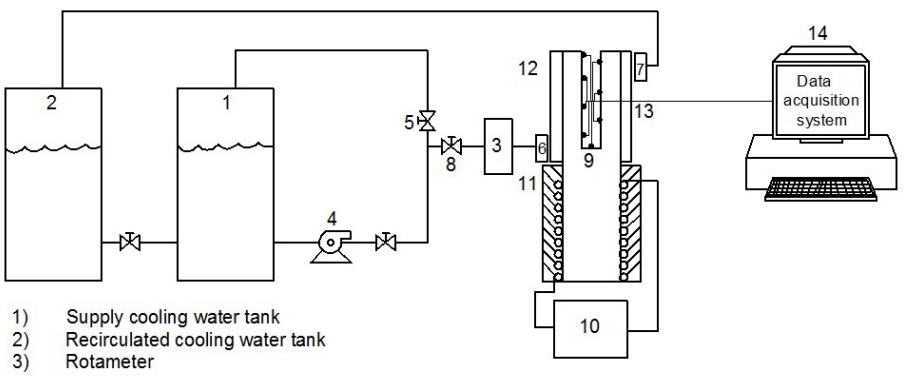

Fig. 2. *Technical scheme of the experimental set up*

0 V to 120 V, and it had connected a voltmeter (±0.05 V accuracy) in order to measure the voltage difference at the exit. A 0 cm³/s to 16.67 cm³/s range rotameter (±0.5 cm³/s accuracy) was used to measure the cooling water flow. The thermocouples used were of the K type (±2.2 ºC accuracy in the temperature range studied). They were used to measure the temperature on the surface of the internal pipe wall that is the annular zone, and they were also used to monitor the temperature of the cooling water at the inlet and outlet of the condenser.

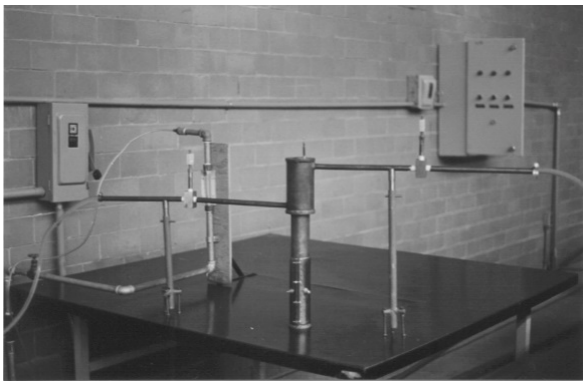

Fig. 3. *The annular TPT experimental system showing the band electrical resistance on the evaporator*

A digital thermometer (±0.5 ºC accuracy in the temperature range studied) with an Omega model HH-22 microprocessor was used for thermocouples type J/K. The thermocouples used in the experiments were located on the internal wall surface of the annular region, all the long its length and with a 3 cm separation between them, as shown in Fig. 4. The annular TPT was thermally insulated with mineral wool and was also covered with a sheet of aluminum.

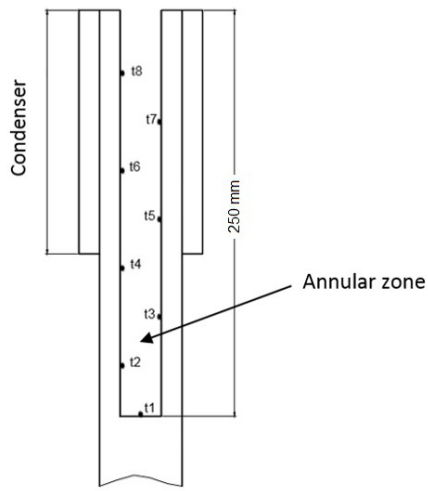

Fig. 4. *Location of the thermocouples in the TPT annular region*

3 EXPERIMENTAL RESULTS AND DISCUSSIONS

Experimental runs were undertaken in order to determine the time in which the annular TPT reaches a working steady state under different operating conditions. Therefore, thermocouples t1, t5 and t8 (see Fig. 4) were monitored during 30 minutes, i.e. the period in which the heating and cooling conditions were maintained at constant levels. Experiments were run for two different cooling water flows (16.67 cm³/s and 4.17 cm³/s), and for each of them the power supplied was varied (38, 154, 350, 1,385) W using the potentiometer to change the applied voltage according to Eq. (13)

$$\Phi = \frac{V^2}{R}. \tag{13}$$

3.1 Experimental Results

The experimental results with cooling water flows equal to 16.67 cm³/s and 4.17 cm³/s are shown in Fig. 5a and b. In these figures, it is possible to observe the temperature variation of the thermocouples t1, t5 and t8, located at the bottom, center and at the top of the annular region, respectively (Fig. 4), for three heat flow levels supplied to the evaporator: 154 W, 615 W and 1,385 W.

For 16.67 cm³/s, the cooling water flow temperature is slightly bigger for the thermocouple t1, but the difference against t5 and t8 is not more than 5K for the same power level supplied (Fig. 5a). In contrast, for the cooling water flow of 4.17 cm³/s (Fig. 5b), the temperature difference between t1, t5 and t8 is uneven; this means that the small cooling water flow is not enough to make the TPT temperature uniform. Practically, the TPT operation temperature for the small cooling water flow is always higher, and its behavior is uneven, especially in the case of 615 W, in which t1, t5 and t8 show values of (370, 351, 370) K, respectively.

In contrast, in Fig. 6a and b, the percentage of the variation in temperatures t1, t5 and t8 in respect with lectures obtained with the same thermocouples, 30 minutes after the beginning of the experiment, is plotted against time. Therefore, the time needed for steady state operation was obtained using the relation:

$$\%\Delta T_{30-i} = \frac{\left(T_{30} - T_i\right)}{T_{30}} 100 \ \%. \tag{14}$$

Fig. 6a and b show the TPT temperature behavior for the cooling water flows of 16.67 cm³/s, and 4.17 cm³/s, respectively. For larger cooling water flows,

there is a smooth tendency to the steady state, which is attained in (18, 28, 18) min for all the power supplied magnitudes, for t1, t5 and t8, respectively (Fig. 6a). In the case of the small cooling water flows, the behavior is more uneven; t1, t5 and t8 attain the steady state in (20, 24, 18) min, respectively (Fig. 6b).

For the cooling flow of 4.17 cm³/s, there is a difference of 5 % in the thermocouple t1 for 615 W that vanishes after 28 min of operation; in contrast, the thermocouple t8 shows that the steady state takes place after 18 min. As expected, the steady state is reached faster with larger cooling water flows.

To investigate in detail the isothermal behavior, the range of power supply values was broadened including 615 W and 960 W. In Fig. 7, t1 to t8 indicate the thermocouples installed inside the annular region (see Fig. 4). The wall's isothermal behavior inside the annular region is evident, and this condition is easily attained for power supplied in magnitudes greater than 350 W in the evaporator. In this work, isothermicity is defined as such state when the temperature difference is not bigger than 3 % along the TPT surface. It is important to note that the operation temperature values are always higher for the lower cooling water flow. For the power supplied in magnitudes of 38 W and 154 W, the uniformity of the temperature profile is never achieved; therefore, there is an axial temperature gradient, and the annular TPT efficiency is reduced.

Practically, for the two cooling water flows used in the experiments (16.67 cm³/s and 4.17 cm³/s) the steady state was obtained 18 min after the experiment

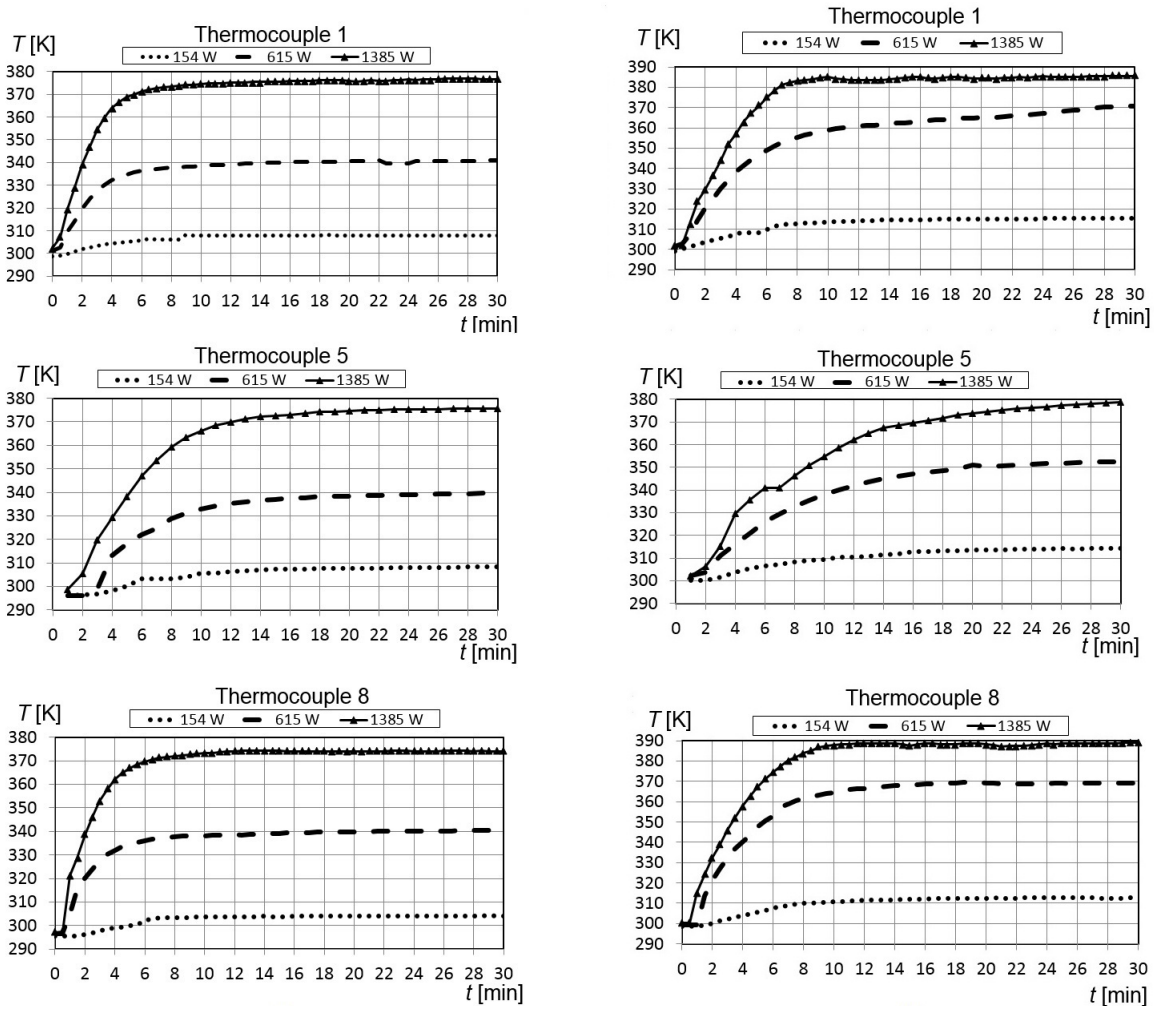

Fig. 5. *Temperature behavior measured by thermocouples t1, t5 and t8, for three heating conditions in the evaporator (154, 615, 1,385 W) versus time; a) for a cooling water flow of 16.67 cm³/s and b) for a cooling water flow of 4.17 cm³/s*

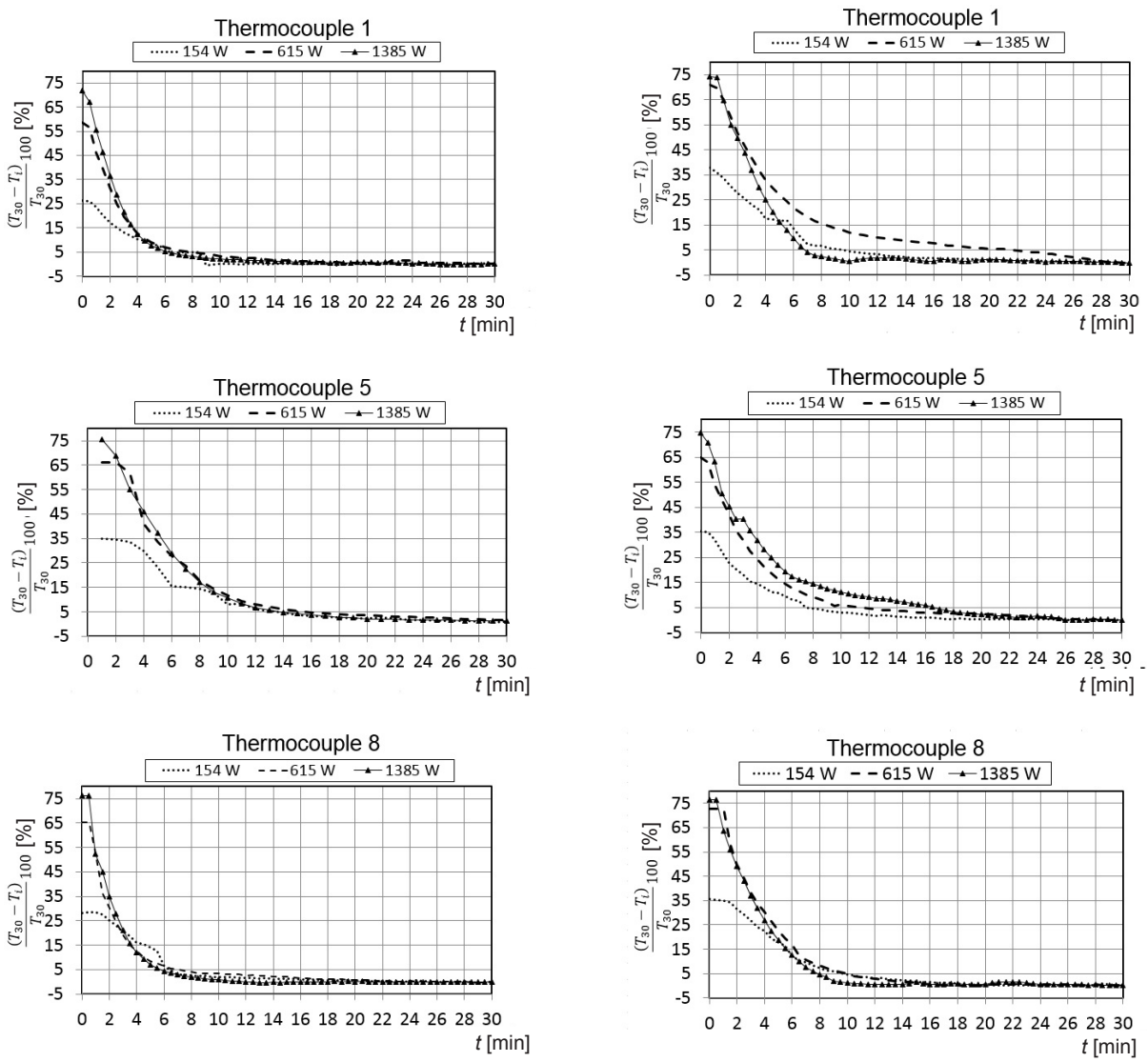

Fig. 6. *Percent variation of temperatures t1, t5 and t8 for three heat flow levels; a) for a cooling water flow of 16.67 cm³/s and b) for 4.17 cm³/s*

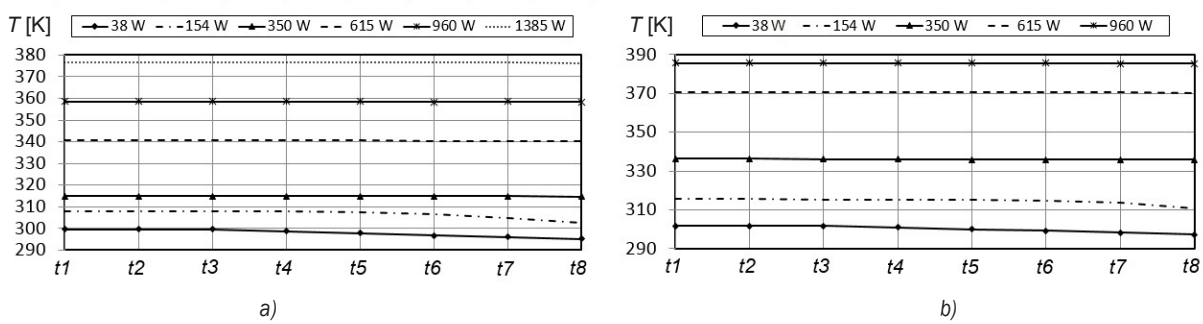

Fig. 7. *Temperature values measured for the different thermocouples t1 to t8 for 38, 154, 350, 615, 960 and 1385 W of heat flow levels supplied, with cooling water flow of a) 16.67 cm³/s and b) 4.17 cm³/s, 30 minutes after the experiment start*

started (heat flow supply and cooling water flow maintained constant). For this period, there was a variation in temperature values of 2 % in all analyzed cases.

3.2 Results Discussion

One of the objectives of this research was to evaluate the annular TPT as an isothermal source to calibrate temperature instruments, using the comparison method. In the experimental test, it was proved that TPT operation is isothermal along the 21 cm characterized annular zone length; consequently, the bar effect that produces a temperature measurement error, due to the axial temperature gradient, was avoided. Therefore, the device fulfills the requirements to be used as an isothermal reservoir for calibration purposes using the comparative method in the range from 313.15 K to 373.15 K. Of course, when the required range of application is larger, the TPT working fluid should be changed, as well the cooling fluid and its flow.

In this research, the annular TPT immersion depth was 21 cm, which can be easily extended by changing the device characteristics.

For the small heat flow magnitudes (38 W and 154 W), the heat flow supplied to evaporator is not sufficient to guarantee that the axial pressure gradient is near zero and consequently the axial isothermal behavior is not reached. Nevertheless, for heat flow supplied magnitudes higher than 350 W this effect disappears, as shown in Fig. 7. However, it is important to note that the annular TPT region operates at higher temperatures when the water cooling flow is reduced.

The other goal of this research is to propose the use of the TPT as a secondary reference for temperature instrument calibration. However, this application implies a guarantee of the TPT stability and repeatability for different TPT working conditions; therefore, there should be the same values of temperature in different schedules using the same operation conditions.

Figs. 8a and b show the temperature profile on the annular region wall of the TPT, for three distinct experimental tests carried out in different days, but keeping the same operation condition (960 W and 1,385 W, with 16.67 cm³/s of cooling water flow), after 30 minutes of the experiment start. In the above-mentioned graphs, it obvious that the temperature values are not strictly the same, and the differences were approximately of 4 K (i.e. 2.9 %): therefore, strictly speaking, the results are not reproducible.

This difference could be attributable to the cooling water temperature, which was not constant, because it depends on environmental conditions. In contrast, the other involved parameters (e.g. the electrical power supply and the cooling water flow) need to be controlled with a higher degree of precision.

In contrast, considering that the measured values obtained in different instants are not the same, it was not possible to obtain a calibration curve for the annular TPT in order to use it as a secondary reference for the calibration of temperature instruments.

In order to obtain a reliable TPT calibration curve and propose its use as a secondary reference for metrology purposes, it is necessary to keep constant, precise and stable the following parameters:

- Inlet cooling water temperature;
- Cooling water flow;
- Heat flow supplied magnitude in the evaporator.

Furthermore, even though the TPT is thermally insulated, it is also important to avoid any stream of air in the room where the experiments take place to avoid changing the surrounding conditions.

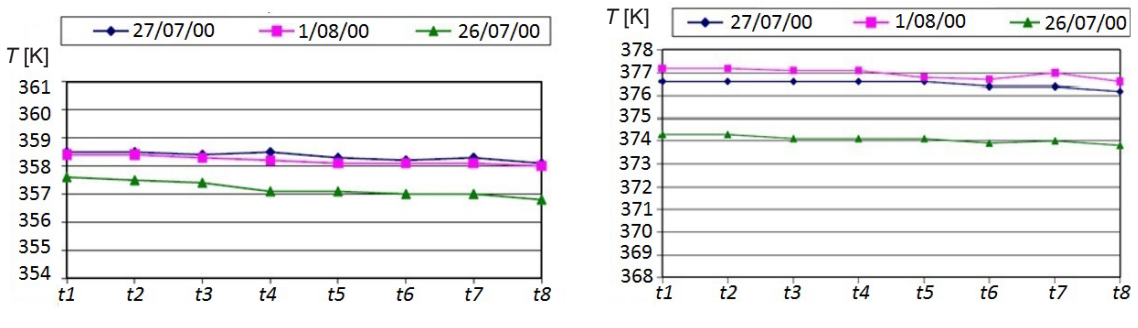

Fig. 8. *Repeatability of the axial temperature profile. Replay of the same experimental condition; a) 960 W and b) 1,385 W with 16.67 cm³/s of cooling water flow, carried out in different days and on a different schedule*

In order to evaluate the radial heat leakages, the thermal TPT efficiency was computed; this parameter was expected to be high because a TPT is similar to an ideal fin. The abovementioned is shown in Fig. 9, where the TPT efficiency is plotted at different operation power magnitudes, and was always higher than 94 %.

$$\eta = \frac{\dot{Q}_c}{\Phi}. \tag{15}$$

Therefore, the device fulfills the requirements of an isothermal reservoir for calibration purposes using the comparison method. The range of the device's stable operation can be broadened by making some changes as previously mentioned.

In contrast, if the variations of the temperature are reduced by controlling the main parameters affecting the TPT stable operation and their precision, it would be possible to use the annular TPT as a secondary reference for calibration purposes.

The mean uncertainty of measured temperature in the range studied was ± 6 %.

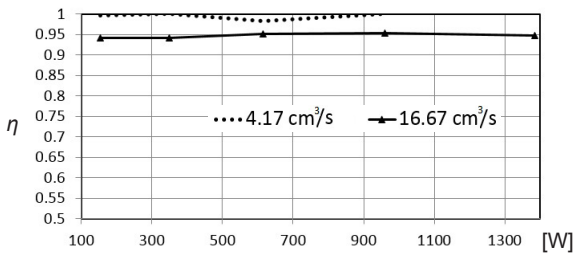

Fig. 9. *TPT Efficiency for different operation conditions*

Table 2. *Uncertainty of voltage V and power supplied Φ*

Voltage [V]	u_V [V]	u_Φ [%]
40	±0.00124	±0.514
60	±0.000814	±0.508
80	±0.000598	±0.496
100	±0.000482	±0.490
120	±0.000410	±0.488

Table 3. *Uncertainty of heat flow transported, $\dot{Q}$ and efficiency η*

Voltage [V]	u_Q [%]	u_η [%]
40	±4.20	±4.23
60	±2.88	±2.92
80	±2.61	±2.66
100	±2.55	±2.60
120	±2.53	±2.58

The maximum uncertainties obtained for main variables calculated in the present study is uncertainty of electrical resistance, *R*:

$$u_R = \pm 0.00481\ \Omega.$$

4 CONCLUSION

An annular two-phase thermosyphon was designed, built and characterized, in order to evaluate its use in thermometry. Experiments were carried out for 16.67 cm³/s and 4.17 cm³/s cooling water flows with heat flow supplied magnitudes in the evaporator of (38, 154, 350, 615, 960, 1,385) W for each cooling water flow.

Except in the cases of 38 W and 154 W, the isothermal TPT characteristic was observed throughout the annular 21 cm length.

The system accomplishes all the requirements for an isothermal source for calibration of temperature instruments using the comparative method. The bar effect does not appear or is reduced. Therefore, temperature measurements do not need to be corrected to take in account this thermal effect.

According to isothermal behavior shown by TPT, it can be proposed as an isothermal source for the calibration of temperature instruments using the comparative method.

Another advantage is the immersion depth of the temperature sensor, which is 21 cm, in this case. This value could be increased by changing the geometry of the annular TPT.

Regarding the repeatability of experiments, the cooling water temperature was not constant, because it depends on the surrounding conditions and other parameters involved, which were not fully controlled in the experiments (voltage, electric supply to the resistance terminals and cooling water flow). It was, thus, not possible to obtain the device calibration curve. Therefore, for experiments with the same operation conditions (heat flow supplied to evaporator and cooling water flow in the condenser), but in different schedules and days, there was not a good reproduction of the annular region temperature where the steady state was attained. Under these conditions, it is not possible to use the annular TPT as a secondary reference for calibration purposes.

5 ACKNOWLEDGMENT

The authors would like to thank the National Polytechnic Institute of Mexico and the National Science and Technology Agency of Mexico (CONACYT) for funding this research.

6 NOMENCLATURE

A	area	[m^2]
K	permeability	[m^2]
L	change phase specific enthalpy	[J/kg]
P	pressure	[Pa]
$\dot{Q}$	heat flow transported	[W]
R	electrical resistance	[Ω]
T	temperature	[K]
V	electrical potential	[V]
g	gravity acceleration	[m/s^2]
h	specific enthalpy	[J/kg]
l	length	[m]
$\dot{m}$	mass flow rate	[kg/s]
r	radius	[m]
t	time	[s]
u	uncertainty	[-]

Greek

Δ	difference	[-]
Φ	heat power supplied	[W]
η	efficiency	[-]
μ	dynamic viscosity	[Pa×s]
ρ	density	[kg/m^3]
q	inclination angle	[°]

Sub-index

a	adiabatic
eff	effective
g	gravity
i	instant
s	saturation
C	condenser
E	evaporator
L	liquid
LC	liquid in the condenser
LE	liquid in the evaporator
Q	heat flow transported
R	resistance
S	saturation
V	vapor, voltage
VC	vapor in the condenser
VE	vapor in the evaporator
30	after 30 minutes of exposition
30-i	difference between 30 minutes and the time i
η	efficiency

7 REFERENCES

[1] ASTM E 220-13, (2011). Standard method for calibration of thermocouples by comparison techniques. *American Society for Testing and Materials*, Philadelphia, **DOI:10.1520/E0220**.

[2] Mills, A.F. (1999). *Heat Transfer, 2nd ed.*, Prentice Hall, Homewood, Boston.

[3] EURAMET (2011). Calibration of Thermocouples, EURAMET cg-8, Version 2.1., *from: http://www.euramet.org/fileadmin/docs/Publications/calguides/EURAMET_cg-8__v_2.1_Calibration_of_Thermocouples.pdf*, accessed on 2015-03-10.

[4] Bernier, M.A., Baliga, B.R. (1993). Effects of heat losses (or gains) from insulated portions of closed loop thermosyphons with vertical heat transfer sections. *Journal of Heat Transfer*, vol. 115, no. 2, p. 480-482, **DOI:10.1115/1.2910705.**

[5] Reiss, F.E. (1974). Heat pipe as a means of avoiding emergent stem correction for liquid in glass Thermometers. *Review of Scientific Instruments*, vol. 45, no. 9, p. 1157-1158, **DOI:10.1063/1.1686831.**

[6] Sostmann, H.E. (1991). The heat pipe and its use in thermometer calibration. *ISOTECH Journal of Thermometry*, vol. 2, no. 1, p. 31.

[7] Bienert, W.W. (1991). Isothermal heat pipes and pressure controlled furnaces. *ISOTECH Journal of Thermometry*, vol. 2, no. 1, p. 32-49.

[8] Tamba, J., Kishimoto, I., Arai, M., (2002). Evaluation of a Pressure-Controlled Water Heat Pipe for Accurate Comparison of Platinum Resistance Thermometers. *Proceedings of the 41st Society of Instrument and Control Engineers*, Osaka, vol. 4, p. 2435-2438, **DOI:10.1109/SICE.2002.1195792**.

[9] Noorma, M., Mekhontsev, S., Khromchenko, V., Litorja, M., Cagran, C., Zeng, J., Hanssen, L. (2006). Water heat pipe blackbody as a reference spectral radiance source between 50°C and 250°C. *Proceedings of the International Conference on Thermal Sensing and Imaging Diagnostic Applications*, vol. 6205, **DOI:10.1117/12.667257.**

[10] Tasneem, K.A. (2009). Calibrating a thermocouple and investigating heat transfer. Technical Report: Heat transfer and thermocouples. Lahore University of Management Sciences, Lahore, *from http://lums.edu.pk/docs/Calibration.pdf*, accessed on 2015-03-10.

[11] Faghri, A., (1995). *Heat Pipe Science and Technology*. Taylor & Francis Group, London.

[12] Faghri, A., Chen, M.M., Morgan, M. (1989). Heat transfer characteristics in two-phase closed conventional and concentric annular thermosyphons. *Journal of Heat Transfer*, vol. 111, no. 3, p. 611-618, **DOI:10.1115/1.3250726**.

[13] Chi, S.W. (1976). *Heat Pipe Theory and Practice*, McGraw-Hill, New York.

[14] Sánchez-Silva, F., Carvajal Mariscal, I., Tolentino Eslava, G., Abugaber Francis, J. (2001). Thermal and mechanical design of a two phase flow thermosyphon heat exchanger. *Información Tecnológica*, vol. 12, no. 3, p. 63-70. (in Spanish)

[15] Sánchez-Silva, F. (1980). *Contribution to the study of two-phase water thermosyphons*, Ph.D. Thesis, Université de Poitiers, Poitiers. (in French)

[16] Carvajal-Mariscal, I., Sánchez-Silva, F., Polupan G., (2012). Development of High Efficiency Two-Phase Thermosyphons for Heat Recovery. Mitrovic, J. (ed.). *Heat Exchangers - Basics Design Applications*, p. 97-116, **DOI:10.5772/32693**.

[17] Spendel, T. (1984). Laminar film condensation heat transfer in closed two-phase thermosyphons. *Proceedings of 5th International Heat Pipe Conference*, p. 208-213.

Vsebina

Strojniški vestnik - Journal of Mechanical Engineering
letnik 61, (2015), številka 4
Ljubljana, april 2015
ISSN 0039-2480

Izhaja mesečno

Razširjeni povzetki

Osebne vesti

Strojniški vestnik - Journal of Mechanical Engineering 61(2015)4, SI 43

Prejeto v recenzijo: 2014-11-12
Prejeto popravljeno: 2015-02-03
Odobreno za objavo: 2015-02-03

Identifikacija materialnih lastnosti pločevine v prečni smeri glede na ravnino valjanja s procesom prebijanja

Špela Bolka[1] – Janko Slavič[2] – Miha Boltežar[2,*]
[1] Hidria Rotomatika, Slovenia
[2] Univerza v Ljubljani, Fakulteta za strojništvo, Slovenija

Karakterizacija materialnih lastnosti pločevine se tipično izvaja v ravnini valjanja pločevine s pomočjo standardiziranih testov, denimo enoosnega nateznega ali strižnega preizkusa. Pločevino za različne aplikacije, na primer prebijanje ali globoki vlek, se praviloma dobavlja v večjih kolutih. Materialne lastnosti se spreminjajo že v posameznem kolutu, zagotovo pa med posameznimi koluti, kar otežuje tako proizvodnjo kvalitetnih izdelkov, kot tudi eksperimentalno karakterizacijo materiala. Poleg tega se preoblikovanje pločevine pretežno izvaja v prečni smeri glede na ravnino valjanja pločevine, zato bi bilo smotrno spreminjanje materialnih lastnosti spremljati v tej smeri, vrednosti identificiranih parametrov pa primerjati z vrednostmi, dobljenimi na podlagi standardnih enoosnih nateznih testov v ravnini valjanja pločevine.

V prispevku obravnavamo pristop k eksperimentalni karakterizaciji mehanskih lastnosti pločevine v prečni smeri glede na ravnino valjanja pločevine. Za eksperimentalno identifikacijo je uporabljena na novo razvita laboratorijska naprava za prebijanje pločevine, ki omogoča polne, delne (do določene globine) ter zaporedne (zaporedni delni preboji do polnega pretrga materiala) preboje pločevine pri različnih hitrostih procesa. Naprava omogoča veliko ponovljivost in natančnost meritev. Mogoča je uporaba različnih geometrij rezilnih elementov – v obravnavanem delu so bili uporabljeni rezilni elementi krožne oblike nazivnega premera 10 mm ter zračnosti 0.025 mm na polmer. Polni preboji so bili izvedeni kvazistatično s hitrostjo približno 0.1 mm/s ter dinamično s hitrostmi (200, 250, 300, 350) mm/s. Enako so bili kvazistatično in dinamično izvedeni tudi delni preboji do globin (100, 200, 300, 350) μm ter zaporedni preboji s korakom 50 μm oziroma 100 μm. Pri tem so bili delni in zaporedni kvazistatični preboji izvedeni z enako hitrostjo kot polni, pri dinamičnih eksperimentih pa je bila začetna hitrost prebijanja ravno dovolj velika, da je nož prebil material do želene globine. Za vse eksperimente je bila uporabljena končno-žarjena elektro pločevina debeline 0.5 mm, eksperimenti pa so bili izvedeni brez dodatnega mazanja in pri sobnih temperaturah.

Eksperimenti polnih prebojev so služili kot osnova za identifikacijo strižne meje tečenja in strižne trdnosti materiala, ki jih je bilo nato mogoče primerjati z natezno mejo tečenja in natezno trdnostjo materiala v smeri valjanja pločevine. Z uporabo delnih in zaporednih prebojev pa je bilo mogoče iz testa prebijanja identificirati akumulacijo poškodovanosti materiala. Tudi te rezultate je bilo moč primerjati z rezultati nateznih testov – s pomočjo koračnih enoosnih nateznih testov je mogoče, z opazovanjem spreminjanja naklona krivulje razbremenjevanja, določiti napredovanje parametra poškodovanosti, popisanega z Lemaitreovim izotropnim zakonom poškodovanosti. Enak pristop je bil uveden tudi v prečni smeri glede na ravnino valjanja pločevine.

Predstavljena metoda tako omogoča nov način karakterizacije in neposrednega spremljanja materialnih lastnosti iz samega procesa prebijanja, kar nakazuje možnost širše industrijske uporabe za sprotno identifikacijo materialnih lastnosti.

Ključne besede: rezanje in preoblikovanje, konstitutivne relacije, elasto-plastični material, mehanski testi, žilavi lom, eksperiment v smeri, prečni na ravnino valjanja

*Naslov avtorja za dopisovanje: Univerza v Ljubljani, Fakulteta za strojništvo, Aškerčeva 6, 1000 Ljubljana, Slovenija, miha.boltezar@fs.uni-lj.si

Strojniški vestnik - Journal of Mechanical Engineering 61(2015)4, SI 44

Prejeto v recenzijo: 2014-10-18
Prejeto popravljeno: 2015-01-23
Odobreno za objavo: 2015-02-09

Mehanske lastnosti dveh okolju prijaznih smol, ojačenih z lanenimi vlakni

Dario Croccolo* – Massimiliano De Agostinis – Stefano Fini – Alfredo Liverani – Nicolò Marinelli – Eugenio Nisini – Giorgio Olmi
Univerza v Bologni, Oddelek za industrijski inženiring (DIN), Italija

Članek podaja primerjavo mehanskih lastnosti dveh različnih kompozitnih materialov z naravnimi vlakni. Kompozita sta izdelana iz dveh različnih okolju prijaznih smol in ojačena z enakimi lanenimi vlakni. Prva (181 EN2X) je smola na bazi izoftalne kisline s 25 % polietilen tereftalata, pridobljenega iz recikliranega materiala. Druga (VEef220ST) je vinil ester, pridobljen iz bisfenolne epoksi smole z majhno vsebnostjo stirena. Ti dve smoli sta se uveljavili v pomorstvu zaradi visoke obstojnosti proti vplivom okolja, še posebej proti korozivnemu učinku slane vode.

Mehanske lastnosti kompozitov so bile preiskane z nateznimi, strižnimi in upogibnimi preizkusi po veljavnih standardih (ISO 527-1 in -4, ISO 14125, ISO 14130). Eksperimenti so bili opravljeni na stiskalnici Instron 8033, opremljeni s 25 kN obremenitveno celico, nastavljivimi prijemali za natezni preizkus in provizorično podporo za tritočkovno obremenitev pri upogibnih in strižnih preizkusih, skladno z ISO 14125 in ISO 14130. Preizkušenih je bilo skupno 32 vzorcev, pripravljenih po omenjenih standardih. Pri nateznih in upogibnih preizkusih so bili pridobljeni sprejemljivi rezultati, kar pa ne velja za strižne preizkuse, kjer so vzorci odpovedali na nesprejemljiv način – verjetno zaradi lastnosti laminiranega kompozita.

Rezultati kažejo, da je izoftalna smola boljša od vinil estrske smole (VEef220ST) tako po trdnosti, kakor tudi po togosti. Ojačitev poveča natezno trdnost smole 181 EN2X za približno 25,4 %, modul elastičnosti za približno 21,5 %, upogibno trdnost za približno 8,7 % in upogibni modul elastičnosti za približno 8,2 %. Pri vinil estrski smoli je ugoden učinek ojačitve nekoliko manj izražen, predvsem pri natezni trdnosti. V diskusiji je predstavljena primerjava s podobnimi študijami v dostopni literaturi, ki obravnavajo kompozite, ojačene z rastlinskimi vlakni. Omeniti je treba, da je učinek ojačitve z lanenimi vlakni pri okolju prijaznih smolah primerljiv z učinkom ojačitve pri kompozitih, izdelanih s konvencionalnimi epoksi smolami. Za oceno adhezije med ojačitvijo in matriksom ter prisotnosti napak je bilo nekaj vzorcev iz izoftalne smole razrezanih in pregledanih pod optičnim mikroskopom. Analiza je pokazala, da je osnovna nit premera 500 μm do 600 μm, medtem ko je votkovna nit premera 200 μm do 250 μm. Zračnih vključkov je manj in so manjši v primerjavi s podatki iz literature za kompozite, iz katerih se izdelujejo trupi plovil. Analiza površine zloma pri vzorcih nateznega preizkusa je pokazala homogeno in pravilno površino, kar pomeni, da matriks in ojačitev skupaj prispevata k celotni natezni trdnosti kompozita.

Takšen rezultat je dokaz za dobro adhezijo med komponentama. Najpomembnejši sklep te študije je, da se mehanske lastnosti izoftalne smole občutno izboljšajo s prisotnostjo vlaknene ojačitve. Pomembna lastnost te smole je, da je zelo občutljiva na prisotnost lanenih vlaken. Nasprotno pa dodajanje teh vlaken ni nujno koristno tudi pri matriksu iz vinil estrske smole.

Ključne besede: kompoziti z naravnimi vlakni, mehanske lastnosti, lan, okolju prijazna smola, napetosti, deformacije

*Naslov avtorja za dopisovanje: Univerza v Bologni, Oddelek za industrijski inženiring (DIN), Viale del Risorgimento 2, 40136 Bologna, Italija, dario.croccolo@unibo.it

Strojniški vestnik - Journal of Mechanical Engineering 61(2015)4, SI 45

Prejeto v recenzijo: 2014-11-21
Prejeto popravljeno: 2015-01-15
Odobreno za objavo: 2015-02-06

Postopek snovanja dvofaznega tihega verižnega prenosnika Hy-Vo

Yabing Cheng* – Yang Wang – Lei Li – Shuaibing Yin – Lichi An – Xiaopeng Wang
Univerza Jilin, Fakulteta za tehniške vede in strojništvo, Kitajska

Dvofazni tihi verižni prenosni sistem Hy-Vo je zasnovan za zmanjšanje fluktuacij in poligonskega efekta pri pogonskih sistemih. Članek podaja postopek snovanja dvofaznega tihega prenosnega sistema s ploščicami, verižnikom in orodjem kot teoretično osnovo za projektiranje drugih večfaznih verižnih prenosnikov.

Predstavljen je postopek snovanja dvofaznega tihega verižnega prenosnika Hy-Vo. Dvofazni verižnik ima za razliko od enofaznih prenosnikov dva razdelka in dve skupini kotov pritiska. Zaradi fazne razlike med zobmi dvofaznega verižnika imajo lahko zobje obeh faz različne razdelke in kote pritiska. Postavljen je model dvofaznega tihega verižnega prenosnika Hy-Vo in dvofazni prenosnik je razstavljen v dva enofazna prenosna sistema. Poligonski efekt dvofaznega prenosnega sistema, ki ga opisuje veličina fluktuacije, je analiziran matematično in s simulacijo.

Članek preučuje metodo snovanja dvofaznega tihega verižnega prenosnika Hy-Vo ter poligonski efekt pri dvofaznem prenosniku. Na podlagi teorije ubiranja tihe verige Hy-Vo z verižnikom in povezanega pogoja ubiranja tihega verižnika Hy-Vo z orodjem sta zasnovana multivariabilna tiha veriga in verižnik Hy-Vo ter je postavljen sistem ubiranja dvofazne tihe verige Hy-Vo. Razlika med fluktuacijami pri dvofaznih in enofaznih prenosnih sistemih je bila analizirana s Fourierjevo vrsto, za oceno poligonskega efekta pa je bila uporabljena simulacija.

Sistem za snovanje ubiranja med tiho verigo, verižnikom in orodjem Hy-Vo je primeren tako za snovanje enofaznih tihih verižnih prenosnih sistemov Hy-Vo, kakor tudi za snovanje dvofaznih tihih prenosnih sistemov Hy-Vo. Metoda snovanja ploščic tihe verige, verižnika in orodja dvofaznega sistema Hy-Vo je v tem primeru novost. Če sta razdelka dvofaznega verižnika enaka in sta enaki tudi skupini kotov pritiska, je lahko trenutno prenosno razmerje dvofaznega prenosnega sistema drugačno od trenutnega prenosnega razmerja razstavljenega neodvisnega enofaznega prenosnega sistema. Največja fluktuacija pri dvofaznem prenosnem sistemu je manjša kot pri enofaznem sistemu, manjši pa je tudi poligonski efekt.

Članek preučuje metodo snovanja dvofaznega tihega verižnega prenosnika Hy-Vo ter poligonski efekt pri dvofaznem prenosniku. V prihodnjih raziskavah bi bilo mogoče preučiti tudi hrup in napetosti dvofaznega tihega verižnega prenosnika Hy-Vo, kakor tudi sistem večfazne verige.

Predstavljen je nov postopek snovanja dvofaznega tihega verižnega prenosnika Hy-Vo. Uporaba tihe verige in dvofaznega verižnika Hy-Vo v prenosnih sistemih, npr. za krmiljenje odmične gredi, oljne črpalke in izravnalne gredi, lahko zmanjša hrup ter pripomore k bolj gladkemu delovanju prenosnega sistema.

Ključne besede: dvofazni prenosnik, tiha veriga Hy-Vo, multivariabilnost, snovanje sistema ubiranja, veličina fluktuacij, poligonski efekt

*Naslov avtorja za dopisovanje: Univerza Jilin, Fakulteta za tehniške vede in strojništvo, Renmin street 5988, Changchun, Kitajska, chengyb@jlu.edu.cn

Strojniški vestnik - Journal of Mechanical Engineering 61(2015)4, SI 46

Prejeto v recenzijo: 2014-12-02
Prejeto popravljeno: 2015-01-21
Odobreno za objavo: 2015-02-05

Simulator sistema vodenja hrapavosti površine pri procesu struženja

Franci Čuš – Uroš Župerl*
Univerza v Mariboru, Fakulteta za strojništvo, Slovenija

Cilj članka je predstaviti modelno podprt sistem vodenja struženja s pripadajočim simulacijskim blokovnim diagramom. Namen na modelu temelječega sistema vodenja je zagotavljati želeno hrapavost obdelane površine s sprotnim prilagajanjem rezalnih parametrov in ohranjanjem konstante rezalne sile. Sistem z dinamično adaptacijo podajanja obvladuje hrapavost površine ter rezalne sile na struženem nožu. Namen izdelave predlaganega sistema vodenja je poiskati omejitve takšnega principa vodenja. Modelno podprt sistem vodenja je izdelan na osnovi poenostavljenega modela procesa struženja in podajalnega servo-sistema. Celotni sistem vodenja se sesoji iz modela napovedovanja rezalnih pogojev, referenčnega bloka, bloka vodenja, procesa odrezavanja, CNC servo-sistema, elementa za korekcijo podajanja in senzorja, ki meri izhodno veličino procesa.

Glavna predpostavka raziskave je bila, da signali izmerjenih rezalnih sil vsebujejo največ uporabnih informacij o kakovosti obdelane površine. Zato so izvedeni eksperimenti, s katerimi so določene funkcijske korelacije med hrapavostjo obdelane površine, rezalnimi silami in parametri vodenja. Korelacija med procesnima izhodnima veličinama in rezalnimi parametri je določena z regresijo. Pri vnaprej definirani globini rezanja je eksperimentalno raziskan vpliv obdelovalnega materiala in rezalnih parametrov (podajanje, globina rezanja) na omenjeno korelacijo. Ugotovljena je visoka stopnja ujemanja med hrapavostjo površine in rezultirajočo rezalno silo pri različnih rezalnih pogojih. Te povezave se nato uporabljene pri izdelavi modelno podprtega sistema vodenja v katerem se z reguliranjem rezalnih sil izboljšuje zahtevana kakovost obdelane površine.

Z namenom demonstracije učinkovitosti predlaganega sistema vodenja je predstavljena zgradba simulatorja in simulacijski rezultati. Model vodenja je izdelan v simulacijskem paketu Matlab-Simulink. Izpeljana je prenosna funkcija celotnega procesa struženja. Rezultati simulacij pokažejo, da je z vidika fluktuacij hrapavosti površine in učinkovitosti struženja predlagan sistem vodenja precej bolj učinkovit kot sistem z konvencionalnim CNC krmiljem. S simulacijami je potrjena adekvatnost in stabilnost sistema vodenja. Rezultati zagotovijo načine za povečanje učinkovitosti procesa z izboljšanjem kakovosti površine, minimiziranjem posledic spremenljivosti procesa in zmanjšanjem stroškov napak pri operacijah končne obdelave. Dokazano je, da lahko z obvladovanjem rezalnih sil uspešno nadzorujemo hrapavost površine, ki je bistven kazalec kakovosti procesa. Z ohranjanjem konstantne rezalne sile se zagotovi konstantna kakovost obdelane površine.

Po uspešno izvedenih simulacijah je bil simulacijski model CNC servo-sistema in simulator odrezavanja nadomeščen z obdelovalnim strojem GF NDM 16. Stružnica je vodena s CNC krmiljem, katero omogoča korekcije podajalne hitrosti v območju od 0 % do 150 %. Povezana je s osebnim računalnikom na katerem je implementiran sitem vodenja.

Zmogljivosti predlaganega sistema so testirane s serijo eksperimentov na Ck45 jeklenih testnih preizkušancih pri spremenljivih rezalnih pogojih. Z integracijo izdelanega sistema vodenja s CNC krmiljem stružnice se poveča kakovost obdelanih komponent. Obdelovalni sistem postane neobčutljiv na motnje zaradi obrabe orodja, nehomogenosti obdelovalnega materiala ter variacij globine struženja. Sistem je zasnovan za preoces struženja, vendar ga je možno prilagoditi za vse postopke obdelave z odrezavanjem.

Ključne besede: odrezavanje, hrapavost površine, modelno podprto vodenje, simulator

*Naslov avtorja za dopisovanje: Univerza v Mariboru, Fakulteta za strojništvo, Smetanova ulica 17, 2000 Maribor, Slovenija, uros.zuperl@um.si

Strojniški vestnik - Journal of Mechanical Engineering 61(2015)4, SI 47

Prejeto v recenzijo: 2014-09-19
Prejeto popravljeno: 2015-03-03
Odobreno za objavo: 2015-03-11

Algoritem na osnovi metode robnih elementov za URANS simulacije toka preko kvadratne ovire

Janez Lupše* – Leopold Škerget – Jure Ravnik
Univerza v Mariboru, Fakulteta za strojništvo, Slovenija

Danes so numerične metode za preračun toka tekočin v industriji v vsakodnevni uporabi. Vendar pa je večina industrijsko pomembnih tokovnih problemov računsko zahtevnih, kar je povezano z velikimi računskimi zmogljivostmi in s tem veliko porabo časa in energije. Večina današnjih metod v uporabi deluje na principu »surove sile«, kjer z zelo gostimi numeričnimi mrežami opisujemo fizikalno dinamiko pojavov. Glavna prednost metode robnih elementov (MRE), v primerjavi z večino ostalih numeričnih metod, je vključitev fizikalnih mehanizmov toka že med samim postopkom diskretizacije, kar vodi v zmanjšanje potreb po gosti numerični mreži, hkrati pa poveča stabilnost numeričnega algoritma.

V članku predstavljamo numerični algoritem, osnovan na metodi robnih elementov, za računanje nestacionarnih tokov v direktnem in URANS načinu. Algoritem je osnovan na hitrostno-vrtinčnem zapisu Navier-Stokesovih enačb. Tak zapis uporabljajo tudi drugi najbolj učinkoviti algoritmi za izvajanje direktnih numeričnih simulacij. Pomemben del algoritma je določitev robnih vrednosti vrtinčnosti, kjer se uporaba MRE izkaže. Izračun območnih vrednosti mora biti opravljen globalno na celotni domeni reševanja, kar pripelje do reševanja polnih sistemov enačb in s tem velike uporabe računalniškega spomina ter posledično praktičnih omejitev pri velikosti numeričnih mrež. Delno se da problem omiliti z raznoraznimi metodami stiskanja polne matrike, saj se izkaže, da imajo členi, ki ležijo daleč stran od diagonale, zanemarljiv vpliv na natančnost rešitve, ali pa z uporabo drugačne oblike vodilnih enačb. Zaradi lastnosti Greenovih funkcij, uporabljenih kot utežne funkcije v obravnavani metodi, je možno uporabiti relativno redke numerične mreže v primerjavi z drugimi metodami. Hkrati so del rešitve tudi normalni odvodi funkcij polja, kar zmanjša napake pri računanju le-teh in je pomembno npr. pri natančni določitvi Nusseltovega števila.

Algoritem je nadgradnja našega algoritma, razvitega za RANS modele z integracijo do zida. Ker so ti modeli nezadostni v primeru, ko je tokovni problem že v sami osnovi nestacionaren, smo v predloženem članku algoritem razširili še za URANS simulacije. Preverjanje algoritma je izvedeno na primeru toka okoli kvadratne ovire v ravnem kanalu, pri čemer je bilo razmerje med širino ovire in širino kanala 1:8. Tok postane nestacionaren že pri Reynoldsovem številu med 54 in 70, kar omogoča preverjanje algoritma že v laminarnem režimu. V laminarnem režimu smo izvedli numerične simulacije pri Reynoldsovih številih 100, 150, 200 in 250 ter v nizko turbulentnem režimu pri Reynoldsovem številu 1000. Simulacije laminarnega toka pokažejo dobro ujemanje rezultatov z rezultati izračunov iz literature za komponento hitrosti v smeri toka in tudi za Strouhalovo število ter koeficient upora. V nizko turbulentnem režimu obravnavamo tok s pomočjo kvazi-direktne numerične simulacije in s Spalart-Allmarasovim modelom turbulence v URANS načinu, kjer primerjamo rezultate za oba integralna parametra z rezultati iz literature. Zaradi dušenja toka z modelirano viskoznostjo v URANS simulaciji ne vidimo manjših struktur v toku, kar se pozna tudi pri obeh izračunanih parametrih, tok pa postane navidezno podoben laminarnemu. V nasprotju pa pri kvazidirektni simulaciji tega dušenja nimamo in so simulirane strukture omejene z velikostjo mreže, kar se kaže v veliko bolj bogatem spektru struktur v toku.

Ključne besede: metoda robnih elementov, numerični algoritem, hitrostno-vrtinčna oblika, turbulentni tok nestisljive tekočine, URANS, kvadratna ovira

*Naslov avtorja za dopisovanje: Univerza v Mariboru, Fakulteta za strojništvo, Smetanova ulica 17, 2000 Maribor, Slovenija, janez.lupse@yahoo.ca

Strojniški vestnik - Journal of Mechanical Engineering 61(2015)4, SI 48

Prejeto v recenzijo: 2014-11-10
Prejeto popravljeno: 2015-02-27
Odobreno za objavo: 2015-03-05

Raziskava glavnega/podrejenega krmiljenja položaja/tlaka za servohidravlični sistem potujočih škarij

Wang Jun[1] – Sun Binyu[1,*] – Huang Qingxue[1] – Li Hongzhou[2] – Han Heyong[1]

[1] Tniverza za znanost in tehnologijo v Taiyuanu, Kitajska
[2] Hebei WenFeng železo in jeklo, Kitajska

Na univerzi za znanost in tehnologijo v Taiyuanu so bile razvite potujoče hidravlične škarje, ki se uporabljajo za rezanje jeklenih plošč debeline do 35 mm. Če debelina jeklenih plošč presega 35 mm, imajo potujoče škarje težave z rezanjem in podatki kažejo, da ni mogoče dovolj hitro vzpostaviti tlaka. Razlog je v tem, da škarje uporabljajo le zaprtozančno krmiljenje položaja in tlak ni pod nadzorom.

Za razrešitev problema predlagamo novo funkcijo za glavno/podrejeno krmiljenje položaja/tlaka, ki lahko izboljša točnost položaja in tlaka. Zahteve krmiljenja položaja in tlaka so si navidezno v nasprotju, zato uspešno krmiljenje obeh parametrov predstavlja poseben izziv. Nova krmilna funkcija je zasnovana kot dvojen zaprtozančni sistem, kjer ima glavno vlogo krmiljenje položaja in sekundarno vlogo krmiljenje tlaka. Tlačni signal iz valja zaznajo tlačni senzorji in ga pošljejo v model za pretvorbo tlaka in položaja. Krmilnik nato presodi, ali se tlačni signal doda položajnemu signalu. Če je napaka položajnega signala večja od praga, se priključi zaprta zanka za krmiljenje tlaka in tlačni signal se pretvori v kompenzacijski signal za prilagoditev vhodnega položajnega signala. Pretok servoventila se hitro poveča in valj postane hiter, tako da je napaka položaja valja majhna, tlak in položaj valja pa sta pod nadzorom. Krmiljenje položaja ne vpliva na krmiljenje tlaka. Z novim pristopom je mogoče istočasno krmiliti položaj in tlak valja. Glavno/podrejeno krmiljenje položaja/tlaka, ki je opisano v članku, izboljšuje varnost pred zatikanjem, natančnost in stabilnost sistema. Debelina rezanih jeklenih plošč je lahko večja za 35 %, izboljša pa se tudi kakovost. Krmilni sistem je mogoče enostavno vgraditi v omenjene in druge hidravlične servosisteme z visokimi hitrostmi, velikimi pretoki in velikimi bremeni.

Članek podaja matematični model glavnega/podrejenega krmiljenja položaja/tlaka za servohidravlični sistem. Sistem je bil simuliran s programsko opremo AMEsim in Matlab, pri čemer je bila potrjena uporabnost pristopa. Končno so bili opravljeni tudi poizkusi na eksperimentalni opremi z novo funkcijo. Rezultati eksperimentov kažejo, da lahko glavno/podrejeno krmiljenje položaja/tlaka izboljša natančnost in stabilnost servohidravličnega sistema, novo funkcijo pa je mogoče uporabiti tudi za drugo visokohitrostno, visokonatančno in težko opremo.

Omejitev nove funkcije je v funkciji pretvorbe. Zdaj se uporablja sprotni nadzor položaja in tlaka valja ter izračunavanje količnika pretvorbe, ki je počasno in zahteva visokokakovosten nadzorni sistem. Učinkovitost bi se bistveno izboljšala, če bi bilo pretvorbo mogoče zapisati z izrazom.

Članek predstavlja nov pristop k združevanju položaja in tlaka, za katera sicer velja, da ju ni mogoče krmiliti istočasno. Za izboljšanje natančnosti in stabilnosti je uvedena funkcija za pretvorbo tlačnega signala, ki se lahko doda položajnemu signalu. Nov krmilni sistem razširja priložnosti za odkrivanje novih načinov krmiljenja servohidravličnih sistemov. Uporaben je v vseh tehničnih sistemih, ki istočasno zahtevajo visoko natančnost položaja in tlaka, zlasti pri opremi z visoko hitrostjo, velikimi pretoki in velikimi bremeni.

Ključne besede: potujoče škarje, hidravlični sistem, krmilni sistem, glavno/podrejeno krmiljenje položaja/tlaka, pretvorba, natančnost, stabilnost

*Naslov avtorja za dopisovanje: Taiyuan University of Science and Technology, No. 66 Waliu Street, Taiyuan, Kitajska, sunby_sby@126.com

Strojniški vestnik - Journal of Mechanical Engineering 61(2015)4, SI 49

Prejeto v recenzijo: 2014-08-15
Prejeto popravljeno: 2015-01-14
Odobreno za objavo: 2015-02-26

Študija obročastega dvofaznega termosifona kot izotermnega vira pri merjenju temperature

Florencio Sánchez-Silva* – Ignacio Carvajal-Mariscal – Ariel E. Moreno-Cordobés – Pedro Quinto Diez – Miguel Toledo Velázquez

Nacionalni politehnični institut, Šola za strojništvo in elektrotehniko, Mehika

Opravljena je bila študija uporabnosti obročastega dvofaznega termosifona (TPT) pri merjenju temperature in glavni rezultati toplotne zmogljivosti so predstavljeni v tem članku. Obročasti TPT je zasnovan kot izotermen vir za umerjanje merilnikov temperature po metodi primerjave. V ta namen je bil zasnovan, zgrajen in eksperimentalno okarakteriziran obročast TPT z vodo kot delovnim fluidom. Za eksperimentalno opredelitev delovanja obročaste površine TPT je bilo aksialno po notranji obročasti površini v območju kondenzatorja nameščenih osem termoparov. Toplotno moč je zagotavljal električni upornik v območju uparjalnika in toploto je zbiral pretočni sistem hladilne vode okrog kondenzatorja. Toplota je bila merjena po načelih kalorimetrije.

Preizkusi so bili opravljeni pri dveh različnih pretokih hladilne vode: 16,67 cm^3/s in 4,17 cm^3/s. Pri vsakem pretoku hladilne vode so bile vzpostavljene štiri različne ravni toplotne moči v območju uparjanja: (38, 154, 350, 1385) W. Rezultati eksperimentov so pokazali, da je delovanje toplotne naprave izotermno pri ravneh moči nad 350 W, kjer se aksialni temperaturni gradient zmanjša na zelo nizko raven in torej ni več vedenja kot pri palici, ki je na enem koncu v stiku s toplotnim virom in oddaja toploto kot rebro. Manjša je tudi napaka meritev temperature. Izotermni pogoji se po zaslugi visoke prevodnosti naprave TPT vzpostavijo že v par minutah in tako je mogoče v kratkem času opraviti več umerjanj. Pri manjših toplotnih močeh (38 W in 154 W) toplotni tok v uparjalnik ni dovolj velik, da bi se aksialni gradient približal vrednosti nič in zato ni doseženo aksialno izotermno vedenje. Ta težava izgine pri toplotnih močeh nad 350 W. Poudariti je treba, da deluje obročasti del TPT pri višjih temperaturah, ko se zmanjša pretok hladilne vode.

Drugi cilj raziskave je bil preučitev možnosti uporabe TPT kot sekundarnega vira za umerjanje merilnikov temperature. Za takšno uporabo je nujna stabilnost in ponovljivost TPT pri različnih delovnih pogojih. Vrednosti temperature morajo biti torej enake pri različnih režimih ob enakih delovnih pogojih. Temperaturni profil stene obročastega dela TPT je bil pridobljen v treh ločenih eksperimentalnih preizkusih, opravljenih na različne dni in v enakih delovnih pogojih. Pridobljene vrednosti temperature niso strogo enake – razlika je bila približno 4 K ali 2,9 % in rezultati torej niso ponovljivi.

Potopno globino temperaturnih tipal, ki je bila 21 cm, je mogoče povečati s spremembo parametrov geometrije obročastega termosifona. Uporabno temperaturno območje bi bilo mogoče razširiti na poljubno območje s pomočjo primernega delovnega fluida in primerne zmogljivosti ogrevalnega/hladilnega sistema.

Na tem področju preostaja še obravnava stabilnosti in ponovljivosti z nadzorom nad vsemi glavnimi parametri eksperimenta. Z vzpostavitvijo takšne ravni nadzora bi bilo obročasti TPT mogoče uporabiti kot sekundarno referenco pri umerjanju temperaturnih instrumentov.

Ključne besede: merjenje temperature, dvofazni termosifoni, izotermni, obročasti, umerjanje, eksperiment

*Naslov avtorja za dopisovanje: Nacionalni politehnični institut, Šola za strojništvo in elektrotehniko, Campus Zacatenco, Mehika, fsnchz@yahoo.com.mx

Doktorske disertacije, magistrska dela, diplomske naloge

DOKTORSKE DISERTACIJE

Na Fakulteti za strojništvo Univerze v Ljubljani sta obranila svojo doktorsko disertacijo:

- dne *6. marca 2015* **Vanja ČOK** z naslovom: »Implementacija Kansei inženiringa v razvojno-konstrukcijski proces« (mentor: prof. dr. Jožef Duhovnik, somentorica: izr. prof. dr. Metoda Dodič Fikfak);

Obstoječa metodologija kansei inženiringa tipa 1 upošteva čustvene odzive določene skupine kupcev. Cilj doktorske disertacije je dopolnitev metodologije kansei inženiringa tipa 1, tako da bo metodologijo mogoče uporabiti za analizo dveh ali več skupin kupcev. Razvoj izdelkov za globalni trg zahteva mehanizme, ki omogočajo preverbo odziva lokacijsko različnih kupcev na izdelek. Zanimalo nas je kako z uporabo dopolnjene metodologije kansei inženiringa tipa 1 odkrijemo razlike med dvema skupinama kupcev. S pilotno študijo smo analizirali obstoječi postopek kansei inženiringa tipa 1. V pilotni študiji smo ugotavljali tudi kje se kansei inženiring tipa 1 vključuje v razvojno-konstrukcijski proces. Razvili smo metodološki model KCUL, ki upošteva čustvene odzive več skupin kupcev do vizualnih elementov izdelka v zgodnji fazi koncipiranja, natančneje v nivojih abstrakcije. Model KCUL smo razvili, preverili in potrdili na skupini študentov iz Srednje Evrope in Južne Azije. V doktorskem delu je razvita metoda implementacije nadgrajenega kansei inženiringa tipa 1 v razvojno-konstrukcijski proces;

- dne *30. marca 2015* **Matej SITAR** z naslovom: »Določitev geometrijskega stanja konstrukcijskega elementa iz funkcionalnega gradiva po razbremenitvi in nelinearnim elasto-plastičnem utrjevanju« (mentor: prof. dr. Franc Kosel);

Obravnavan je problem določanja geometrijskih in mehanskih stanj enoosnih funkcionalno grajenih nosilcev med in po procesu upogibnega obremenjevanja in razbremenjevanja v elasto-plastičnem območju. Pri tem so nosilci nesimetričnega prečnega prereza izdelani iz gradiv z nelinearno utrjevalnim reološkim modelom. Upoštevana sta tako izotropni kot tudi kinematični model utrjevanja. Stanje specifičnih deformacij je definirano kot funkcija zasuka in premika nevtralne osi ter ukrivljenosti vzdolžne osi nosilca. Upoštevana je celotna zgodovina obremenjevanja, skupaj z efektom lokalnega obremenjevanja določenih vlaken nosilca pri monotono padajoči obremenitvi in obratno. Na osnovi numeričnih primerov je predstavljen vpliv velikosti maksimalne obremenitve na končen in (elastično) povračljiv zasuk nevtralne osi, njen premik ter končno in (elastično) povračljivo ukrivljenost osi nosilca ob različnih oblikah prečnega prereza in gradivih. Ustreznost predstavljenega teoretičnega modela je preverjena z eksperimenti. Ob upoštevanju evolucije elastičnega modula se izkaže, da relativna razlika med numerično in eksperimentalno določenimi rezultati znaša le 0,273 %.

*

Na Fakulteti za strojništvo Univerze v Mariboru je obranil svojo doktorsko disertacijo:

- dne *19. marca 2015* **Milan KAMBIČ** z naslovom: »Raziskava primernosti ionskih tekočin za uporabo v hidravličnih sistemih« (mentor: izr. prof. dr. Darko Lovrec);

Vsaka vrsta hidravlične tekočine ima svoje prednosti za določen primer uporabe. Voda, kot prva in tudi v zadnjih letih ponovno aktualna hidravlična tekočina je negorljiva, praktično nestisljiva, neškodljiva za zdravje človeka ter okolje, cenena in razpoložljiva skoraj povsod. Mineralno olje je možno uporabiti skoraj povsod in v raznovrstni opremi. Težko vnetljive hidravlične tekočine zaradi večje varnosti pred požarom uporabljamo predvsem v metalurških obratih in premogovnikih, biološko hitreje razgradljive hidravlične tekočine pa zaradi manjše nevarnosti za okolje predvsem v mobilni hidravliki. Poleg prednosti pa ima vsaka vrsta hidravlične tekočine tudi slabosti, tako da je pri izbiri najbolj primerne vedno potreben nek kompromis. Idealne rešitve ni, radi pa bi se ji vsaj približali.

Cilj doktorske disertacije je bil, da v praktično neomejenem številu različnih ionskih tekočin, skušamo poiskati nekaj primernih za uporabo v hidravličnih sistemih in na ta način predlagati bodočo alternativo današnjim, običajno uporabljanim hidravličnim tekočinam. V ta namen so obravnavane osnovne lastnosti ionskih tekočin in njihove prednosti. Primernost smo ugotavljali tako na osnovi meritev fizikalno kemijskih lastnosti, kot tudi na osnovi praktičnih testov, aktualnih za hidravlične tekočine. V disertaciji so uporabljene laboratorijske in praktične testne metode tudi podrobneje opisane.

Veliko pozornosti je posvečeno sposobnosti korozijske zaščite, saj večina testiranih vzorcev ni nudila zadostne zaščite pred korozijo. Prav tako je podrobneje obravnavana stisljivost, saj ima

neposreden vpliv na porabo energije in odzivnost hidravličnih sistemov.

Pri iskanju ionske tekočine, ki bi bila primerna za uporabo v hidravličnih sistemih se je izkazalo, da kljub nekaterim boljšim rezultatom v primerjavi s konvencionalnimi hidravličnimi tekočinami, (za sedaj) ni veliko takih, ki bi vse potrebne lastnosti imele vsaj na trenutnem nivoju konvencionalnih hidravličnih tekočin.

*

MAGISTRSKA DELA

Na Fakulteti za strojništvo Univerze v Ljubljani so pridobili naziv magister inženir strojništva:

dne 2. marca 2015:

Samo ČARMAN z naslovom: »Presoja meroslovnih značilnic merilnika padavin« (mentor: izr. prof. dr. Ivan Bajsić);

Simon GODEC z naslovom: »Analiza vpliva tehnoloških parametrov visokotlačnega struženja pri obdelavi zlitine Inconel 718« (mentor: doc. dr. Davorin Kramar, somentor: izr. prof. dr. Peter Krajnik);

Andrej KASTELIC z naslovom: »Razvoj vsebnika ultra tanke toplotne cevi« (mentor: prof. dr. Iztok Golobič, somentor: doc. dr. Matija Jezeršek);

dne 27. marca 2015:

Klemen KOTNIK z naslovom: »Modeliranje torzijskih vibracij motorja z notranjim izgorevanjem ter njihov prenos prek pogonskega sistema« (mentor: prof. dr. Miha Boltežar, somentor: prof. dr. Jörg Wallaschek);

Marko BRUS z naslovom: »Nadgradnja pravil načrtovanja izdelave oblikovnih plošč za brizganje komponente avtomobilskega žarometa« (mentor: izr. prof. dr. Joško Valentinčič, somentor: doc. dr. Andrej Lebar);

Nejc JEGLIČ z naslovom: »Tehnologija izdelave orodja za brizganje plastike in avtomatizacija proizvodnega procesa« (mentor: izr. prof. dr. Joško Valentinčič, somentor: izr. prof. dr. Niko Herakovič).

*

Na Fakulteti za strojništvo Univerze v Ljubljani je uspešno zagovarjal svoje magistrsko delo magistrskega študijskega programa II. stopnje:

dne 2. marca 2015:

Pablo GUTIERREZ RUIZ z naslovom: »Povezava med tlačnimi nihanji in kavitacijsko erozijo / Relationship between pressure oscialtions and cavitation erosion« (mentor: izr. prof. dr. Matevž Dular).

*

Na Fakulteti za strojništvo Univerze v Mariboru sta pridobila naziv magister gospodarski inženir:

dne 25. marca 2015:

Nejc CVÖRNJEK z naslovom: »Uporaba algoritmov po vzorih iz narave pri napovedovanju cene delnic in optimizaciji portfelja« (mentorja: prof. dr. Miran Brezočnik, prof. dr. Timotej Jagrič);

Sandi KAČIČNIK z naslovom: »Dolgoročno planiranje produktnih in storitvenih platform na področju pomivalnih strojev« (mentorja: izr. prof. dr. Iztok Palčič, doc. dr. Igor Vrečko).

DIPLOMSKE NALOGE

Na Fakulteti za strojništvo Univerze v Ljubljani so pridobili naziv univerzitetni diplomirani inženir strojništva:

dne 2. marca 2015:

Nejc DRAKSLER z naslovom: »Izdelava vodilnika aksialnega ventilatorja sadjarskega pršilnika« (mentor: izr. prof. dr. Marko Hočevar, somentor: prof. dr. Branko Širok);

Gal HLEBANJA z naslovom: »Izdelava in tribološke lastnosti polimernih kompozitov z dodatki grafita in polidimetilsiloksana« (mentor: prof. dr. Mitjan Kalin, somentor: doc. dr. Miroslav Huskić);

Alja PUHEK z naslovom: »Vpliv sekundarnega toka na tokovne razmere ob površini krila« (mentor: prof. dr. Branko Širok, somentor: doc. dr. Tom Bajcar);

dne 27. marca 2015:

Jani BOLE z naslovom: »Modifikacija navoja prednapetega visokotrdnostnega vijaka« (mentor: doc. dr. Boris Jerman, somentor: prof. dr. Marko Nagode);

Miha ZUPANC z naslovom: »Analiza mehanskih lastnosti lepljenega spoja med NdFeB magnetom in jeklenim rotorjem« (mentor: doc. dr. Viktor Šajn, somentor: prof. dr. Franc Kosel);

Jera AVŠIČ z naslovom: »Primerjava med točkovnim uporovnim in točkovnim laserskim varjenjem« (mentor: prof. dr. Janez Tušek);

Jernej OBLAK z naslovom: »Optimiranje nastavitev 3D skenerja za dosego najboljših rezultatov meritev« (mentor: doc. dr. Andrej Lebar, somentor: doc. dr. Davorin Kramar);

dne 30. marca 2015:

Klemen SPRUK z naslovom: »Uporaba mikro-parne turbine v sistemu SPTE z izkoriščanjem lesne biomase« (mentor: prof. dr. Mihael Sekavčnik).

*

Na Fakulteti za strojništvo Univerze v Ljubljani je uspešno zagovarjal svoje diplomsko delo univerzitetnega študija :

dne 26. marca 2015:

Albert PEREZ ESTEVE z naslovom: »Razvoj dogodkovno gnanega simulacijskega modela proizvodne delavnice / Application of a discrete event simulation in a manufacturing workshop« (mentor: prof. dr. Alojzij Sluga).

*

Na Fakulteti za strojništvo Univerze v Ljubljani sta pridobila naziv diplomirani inženir strojništva:

dne 5. marca 2015:

Alenka FILIPAŠIĆ z naslovom: »Izbor turbinskega agregata HE Završnica« (mentor: prof. dr. Branko Širok);

Uroš KERMC z naslovom: »Toplozračni solarni ogrevalni sistem z latentnim hranilnikom toplote« (mentor: prof. dr. Sašo Medved, somentor: doc. dr. Ciril Arkar).

*

Na Fakulteti za strojništvo Univerze v Mariboru je pridobil naziv diplomirani inženir strojništva (UN):

dne 25. marca 2015:

Nejc GRAJŽL z naslovom: »Izdelava hladilnih celic« (mentor: izr. prof. dr. Iztok Palčič).

*

Na Fakulteti za strojništvo Univerze v Mariboru je pridobil naziv diplomirani gospodarski inženir (UN):

dne 25. marca 2015:

Samo FIJAVŽ z naslovom: »Priprava projekta selitve podjetja iz najetih v lastne prostore na primeru podjetja MF-CT d.o.o.« (mentorja: izr. prof. dr. Iztok Palčič, doc. dr. Igor Vrečko).

*

Na Fakulteti za strojništvo Univerze v Mariboru sta pridobila naziv diplomirani inženir strojništva:

dne 26. marca 2015:

Mitja BLAGOTINŠEK z naslovom: »Primerjava plinskega ogrevanja, ogrevanja s spremenljivim volumnom hladila in njuna kombinacija« (mentor: izr. prof. dr. Jure Marn);

Tadej FIGEK z naslovom: »Tehnološke izboljšave pri izdelavi zavorne zagozde za avtomatski menjalnik« (mentor: prof. dr. Miran Brezočnik, somentor: prof. dr. Jože Balič).

*

Na Fakulteti za strojništvo Univerze v Ljubljani so pridobili naziv diplomirani inženir strojništva (VS):

dne 5. marca 2015:

Luka KOVAČIČ z naslovom: »Tehnično-ekonomska zasnova male fotonapetostne elektrarne« (mentor: prof. dr. Mihael Sekavčnik);

Rok PANDEL z naslovom: »Razvlaknjenje fruktoze na enokolesni centrifugi« (mentor: prof. dr. Branko Širok);

Anže SLIVNIK z naslovom: »Analiza aeroprofila krila s spremenljivo obliko« (mentor: izr. prof. dr. Tadej Kosel).

*

Na Fakulteti za strojništvo Univerze v Mariboru je pridobil naziv diplomirani inženir strojništva (VS):

dne 27. marca 2015:

Tomaž GRACEJ z naslovom: »Rekonstrukcija dodajalnika okroglih surovcev na 28MN stiskalnici za namene zmanjšanja mrtvega časa med cikli« (mentor: izr. prof. dr. Darko Lovrec, somentor: dr. Vito Tič).

Information for Authors

All manuscripts must be in English. Pages should be numbered sequentially. The manuscript should be composed in accordance with the Article Template given above. The maximum length of contributions is 10 pages. Longer contributions will only be accepted if authors provide juastification in a cover letter. For full instructions see the Information for Authors section on the journal's website: http://en.sv-jme.eu .

SUBMISSION:

Submission to SV-JME is made with the implicit understanding that neither the manuscript nor the essence of its content has been published previously either in whole or in part and that it is not being considered for publication elsewhere. All the listed authors should have agreed on the content and the corresponding (submitting) author is responsible for having ensured that this agreement has been reached. The acceptance of an article is based entirely on its scientific merit, as judged by peer review. Scientific articles comprising simulations only will not be accepted for publication; simulations must be accompanied by experimental results carried out to confirm or deny the accuracy of the simulation. Every manuscript submitted to the SV-JME undergoes a peer-review process.

The authors are kindly invited to submit the paper through our web site: http://ojs.sv-jme.eu. The Author is able to track the submission through the editorial process - as well as participate in the copyediting and proofreading of submissions accepted for publication - by logging in, and using the username and password provided.

SUBMISSION CONTENT:

The typical submission material consists of:

- A **manuscript** (A PDF file, with title, all authors with affiliations, abstract, keywords, highlights, inserted figures and tables and references),
- Supplementary files:
  - a **manuscript** in a WORD file format
  - a **cover letter** (please see instructions for composing the cover letter)
  - a ZIP file containing **figures** in high resolution in one of the graphical formats (please see instructions for preparing the figure files)
  - possible **appendicies** (optional), cover materials, video materials, etc.

Incomplete or improperly prepared submissions will be rejected with explanatory comments provided. In this case we will kindly ask the authors to carefully read the Information for Authors and to resubmit their manuscripts taking into consideration our comments.

COVER LETTER INSTRUCTIONS:

Please add a **cover letter** stating the following information about the submitted paper:

1. Paper **title**, list of **authors** and their **affiliations**.
2. **Type of paper**: original scientific paper (1.01), review scientific paper (1.02) or short scientific paper (1.03).
3. A **declaration** that neither the manuscript nor the essence of its content has been published in whole or in part previously and that it is not being considered for publication elsewhere.
4. State the **value of the paper** or its practical, theoretical and scientific implications. What is new in the paper with respect to the state-of-the-art in the published papers? Do not repeat the content of your abstract for this purpose.
5. We kindly ask you to suggest at least two **reviewers** for your paper and give us their names, their full affiliation and contact information, and their scientific research interest. The suggested reviewers should have at least two relevant references (with an impact factor) to the scientific field concerned; they should not be from the same country as the authors and should have no close connection with the authors.

FORMAT OF THE MANUSCRIPT:

The manuscript should be composed in accordance with the Article Template. The manuscript should be written in the following format:

- A **Title** that adequately describes the content of the manuscript.
- A list of **Authors** and their **affiliations**.
- An **Abstract** that should not exceed 250 words. The Abstract should state the principal objectives and the scope of the investigation, as well as the methodology employed. It should summarize the results and state the principal conclusions.
- 4 to 6 significant **key words** should follow the abstract to aid indexing.
- 4 to 6 **highlights;** a short collection of bullet points that convey the core findings and provide readers with a quick textual overview of the article. These four to six bullet points should describe the essence of the research (e.g. results or conclusions) and highlight what is distinctive about it.
- An **Introduction** that should provide a review of recent literature and sufficient background information to allow the results of the article to be understood and evaluated.
- A **Methods** section detailing the theoretical or experimental methods used.
- An **Experimental section** that should provide details of the experimental set-up and the methods used to obtain the results.
- A **Results** section that should clearly and concisely present the data, using figures and tables where appropriate.
- A **Discussion** section that should describe the relationships and generalizations shown by the results and discuss the significance of the results, making comparisons with previously published work. (It may be appropriate to combine the Results and Discussion sections into a single section to improve clarity.)
- A **Conclusions** section that should present one or more conclusions drawn from the results and subsequent discussion and should not duplicate the Abstract.
- **Acknowledgement** (optional) of collaboration or preparation assistance may be included. Please note the source of funding for the research.
- **Nomenclature** (optional). Papers with many symbols should have a nomenclature that defines all symbols with units, inserted above the references. If one is used, it must contain all the symbols used in the manuscript and the definitions should not be repeated in the text. In all cases, identify the symbols used if they are not widely recognized in the profession. Define acronyms in the text, not in the nomenclature.
- **References** must be cited consecutively in the text using square brackets [1] and collected together in a reference list at the end of the manuscript.
- **Appendix(-icies)** if any.

SPECIAL NOTES

Units: The SI system of units for nomenclature, symbols and abbreviations should be followed closely. Symbols for physical quantities in the text should be written in italics (e.g. *v*, *T*, *n*, etc.). Symbols for units that consist of letters should be in plain text (e.g. ms^{-1}, K, min, mm, etc.). Please also see: http://physics.nist.gov/cuu/pdf/sp811.pdf .

Abbreviations should be spelt out in full on first appearance followed by the abbreviation in parentheses, e.g. variable time geometry (VTG). The meaning of symbols and units belonging to symbols should be explained in each case or cited in a **nomenclature** section at the end of the manuscript before the References.

Figures (figures, graphs, illustrations digital images, photographs) must be cited in consecutive numerical order in the text and referred to in both the text and the captions as Fig. 1, Fig. 2, etc. Figures should be prepared without borders and on white grounding and should be sent separately in their original formats. If a figure is composed of several parts, please mark each part with a), b), c), etc. and provide an explanation for each part in Figure caption. The caption should be self-explanatory. Letters and numbers should be readable (Arial or Times New Roman, min 6 pt with equal sizes and fonts in all figures). Graphics (submitted as supplementary files) may be exported in resolution good enough for printing (min. 300 dpi) in any common format, e.g. TIFF, BMP or JPG, PDF and should be named Fig1.jpg, Fig2.tif, etc. However, graphs and line drawings should be prepared as vector images, e.g. CDR, AI. Multi-curve graphs should have individual curves marked with a symbol or otherwise provide distinguishing differences using, for example, different thicknesses or dashing.

Tables should carry separate titles and must be numbered in consecutive numerical order in the text and referred to in both the text and the captions as Table 1, Table 2, etc. In addition to the physical quantities, such as *t* (in italics), the units [s] (normal text) should be added in square brackets. Tables should not duplicate data found elsewhere in the manuscript. Tables should be prepared using a table editor and not inserted as a graphic.

REFERENCES:

A reference list must be included using the following information as a guide. Only cited text references are to be included. Each reference is to be referred to in the text by a number enclosed in a square bracket (i.e. [3] or [2] to [4] for more references; do not combine more than 3 references, explain each). No reference to the author is necessary.

References must be numbered and ordered according to where they are first mentioned in the paper, not alphabetically. All references must be complete and accurate. Please add DOI code when available. Examples follow.

Journal Papers:

Surname 1, Initials, Surname 2, Initials (year). Title. Journal, volume, number, pages, DOI code.

[1] Hackenschmidt, R., Alber-Laukant, B., Rieg, F. (2010). Simulating nonlinear materials under centrifugal forces by using intelligent cross-linked simulations. *Strojniški vestnik - Journal of Mechanical Engineering,* vol. 57, no. 7-8, p. 531-538, DOI:10.5545/sv-jme.2011.013.

Journal titles should not be abbreviated. Note that journal title is set in italics.

Books:

Surname 1, Initials, Surname 2, Initials (year). Title. Publisher, place of publication.

[2] Groover, M.P. (2007). *Fundamentals of Modern Manufacturing*. John Wiley & Sons, Hoboken.

Note that the title of the book is italicized.

Chapters in Books:

Surname 1, Initials, Surname 2, Initials (year). Chapter title. Editor(s) of book, book title. Publisher, place of publication, pages.

[3] Carbone, G., Ceccarelli, M. (2005). Legged robotic systems. Kordić, V., Lazinica, A., Merdan, M. (Eds.), Cutting Edge Robotics. Pro literatur Verlag, Mammendorf, p. 553-576.

Proceedings Papers:

Surname 1, Initials, Surname 2, Initials (year). Paper title. Proceedings title, pages.

[4] Štefanić, N., Martinčević-Mikić, S., Tošanović, N. (2009). Applied lean system in process industry. *MOTSP Conference Proceedings*, p. 422-427.

Standards:

Standard-Code (year). Title. Organisation. Place.

[5] ISO/DIS 16000-6.2:2002. *Indoor Air – Part 6: Determination of Volatile Organic Compounds in Indoor and Chamber Air by Active Sampling on TENAX TA Sorbent, Thermal Desorption and Gas Chromatography using MSD/FID.* International Organization for Standardization. Geneva.

WWW pages:

Surname, Initials or Company name. Title, from http://address, date of access.

[6] Rockwell Automation. Arena, from *http://www.arenasimulation.com,* accessed on 2009-09-07.

EXTENDED ABSTRACT:

When the paper is accepted for publishing, the authors will be requested to send an **extended abstract** (approx. one A4 page or 3500 to 4000 characters). The instruction for composing the extended abstract are published on-line: http://www.sv-jme.eu/information-for-authors/ .

COPYRIGHT:

Authors submitting a manuscript do so on the understanding that the work has not been published before, is not being considered for publication elsewhere and has been read and approved by all authors. The submission of the manuscript by the authors means that the authors automatically agree to transfer copyright to SV-JME when the manuscript is accepted for publication. All accepted manuscripts must be accompanied by a Copyright Transfer Agreement, which should be sent to the editor. The work should be original work by the authors and not be published elsewhere in any language without the written consent of the publisher. The proof will be sent to the author showing the final layout of the article. Proof correction must be minimal and executed quickly. Thus it is essential that manuscripts are accurate when submitted. Authors can track the status of their accepted articles on http://en.sv-jme.eu/.

PUBLICATION FEE:

Authors will be asked to pay a publication fee for each article prior to the article appearing in the journal. However, this fee only needs to be paid after the article has been accepted for publishing. The fee is 240.00 EUR (for articles with maximum of 6 pages), 300.00 EUR (for articles with maximum of 10 pages), plus 30.00 EUR for each additional page. The additional cost for a color page is 90.00 EUR. These fees do not include tax.

Strojniški vestnik -Journal of Mechanical Engineering
Aškerčeva 6, 1000 Ljubljana, Slovenia,
e-mail: info@sv-jme.eu

9 770039 248001
ISSN 0039-2480

http://www.sv-jme.eu

Contents

Papers